CHAPTER 4

Epitaxial Growth of Semiconductor Self-Assembled Quantum Dots

H. J. Kim, Z. M. Zhao, B. Shi, J. Lin, Y. H. Xie
Department of Materials Science and Engineering, University of California, Los Angeles, CA, USA

CONTENTS

1. Introduction 149
2. Quantum Dot Based Device Applications 151
3. Three Growth Modes 156
4. Ge Quantum Dot on Si 157
   4.1. Pyramid to Dome Transition 157
5. InAs Quantum Dots on GaAs 174
   5.1. Growth Parameters that Strongly Affect Dot Formation 174
   5.2. Optical Properties for Optoelectronic Applications 179
   5.3. Strain and Dislocations in Quantum Dots 183
   5.4. Summary 185
6. Other Group Quantum Dots 185
   6.1. Self-Organized GaN Quantum Dots on AlN 185
   6.2. Self-Assembled PbSe Quantum Dots on PbTe(111) Under Tensile Strain 187
7. InGaAs Quantum Dots on Si 188
   7.1. Introduction 188
   7.2. III–V Quantum Dots on IV Substrates 190
   7.3. Summary 197
8. Conclusion 197
   References 199

1. INTRODUCTION

Semiconductor quantum structures subject to three-dimensional (3D) confinement (also known as quantum dots) possess many properties that are beneficial for electronic and optoelectronic applications. Many of these device applications are not possible with lesser degrees of confinement, e.g., semiconductor structures in which electrons and holes have one, two,

ISBN: 1-58883-074-8
Copyright © 2006 by American Scientific Publishers
All rights of reproduction in any form reserved.

Handbook of Semiconductor Nanostructures and Nanodevices
Edited by A. A. Balandin and K. L. Wang
Volume 1: Pages (149–204)

and three degrees of freedom, also known as quantum wires, quantum wells and bulk structures. This chapter is dedicated to the review of one of the several families of methods used to fabricate semiconductor structures with 3D confinement, namely, via epitaxial growths.

Comparing to other techniques of synthesizing quantum dots including gas phase synthesis [1], phase segregation in solid state upon high temperature anneal [2], etc., epitaxial growth offers the unique advantage of an atomically continuous interface between the quantum dots and the surrounding matrix. This means the absence of interface states and defects that could cause carrier scattering and accelerated recombination of minority carriers allowing for coherent charge transport and highly efficient injection of minority carriers.

It is well known that the growth mode of epitaxial thin films can be categorized into three types: Frank van der Merwe, Stranski-Krastanow, and Vomer-Weber. The three growth modes describe layer-by-layer, layer-by-layer followed by islanding, and island growth, respectively. The underlying physics that drives these growth modes are relatively well understood. For a given combination of the film and substrate materials, the prevailing growth mode is determined by the configuration that has the lowest free energy. In addition to the entropic component, the total free energy consists of the following enthalpic component: the film surface energy, the substrate surface energy, the interface energy, and the strain energy due to lattice mismatch between the film and the substrate materials. At typical epitaxial growth temperatures that are well below the melting temperature, the entropic component plays a minor role comparing to the enthalpic components.

Accurate prediction of the equilibrium morphology in island growths is difficult. It is hindered by the lack of information with regard to the strain distribution inside individual islands and the surface energy. One feature common to materials with covalent bonding is surface reconstruction. All common semiconductor materials fall into this category. This is in clear contract to ionic or metallic bonded materials such as NaCl and most metals. This feature is as fundamental as the brittle mechanical property of covalently bonded materials. The surface energy of a given structure with covalent bonding is completely determined by the detailed surface reconstruction. One of the most significant consequences is that the surface energy is a function of both the magnitude and the sign of strain [3]. Experimentally, island formation is observed almost exclusively in films under compression as opposed to tension. The only exception we can find in the literature is for PbSe on PbTe(111). In that case the island surfaces are composed of perfect {100} facets with no surface steps present [4]. Such dependence of surface energy on the detailed atomic structure at the surface is absent from the traditional concept of surface energy.

In addition to the requirement of compressive strain, device applications further demand the presence of significant energy band edge discontinuity ($\gg kT$) between the island (quantum dot) and the surrounding matrix for confining carriers. For light emitting applications such as current injection lasers, the band edge discontinuity has to be in the fashion known as type I alignment for the simultaneous confinement of both electrons and holes inside the island.

There is a well-known trend in semiconductor materials relating to their respective position in the periodic table: The lower an element's position in the periodic table the larger the atom size becomes, and associated with the increased atomic size is the narrowing of the energy band gap as a result of electrostatic screening of the valence electrons by the electrons in the inner shells. Most of the well-studied semiconductor quantum dots grown by epitaxy are materials of larger lattice constant than the surrounding matrix. Examples include Ge quantum dots in Si matrix, InAs quantum dots in GaAs matrix, and GaN quantum dots in AlN matrix. The discussion of the current chapter focuses on two of the materials combinations: Ge on Si and InGaAs on Si. Quantum dots in other materials systems will only be mentioned briefly.

Despite the tremendous progress the research community has made towards the understanding of the self-assembly of semiconductor quantum dots by epitaxy, many of the key issues remain not understood. We highlight two of such issues below. The first one is the kinetic process of island size coarsening, also known as Oswald ripening. It remains largely not understood because of the difficulty in mapping out the chemical potential contour of surface adatoms. The non-uniform chemical potential is the direct consequence of the

non-planar surface topography and the associated non-uniformity of lattice strain on the surface. This in turn leads to the expected fluctuation in adatom diffusion coefficient and the associated adatom density fluctuation. From the experimental point of view, what further complicate matters is the un-avoidable intermixing between the substrate and the film materials. Available results on this subject will be reviewed.

Another subject that remains unclear is the atomic structure at the interface between a polar semiconductor such as GaAs and a non-polar material such as Si. Hetero-epitaxial structures such as GaAs on Si have obvious advantages for device applications and have been pursued with vigor as a result. The technologically important (001) crystallographic orientation of Si substrates is a polar direction for epitaxial GaAs in that the film is composed of alternate atomic layers of As (group V) and Ga (group III). It has long been recognized that a polar-non-polar interface cannot be an abrupt change between the two materials [5]. There has to be some sort of atomic rearrangement at the interface to mitigate the otherwise non-8-electron outer shell per interface atom and the associated prohibitively high interface energy. Several detailed atomic arrangement at such an interface have been proposed that could theoretically mitigate the problem of valence electron counting. Such arrangements remain to be verified by experiments. Furthermore, questions remain as to the kinetic pathway an actual interface formed during epitaxy can approach the ideal configuration.

Although the excitement in the subject of epitaxial growths of semiconductor quantum dots has subsided somewhat comparing to 15 years ago, it remains a fertile ground for scientific research and technology development. Many promising device applications remain to be realized. It is the goal of this chapter to further stimulates research interests on this subject and to help focus future research efforts.

This chapter consists of the following sections. First, a review of the various quantum dot based device applications is given. It begins with a discussion of the performance limitations of quantum dot lasers. Key parameters considered include threshold current density, multiple longitudinal modes versus single mode operation, the temperature sensitivity, and the modulation behavior. Quantum dot infrared photodetector is the second category of devices to be discussed. It is shown that such devices could potentially have performance rival that of HgCdTe detectors provided the dots are highly uniform in size and the density is sufficiently high. The last category of quantum dot devices is known as single electron devices. These devices explore the exceedingly small capacitance of the quantum dots and the associated large potential change upon the arrival of a single electron. This class of devices has been contemplated for both digital as well as analog applications. One coherent requirement emerges from the discussions pointing to the quantum dot size uniformity being the universal requirement for quantum dot based device applications. The subsequent sections discussing the epitaxial growth of quantum dots all have this principle in mind.

The next section provides a review of the current understanding of the physics governing the three growth modes commonly known as Frank-van der Mewer, Vomer-Weber, and Stranski-Krastanov. This is the physics background that facilitates the discussion of specific materials systems.

The following several sections provide detailed reviews of epitaxial growths of specific materials combinations. The review is presented in the order that proceeds from simple to more complicated situation. We start with the case of Ge on Si, InAs on GaAs, other less commonly studied materials combinations, and finally InGaAs on Si.

By presenting the topics in this fashion, we hope to provide the readers with a clear picture of the application potential of quantum dot based devices as well as an in-depth appreciation of the complexity, the intrigue and the challenges this field of science presents.

2. QUANTUM DOT BASED DEVICE APPLICATIONS

Due to the three-dimension quantum confinement, quantum dot system has special electrical and optical properties and shows great potential in photonic and electronic applications. The requirements on quantum dot system are application specific. Three groups of applications of quantum dots: quantum dot laser, quantum dot infrared photodetector (QDIP), and

single-electron device, will be examined to make clear which parameters of quantum dot system affect the device performances in each particular application.

Laser device is one of the most important applications employing quantum dots. Compared with quantum well laser, quantum dot laser has several significant advantages, such as low threshold operation [6, 7], high temperature stability [8], and high modulation frequency [9]. However, some of these advantages are degraded due to the difficulty in achieving structurally ideal quantum dots. Here we will discuss how the parameters of quantum dots affect the performance of the laser device.

Threshold current density is one of the key factors of laser device. Quantum dot laser is theoretically expected to have low threshold operation. But the quantum dot lasers in the early stage, which mainly realized by lithographic patterning, have higher threshold current density compared with quantum well lasers. The main reason of the high threshold current density is the high defect density due to process-introduced damage. Epitaxial self-assembled quantum dots, which have much lower defect density comparing to the lithographically defined ones, are more suitable for laser applications. The size uniformity of quantum dots is another very important factor affecting the threshold current density. Inhomogeneous broadening due to non-uniform quantum dot size is associated with broader gain spectrum, lower quantum efficiency, and higher threshold current density. Liu et al. [10, 11] have demonstrated very low threshold current density of 26 A/cm^2 using a single sheet of InAs quantum dots. Figure 1 [12] shows the historic development of threshold current density of different kinds of lasers.

The laser spectrum mainly depends on the size distribution of the quantum dots in a given material system. The peak of the size distribution determines the operation wavelength of laser, and the width of the laser spectrum is mainly affected by the size non-uniformity especially in quantum dot lasers. Despite of the observation of single mode operation by Kirstaedter et al. [13], quantum dot lasers typically operate in multi-mode oscillation even at very low injection levels. This is because of the quantum dot size non-uniformity induced inhomogeneous broadening leading to typical gain spectral width in the range of several 10 meV [14]. It is obvious that improving the size uniformity of quantum dots, thereby narrowing the gain broadening, is very important for single mode laser operation.

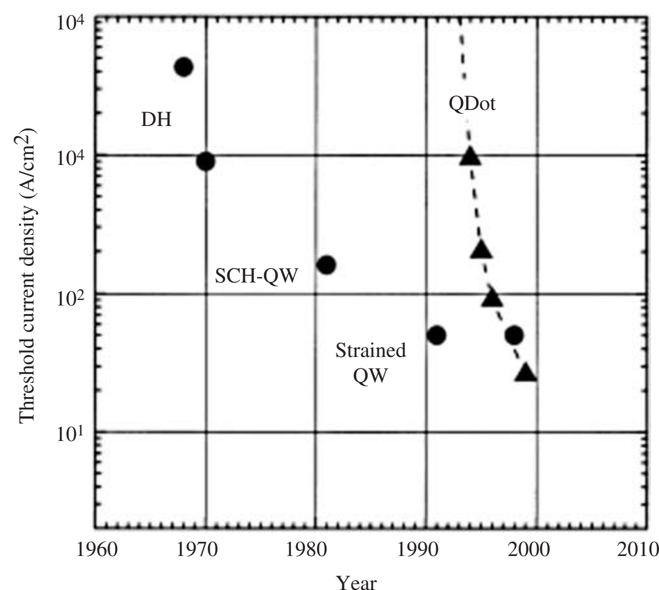

Figure 1. The historic development of the threshold current density of semiconductor laser diodes (as cleaved at room temperature). Circles denote double heterostructure (DH), separate connement heterostructure quantum well (SCH-QW) and lasers based on strained QWs. Triangles denote results obtained for QD laser diodes. Reprinted with permission from [12], "The Present Status of Quantum Dot Lasers," *Marius Grundmann* 5(3), 167–184 (2000). © 2000, Elsevier Science B.V.

The temperature-insensitivity is another advantage of quantum dot lasers. Zaitsev et al. [15] and Patane et al. [16] have shown slight decreases of threshold current density with temperature in the range of 10 K–100 K, which is believed due to the extreme non-equilibrium carrier distribution in the low temperature (see, for example, [17]). Above 150 K, threshold current of quantum dot lasers is found to increase slowly with temperature [18–20]. Such a threshold increase is mainly due to the leakage current and recombination in the barrier. To improve temperature stability, again a high quality coherent quantum dot system with very low defects density is required. Also, the barrier selection will be another issue when designing the quantum dot system.

The modulation behavior of laser device is very important for laser application with internal modulation. Frequency chirp is one of the most important reasons limiting the modulation frequency. In an ideal quantum dot laser, due to the δ-like density of state, there will be no frequency chirp. Because of the size non-uniformity, there is an inhomogeneous broadening in the real quantum dot system, which introduces the frequency chirp in laser operated under modulation. Despite of the ever-present quantum dot size non-uniformity, a very small chirp was observed by Choo et al. and Krebs et al. [21, 22], which is comparable with very good quantum well lasers. If the uniformity of quantum dot size is improved, much better modulation behavior can be expected.

Quantum dot infrared photodetector (QDIP) is another important application of quantum dot system. It is the only promising candidate to rival the current HgCdTe detectors in mid-infrared applications. Compared with quantum well infrared photodetector (QWIP), QDIP has two major advantages. One is that it can operate under normal incident since there are no polarization selection rules in quantum dot system. This feature makes the design of the detector structure much easier compared with QWIP, which need complicated grating and coupling structure to accommodate normal incidence. Another is that it has low dark current, large detectivity, and better response at elevated temperature [23, 24] due to the suppression of electron-phonon scattering in quantum dot system. This feature leads to longer lifetime of excited electrons [25, 26]. The superior high temperature behavior permits QDIP to operate with cost efficient cooling systems.

The dark current of a detector is a very important figure of merit for detector performance. Here we compare the temperature dependence of dark current in HgCdTe, QWIP and QDIP detectors. Figure 2 shows dark current as a function of temperature for different kinds of detectors. It is clear that the dark current of QWIP is much higher than that of QDIP, even in the quantum dot system with worst size uniformity. When the uniformity of quantum dot size improves, the dark current of QDIP approaches that of HgCdTe. With increasing

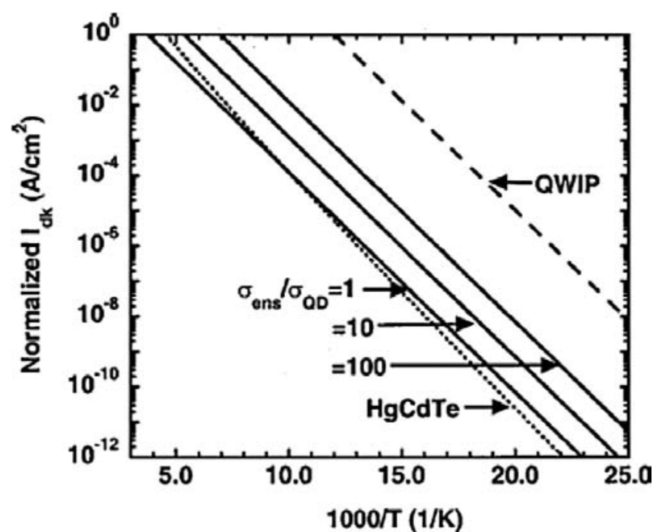

Figure 2. Normalized dark current for HgCdTe, QWIP, and QDIP detectors as a function of temperature with a band gap energy of 10 μm. Reprinted with permission from [24], Jamie Phillips, "Evaluation of the Fundamental Properties of Quantum Dot Infrared Detectors," 91(7), 4590–4594 (2002). © 2002, American Institute of Physics.

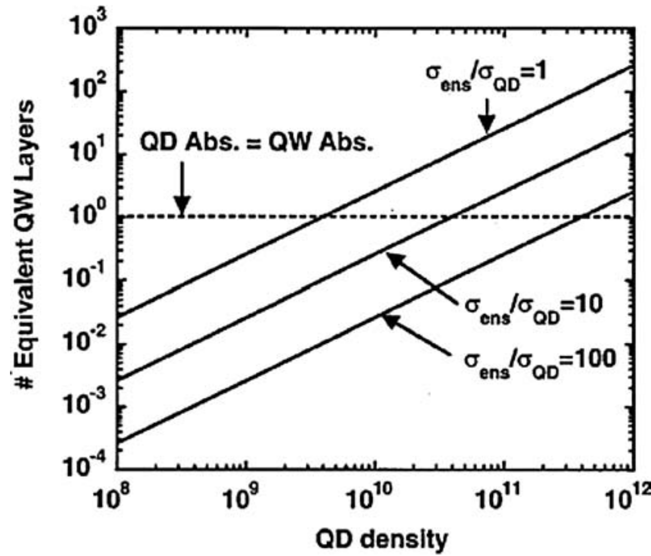

Figure 3. Quantum dot layer peak absorption equivalence compared to a single GaAs quantum well for varying QD uniformity. Reprinted with permission from [24], Jamie Phillips, "Evaluation of the Fundamental Properties of Quantum Dot Infrared Detectors," 91(7), 4590–4594 (2002). © 2002, American Institute of Physics.

temperature, the dark current of HgCdTe increases faster than that of QDIP, making QDIP the detector of choice for high temperature operation.

To achieve high detectivity, strong absorption in the active layer is requirement. This requires high quantum dot density. Quantum dot density higher than 10^{10} cm^{-2} is necessary to provide adequate absorption as shown in Fig. 3. This is especially true when the dot size uniformity is poor. Consequently, good size uniformity and high dot density are both required to improve the absorption in the quantum dot system.

We now compare detectivity, which is the most important figure of merit of a detector, among the three kinds of detectors, the HgCdTe detector, QWIP, and QDIP. From Fig. 4 we can find that the detectivity of QDIP is much better than that of QWIP within the entire temperature range from 40 K–250 K. QDIP with better uniformity has better detectivity illustrating once again that quantum dot size uniformity is very important for the performance

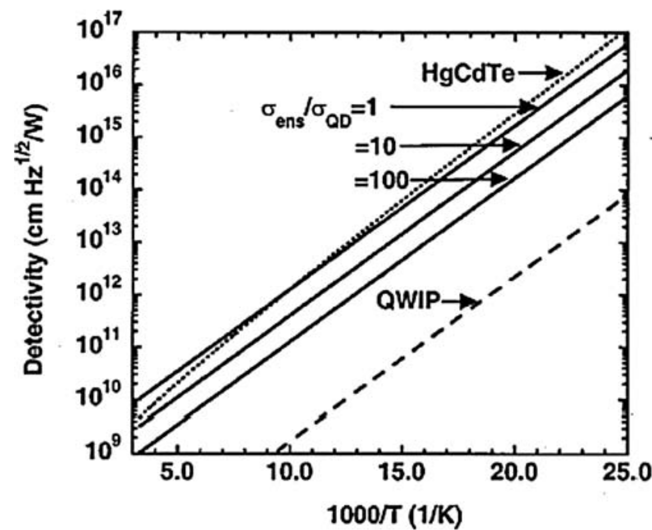

Figure 4. Detectivity for HgCdTe, QWIP, and QDIP detectors as a function of temperature with a band gap energy and incidence wavelength of 10 μm. Reprinted with permission from [24], Jamie Phillips, "Evaluation of the Fundamental Properties of Quantum Dot Infrared Detectors," 91(7), 4590–4594 (2002). © 2002, American Institute of Physics.

of QDIP. The predicted comparable detectivity and better high temperature performance of QDIPs with uniform dot size makes it the toughest competitor to HgCdTe as the material of choice for IR detector applications.

Single-electron devices represents yet another promising application of semiconductor quantum dots. The large change in the energy (comparing to kT) of a quantum dot upon the addition or subtraction of one single electron making it possible for this class of devices to operate at even room temperature if the dot size is smaller than 10 nm. This class of devices is expected to have advantages for both analog and digital applications such as single-electron transistor [27], background-charge-insensitive memory [28], nonvolatile random-access memory [29], supersensitive electrometry [30, 31], single-electron spectroscopy [32], DC current standard [33], and temperature standard [34].

The change in energy of a quantum dot upon the addition of one single electron, which is critical for the quantum dot-based single-electron device, is mainly determined by the size and shape of the quantum dot in a given material system. Thermal fluctuations on the order of kT suppress most single-electron effect unless the energy associated with the addition of one electron is about ten times larger than kT. For room temperature operation, this energy should be on the order of 100 meV. Such large electron addition energy requires a relatively small quantum dot size, typically less than 10 nm. Figure 5 shows a simple calculation of this energy as a function of quantum dot size. What further complicates the matter is that in quantum dot of such small sizes, the energy level is also very sensitive to the shape of the quantum dot. As a result, precise control of dot size and shape is one of the most important challenges of quantum dot fabrication for single-electron device applications.

Precise control of the placement of quantum dots is another fabrication challenge for single electron device applications. To make an ordered quantum dot array, or furthermore to fabricated quantum dots at the designed site of the substrate, is always required in the single-electron device application. To date, quantum dots fabricated using advanced lithographic patterning is the only way to meet such requirement. Even with the state of arts of lithographic technology, to make device with a-few-nm minimum feature size across the area of a wafer is currently not achievable.

In the above discussion of different applications of quantum dots, we can see that for different applications, there are different requirements for quantum dots fabrication. Laser applications require low defect density and good size uniformity. QDIP applications require

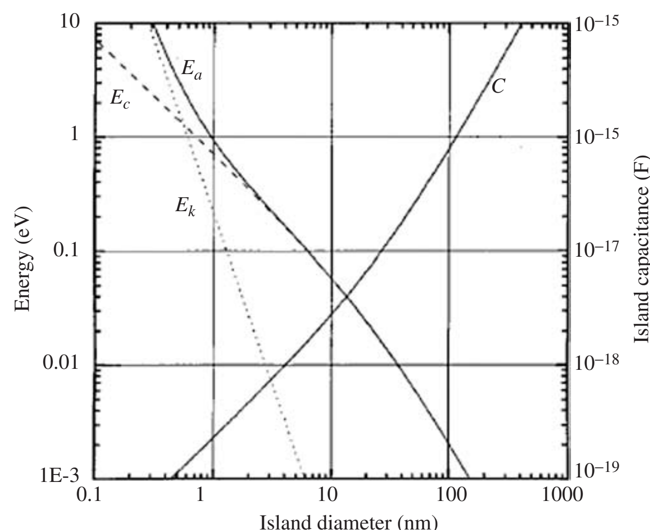

Figure 5. Single-electron addition energy E_a (solid line), and its components: charging energy E_c (dashed line) and electron kinetic energy E_k (dotted line), as calculated using (1) and (2) for a simple model of a conducting island. In this model, the island is a round three-dimensional (3-D) ball with a free, degenerate electron gas (electron density $n = 10^{22}$ cm; effective electron mass $m = m_0$), embedded into a dielectric matrix (dielectric constant $\varepsilon = 4$), with 10% of its surface area occupied by tunnel junctions with a barrier thickness of 2 nm. Reprinted with permission from K. K. Likharev, “Single-Electron Devices and their Applications,” 87(9), 606–632 (1999). © 1999, IEEE.

high dot density and very uniform dot size. And for single-electron devices, the precise control of dot size, shape and location are the most important concerns in dot fabrication.

3. THREE GROWTH MODES

In heteroepitaxial growth, three growth modes have been generally distinguished. These are Frank van der Merwe (FM), Volmer-Weber (VW), and Stranski-Krastanov (SK) growth modes. As shown in Fig. 6, the modes can be described as layer-by-layer growth, island growth, and layer-plus-island growth, respectively. Layer-by-layer growth mode stems from the strong bonding between the atoms in the film and that of the substrate. When the atoms of the film are more strongly bond to each other than they are to the substrate, the three-dimensional islands form such as Si on Ge. In layer-plus-island growth mode, the first several monolayers of the deposited material grow in layer-by-layer mode. This thin layer is known as the wetting layer and satisfies the condition of $\gamma_i + \gamma_f < \gamma_s$, where γ_i, γ_f, and γ_s represent surface energies of interface, film, and substrate, respectively. The wetting layer is strained due to significant lattice mismatch between the film and the substrate. Following the formation of the wetting layer of several atomic layers thick, islands are formed in order to elastically reduce misfit strain energy.

$2 \times n$ reconstruction is formed during the growth of the wetting layer when Ge is grown on Si (001). In this structural rearrangement, vacancies are formed on the surface and their mutual interactions lead to the formation of a periodic line structure where every nth dimer in each row is replaced by a vacancy. The missing dimer trenches relieve part of the elastic strain caused by dimerization. The vacancy formation energy is lowered via the re-bonding of the second-layer atoms. Nurminen et al. reveal that the optimal value of n strongly depending on Ge coverage. It decreases as Ge is first grown on the surface and then saturates to $n = 8$ at about 2 ML coverage.

One way to make such self-assembled quantum dots (SAQDs) is the use of a strained epitaxial layer to create small islands over a wider band gap semiconductor substrate. The epitaxy of quantum dots uses the transition from the two-dimensional (2-D) layer growth to three-dimensional (3-D) island growth that takes place during the deposition of a pseudomorphically strained epitaxal layer. Heteroepitaxial growth of highly strained structures has gained interest lately because it offers the possibility to fabricate islands with very narrow distribution in their size without any substrate patterning process or surface treatment. Quantum dot formation has been observed for a wide range of material/substrate combinations, including InAs/GaAs, InGaAs/GaAs, InP/GaAs, SiGe/Si, and Ge/Si. Among all these different materials combinations, Ge/Si represents the simplest system.

There have been a great number of approaches for fabricating semiconductor quantum dot arrays of uniform size and shape with regular spatial distribution. In order to achieve this goal, it is essential to advance the understanding of the formation mechanism of Ge quantum dots. The formation mechanism is still obscure. The issue of thermodynamics is complicated by the following unknown effects. These include interdiffusion between quantum dots and substrate, the resulting non-uniform composition of individual quantum dots, non-uniform distribution of quantum dots across the substrate surface, local strain field at

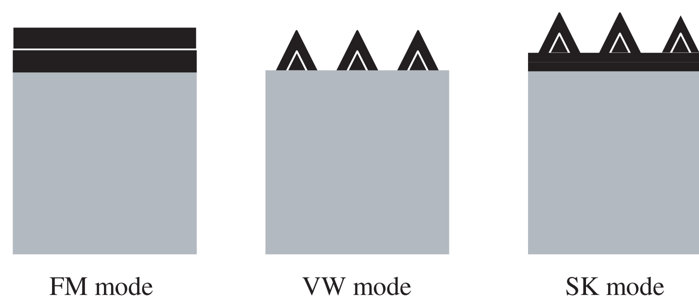

Figure 6. Schematic of three growth modes in heteroepitaxial growth; Frank van der Merwe (layer-by-layer), Volmer-Weber (island), and Stranski-Krastanov (layer-plus-island) growth modes.

subsurface, surface energies associated with the facets of different shaped quantum dots, and the possible dot size-dependent energy configuration. On the other hand, the prevailing morphology from a particular fabrication process could be extensively limited by kinetics. The key elements influencing the kinetic process are the surface diffusion of adatoms during the growths of the wetting layer (2-D) as well as quantum dots (3-D), adatom density, dot nucleation density, and Oswald ripening (also known as coarsening). All these parameters are determined by experimental variables, such as substrate temperature, growth rate, and cleanliness of substrate surface. The ability to de-couple the effects of each of these experimental variables will allow us to clearly understand the formation mechanism of Ge quantum dots. For example, a high substrate temperature during dot growth enhances the surface diffusion of Ge adatoms, but also increases interdiffusion, leading to the higher Si concentration in Ge quantum dots. Now we will discuss the influence of the misfit strain within quantum dots on the size and shape of Ge quantum dots, followed by the nucleation and growth of Ge quantum dots at three distinct surface sites on the relaxed $Si_{1-x}Ge_x$ buffer layer. Finally, a new method will be introduced for the quantitative observation of surface diffusion processes as a function of the substrate temperature and the growth rate of Ge.

4. Ge QUANTUM DOT ON Si

Since the observation of pyramidal Ge islands formed on Si (001) by epitaxy in the early 1990s, there have been substantial interests in fabricating dense and uniform self-assembled Ge quantum dots. As a heterostructure of elemental semiconductors, they both have diamond structure with no chemical mismatch (polar-nonpolar interaction). Ge has 4.2% lattice mismatch with Si. From the perspective of materials science in fabricating quantum dots via epitaxy, this is the simplest heterostructure to study. Significant progress has been made during the past one and half decade. Systematic experimental observations have been made with respect to the dot shape evolution during growths, critical dot size for dislocation, and Oswald ripening. Despite of these progresses, there remain quite a few issues regarding Ge dot formation on Si (001) not understood. One such issue is the physics governing the preferential nucleation of Ge dots over buried dislocations and the other is the real function of surfactants such as Sb. In this section, the subjects of pyramid-to-dome transition and vice versa, two-step growth and nucleation of Ge islands, and finally surface diffusion of Ge adatoms are discussed.

4.1. Pyramid to Dome Transition

Ge films grown on Si follow the SK growth mode. The thickness for the transition from two-dimensional to three-dimensional growths is around 3 monolayer (ML). After the wetting layer is finished, Ge adatom density starts to increase until the critical supersaturation value is reached when Ge islands start to nucleate. These Ge islands (we use the terms islands and dots interchangeably throughout the text) have the shape of square-based pyramid with {105} facets. The characteristic aspect ratio is typically 1 : 10. The pyramidal islands are also known as huts from the early studies of Mo et al. [35]. As island size increases, there exists a critical size with the appearance of higher aspect ratio facets such as {111} and {113}. These multi-faceted islands are conventionally known as domes. The transition from pyramid to dome appears to be associated with a gradual change in the island volume that is evidenced by the nearly constant island base size during the transition. Growths of Ge islands on Si (001) without paying special attention to the island size uniformity typically result in what is known as the bimodal distribution consisting both pyramids and domes.

A qualitative model of the underlying thermodynamics is proposed by Ross et al. in which a crossover point exists in the Gibbs free energy (G) versus island size curves, [36] which is shown in Fig. 7. They also observe some transition states between pyramids and domes during Ge/Si island growth [37]. The critical island size at which pyramid-to-dome transition actually takes place is slightly larger than the island size for G crossover. It actually occurs at the point when the chemical potential (μ) for pyramids and domes crosses over one another. The key point of this model is that the pyramids are the thermodynamically stable

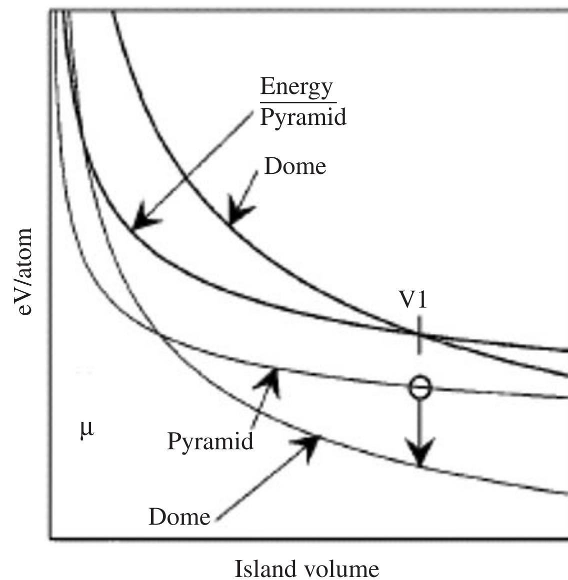

Figure 7. Energy per atom and chemical potential (μ) of islands with two types of facets with values of α in the ratio 1:2, The shape transition occurs at volume V1, where the energy curves cross, at which point there is a discontinuity in μ. Reprinted with permission from [36], F. M. Ross et al., "Coarsening of Self-Assembled Ge Quantum Dots on Si(001)," *Phys. Rev. Lett.* 80(5), 984–987 (1998). © 1998, American Physical Society.

configuration of Ge islands when their sizes are small as opposed to the possibility that the pyramids are a product of kinetically limited crystal growths. This model is derived from the extensive experimental studies by several research groups across the world, especially that from Kamins et al. [38].

The careful study of Kamins et al. [4] also reveals that the pyramid-to-dome transition is reversible. In other words, there can be a dome-to-pyramid transition. The study shows that for Ge islands on Si (001) grown at 650 °C followed by anneal at the same temperature, significant intermixing occurs between Ge and Si as evidenced by $\theta/2\theta$ X-ray diffraction. After anneal for 20 minutes, some dome-shaped islands start to change their shapes. One side of the base starts to expand outward and form the additional {105} facet as shown in the atomic-force micrograph in Fig. 8. The steep facets of a dome can often be seen superposed on top of the pyramid. The corners of these transition pyramids are not well defined. After anneal for 60 minutes, almost all of the dome-shaped islands changed into pyramid-shaped islands. Such a reverse transition is a direct product of the intermixing between Ge and Si that leads to a reduced misfit strain in the now SiGe alloy islands (instead of the original nearly pure Ge islands).

For Ge islands grown on Si, the minimum G configuration comes as a tradeoff between the increase in surface energy and the associated decrease in misfit strain energy due to side wall flexing. When intermixing between Ge and Si becomes significant upon extended anneal at high temperatures, the crossover point in the G versus island size curve shifts towards the right, i.e., towards the direction of large island sizes. An island of nearly pure Ge that used to be above the pyramid-to-dome transition point now falls below the shifted pyramid-to-dome transition size for SiGe islands. As a result, dome-to-pyramid transition takes place.

From the perspective of thermodynamics, the system can be considered as a closed system since the growth is stopped. Extended anneal brings the system from a local G minimum towards the global equilibrium. The dome-to-pyramid transition represents one inter-mediate stage of the system on its way to the global equilibrium, which is a near ball shape facetted SiGe block with uniform composition.

Device applications often prefer layered structures being capped with Si. The growth of Si over Ge islands is another interesting and non-intuitive process that has been investigated in detail by Yam et al. [39] using reflection high energy Electron diffraction (RHEED),

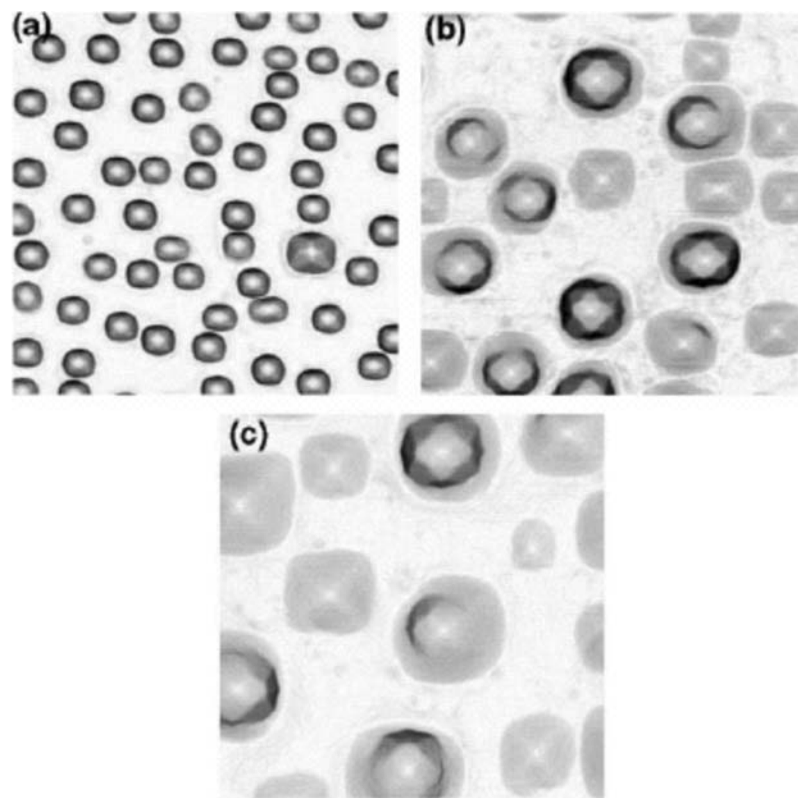

Figure 8. Plan-view, atomic-force micrographs of Ge islands deposited on Si (001) at 650 °C to a thickness of 11 equivalent relaxed Ge monolayers. (1 μm × 1 μm areas displayed.) (a) After deposition; (b) After annealing for 20 min at 650 °C; (c) After annealing for 60 min at 650 °C. The images have been processed to emphasize the slopes of the facets. Darker shading corresponds to the steeper facets of domes; medium gray corresponds to the shallower {105} facets of pyramids. Reprinted with permission of from [38], T. I. Kamins et al., "Dome-to-Pyramid Transition Induced by Alloying of Ge Islands on Si (001)," *Appl. Phys. A* 67, 727–730 (1998). © 1998, Springer-Verlag.

atomic force microscopy (AFM), transmission electronic microscopy (TEM), and photoluminescence. Their results clearly show that there are three stages in the capping process. The first stage consists of dome-to-pyramid transition with increasing islands density and volume. The second stage involves the gradual transformation of pyramidal shape islands to domes. The third and final stage is the smoothening of surface. And even if the Si capping thickness is higher than the island height, the surface is still not flat enough. A strong surface roughness (~10 Å) is correlated with the mechanism of the vertical alignment of Ge islands on Si for the superlattice structure.

Now we discuss a new technique to minimize the interdiffusion between Ge dots and a Si substrate. Size and shape uniformity are the two most important parameters when self-assembled quantum dots are considered for device applications. The existence of pyramid and dome of Ge dots on Si (001) has been extensively investigated for the principle of dot size and shape changes. However, less information regarding to nonuniform strain distribution in a dot [40] and reconstructed atomic arrangement in facet planes [41] is the main difficulty for considering the strain energies and surface energies of pyramid and dome, respectively. The former can be significantly varied by the experimental variables and is dependent on the aspect ratio of the dot and the interdiffusion induced nonuniform composition within dots [42]. The latter has not been studied in detail for the different shapes of Ge dots such as {105} facet in a pyramid and a multifaceted dome.

The presence of Si in Ge dots determines the misfit strain as well as the energetically stable shape. In particular, Si atoms diffused from the substrate into Ge wetting layer at the early stage of Ge dots growth keep diffusing into Ge dots, resulting in broad size and shape distributions. Figure 9 depicts the possible interdiffusion occurring at relatively high temperature. The interdiffusion is inevitable due to the complete solid solubility between Si

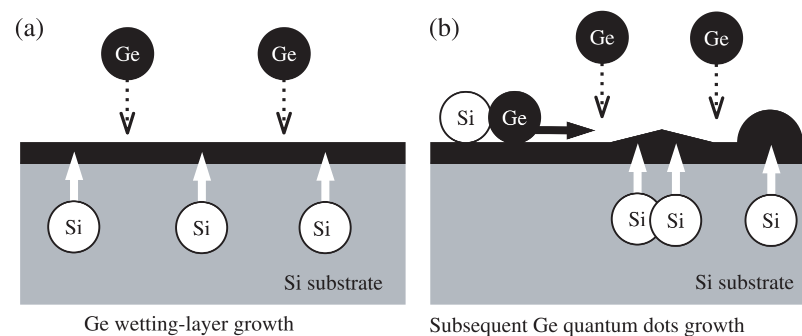

Figure 9. Schematic diagram representing the interdiffusion between Ge quantum dots and Si substrate.

and Ge through a wide range of temperature [43]. The bulk diffusion of Si in Ge occurs via monovacancy mechanism. Räisänen et al. proposed 2.4 eV and 0.24 cm^2/s for the activation energy and pre-exponential factor, respectively, in the temperature range of 650–900 °C [44]. This result implies a strong Si diffusion during Ge dots growth. High substrate temperatures accelerate the interdiffusion so that resulting in the lower misfit strain as well as the broader size and shape distributions.

The morphology of 7.0 Å Ge coverage on bulk Si (001) substrates is shown in AFM images of Fig. 10. Ge dots are not only randomly situated but also non-uniformly spaced. The only difference between the two samples is the growth temperature for the wetting layer, 650 °C and 280 °C for Fig. 9(a) and (b), respectively. The resulting size uniformity of dots between the two samples represents a clear contrast. The one-step sample [Fig. 10(a)] exhibits tri-modal distribution in size and shape. These include pyramids, domes and superdomes as described in references [45, 46] with population ratio of about 6:3:1. This multimodal distribution of Ge quantum dots is significantly suppressed in the two-step sample as shown in Fig. 10(b), The number of pyramid significantly decreases so that the population ratio of pyramid to dome is approximately 1:5 with no superdomes. The wetting layer grown at the low temperature of 280 °C results in much more uniform size and shape of dots.

At the initial stage of dots formation under a constant Ge flux of 0.05 Å/s, the base of pyramids keeps increasing in size with a constant aspect ratio of about 1:9(±1) until its base width reaches the critical value at which point conversion from pyramids to domes occurs. The aspect ratio is in approximate agreement with {105} facets [47]. The domes have typical aspect ratio of 1:5.5(±1). The biggest pyramid has similar base area as domes in both samples consistent with [48].

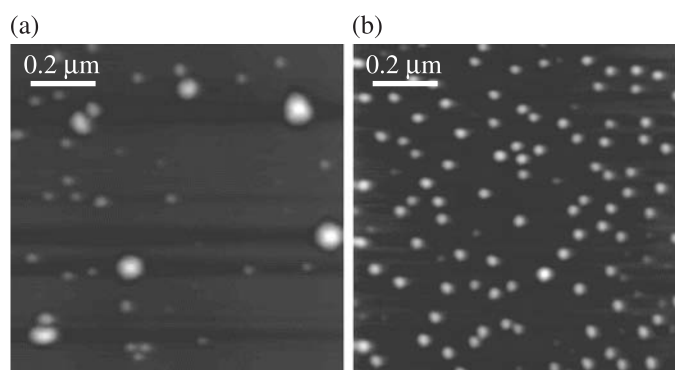

Figure 10. Two-dimensional AFM topographic images of 7.0 Å Ge coverage on Si (001) substrate without a buried misfit dislocation network; (a) One-step sample (the height of highest dot = 344 Å) (b) Two-step sample (the height of highest dot = 92 Å). Reprinted with permission from H. J. Kim and Y. H. Xie, "Influence of the Wetting-Layer Growth Kinetics on the Size and Shape of Ge Self-Assembled Quantum Dots on Si(001)," *Appl. Phys. Lett.* 79(2), 263–265 (2001). © 2001, American Institute of Physics.

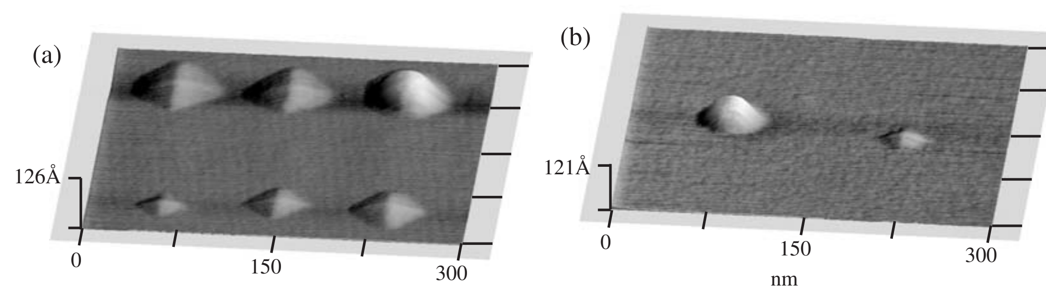

Figure 11. Three-dimensional AFM images of the samples with 6.0 Å Ge coverage; (a) One-step sample (b) Two-step sample. Reprinted with permission from H. J. Kim and Y. H. Xie, "Influence of the Wetting-Layer Growth Kinetics on the Size and Shape of Ge Self-Assembled Quantum Dots on Si(001)," *Appl. Phys. Lett.* 79(2), 263–265 (2001). © 2001. American Institute of Physics.

Interestingly, the biggest pyramid sizes of one-step samples are lager than those of two-step samples. Figure 11 displays 3-D AFM images of one-step and two-step samples with 6.0 Å Ge coverage. Ge dots are grown on relaxed $Si_{0.75}Ge_{0.25}$ buffer layers. The buried misfit dislocations located at the interface between the buffer layer and Si (001) substrate are effective for inducing preferential nucleation. The buried dislocation density can be controlled by Ge concentration of $Si_{1-x}Ge_x$ layer.

Bimodal distribution in both samples facilitates the identification of base width between the biggest pyramid and smallest dome. The critical size of pyramid-to-dome transition in the one-step sample (~660 Å) [Fig. 11(a)] is significantly larger than that in the two-step sample (~505 Å) [Fig. 11(b)].

There are two important and interrelated observations when the growth temperature of the wetting layer is lowered. First, a significantly reduced fraction of pyramids for comparable amount of Ge deposited. Second, the dot size at which the transition from pyramids to domes occurs is reduced. The dot size and shape uniformity are improved across a wide range of dot sizes.

One of the most significant consequences expected from lowering the growth temperature of the wetting layer is to minimize alloying between Si and Ge. Interdiffusion of Si from a substrate into Ge wetting layer has been observed in samples with Ge deposited at room temperature and annealed at temperature as low as 300 °C [49]. It reduces the misfit strain in Ge dots. Continuous supply of Si to the surface when the wetting layer is completed is through bulk diffusion. The rate of supply of Si to the wetting layer surface is estimated to be much slower than the arrival rate of Ge per unit surface area based on the result of Nakajima et al. As a result, the dot composition changes rapidly (within a 2.0 Å of additional Ge) upon the completion of the Ge wetting layer to nearly 100% Ge. This explains why the difference between one-step and two-step samples is most significant only up to certain Ge coverage, in our case that coverage is 7.0 Å.

The major effect of growing wetting layer at low temperatures is to suppress the initial rapid alloying between Si and Ge when there is only a fraction of monolayer coverage of Ge on bare Si surface. Surface processes proceed with lower activation energy because there are fewer bonds to break, and therefore they proceed much faster than bulk process such as diffusion through the wetting layer. This initial surface process is likely to affect the Si concentration in Ge dots at the early stage of their formation. A Si atom at the surface needs only to break two bonds (instead of four bonds as in bulk case) to move freely around the surface and mix with incoming Ge adatoms. Since this process is important only when Si surface is exposed, the effect is at most on the order of one monolayer, i.e., $>10^{15}$ Si atoms per cm^2. In the case of Ge dots on Si, the amount of Ge involved is on the order of a few angstroms, i.e., 3–4 monolayers. As a result, the interdiffuson resulting from an exposed Si substrate surface at high temperatures could lead to a maximum of 30% difference in Ge dot composition. A composition variation at that level results in clearly observable changes in the critical island size for pyramid-to-dome transition.

The model of Ross et al. includes an abrupt change in the chemical potential when a critical dot size is reached. The experimental results suggest that the critical size is a sensitive function of the misfit strain, and increases with decreasing strain.

The critical size of Ge dots as a function of the misfit strain influenced by another important factor will be discussed. The critical size of Ge dots is larger when they are grown over the buried dislocations acting as underlying stressors.

This particular relaxed buffer layer causes two clearly different regions distinguished by the spatial distribution of Ge dots because it provides considerably larger dislocation spacing than average surface diffusion length of Ge adatoms. As a result, there coexist the preferential and random distributions over the dislocation lines and in the region between dislocations, respectively. The sizes of the biggest pyramid and the smallest dome in the two regions are carefully measured. Figure 12 shows 3-D AFM images of Ge dots grown over the buried dislocation line and in the region between dislocations. The resulting critical sizes from the two regions are significantly different. In spite of the fact that the arrival rate of Ge flux per unit area is same in the two regions, the critical size of dots along the dislocation lines (547 ± 10 Å) [Fig. 13(a)] is larger than that in the region between the dislocations (476 ± 10 Å) [Fig. 13(b)]. The total number of the biggest pyramids within this size range comprised less than 2% of all the pyramids investigated by AFM. The biggest pyramids in both (a) and (b) showed the same aspect ratio of 1 to 9.7(±1).

Figure 13 shows the corresponding plan-view TEM image representing the ordering of Ge dots along two sets of the buried dislocations in the relaxed $Si_{0.85}Ge_{0.15}$ buffer layer. Each array of dots is not only clearly associated with a single buried dislocation, as opposed to dislocation pile-ups, but is also observed on one side of the buried misfit dislocations. In spite of the higher dot density in the sample the TEM image of low magnification exhibits only relatively big dots such as 200 Å tall dots. Projections of Burgers vectors onto the interface plane are marked with arrows. There are two possible slip planes corresponding to each possible Burgers vectors for a 60° misfit dislocation line. The 60° dislocation lying in the $[\bar{1}10]$ direction can have either (111) or $(\bar{1}\bar{1}1)$ slip planes. Two possible Burgers vector directions of $[0\bar{1}1]$ and $[\bar{1}01]$ and another two of [111] and [011] correspond to (111) and $(\bar{1}\bar{1}1)$ planes, respectively. Therefore the Burgers vector analysis allows us to find the corresponding slip plane of the dislocation.

Ross showed the strain field variation of the top surface due to buried dislocations using 2-D linear strain analysis [50]. The lowest energy sites occur at the intersection between the slip plane and the top surface where islands preferentially nucleate.

The average distance (650 ± 13 Å) between the dislocation line and the array of Ge SAQDs, in Fig. 13, approximately agrees with the calculated value (640 Å) that is the lateral distance from the buried dislocation to the position where the {111} slip plane intersects the top surface of the 900 Å thick buffer layers. A dashed line links the centers of the dots that belong to a buried dislocation.

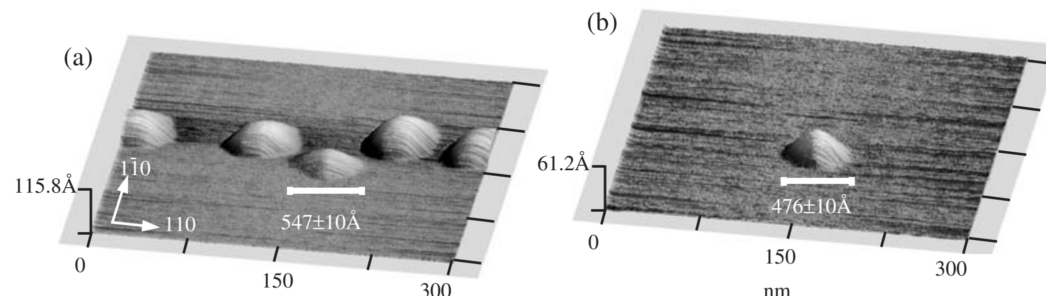

Figure 12. Three-dimensional AFM images of two-step sample with 5.0 Å Ge coverage on the relaxed $Si_{0.85}Ge_{0.15}$ buffer layer; (a) shows arrays of Ge quantum dots grown over the intersections between the slip planes and the top surface and (b) shows a pyramid in the region between the dislocations. Reprinted with permission from H. J. Kim et al., "Influence of a Buried Misfit Dislocation Network on the Pyramid-to-Dome Transition Size of Ge Self-Assembled Quantum Dots on Si(001)," *J. Crystal Growth* 247(3–4), 251–254 (2003). © 2003, Elsevier Science Direct.

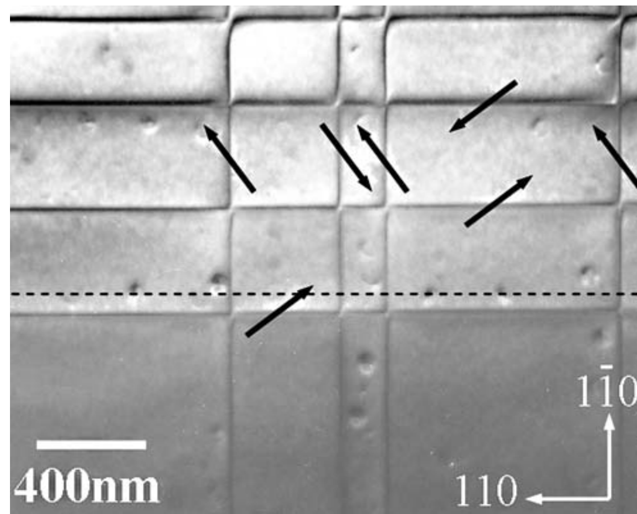

Figure 13. A plan-view TEM micrograph of the sample with Ge quantum dots grown on the relaxed $Si_{0.85}Ge_{0.15}$ buffer layer is shown. Reprinted with permission from H. J. Kim et al., "Influence of a Buried Misfit Dislocation Network on the Pyramid-to-Dome Transition Size of Ge Self-Assembled Quantum Dots on Si(001)," *J. Crystal Growth* 247(3–4), 251–254 (2003). © 2003, Elsevier Science Direct.

It is evident from the experimental observations that the preferential nucleation of dots along the dislocation lines is the direct result of the lower misfit strain in dots. The clear contrast in the critical sizes of dots further illustrates the fact that a larger critical size is associated with lower misfit strain. This is in agreement with the result of a previous section, where the difference of the misfit strain was caused by the interdiffusion. For the precise reason of avoiding interdiffusion, low-temperature wetting layers were used for the sample studied in this work. Therefore, the strain field of buried dislocations can be considered the additional factor influencing the critical size of Ge dots grown on relaxed $Si_{1-x}Ge_x$ buffer layers.

When the average spacing of the underlying stressor dislocation is much larger than the surface diffusion length of adatoms, three types of surface sites can be distinguished. The three types of sites include those over the dislocation intersections, those over single dislocation lines, and those far away from dislocations. We designate them site *A* (points), *B* (lines), and *C* (surface area), respectively.

From the viewpoint of adatom density, the SK growth mode itself is an interesting contrast to homoepitaxial growths of Si on Si that proceeds in Frank-van der Merwe (FV) mode. The latter has been studied in detail by Mo et al. and has been shown to grow via either step propagation or 2-D island nucleation and coalescence [51]. As a result, the adatom density reaches a steady state value for a given incident molecular flux and remains at that value throughout the rest of the growth process. SK growths such as Ge on Si or InAs on GaAs, on the other hand, go through FV mode during the first couple of monolayer (ML) coverage, i.e., during the formation of the wetting layer. At the completion of the wetting layer formation, surface steps cease functioning as sinks for adatoms and 2-D island nucleation and growth are prohibited energetically. As a result, the adatom density starts to increase linearly with time until it reaches the super-saturation value for the nucleation of dots. The three types of surface sites of the partially relaxed buffer layer have the difference in their in-plane lattice constants with the value at site *A* being the closest to that of unstrained Ge. Intuitively, such differences can translate into either a difference in the surface diffusion coefficient of the adatoms, in the wetting layer thickness, in the critical size of pyramid-to-dome transition, or all of the above.

AFM topographies of samples with Ge coverage of 4.0, 4.5, 5.0, and 6.0 Å are shown in Fig. 14(a)–(d). The first three images clearly illustrate the existence of three types of surface sites and the resulting three-stage nucleation over dislocation intersections (site *A*), single dislocation lines (site *b*), and in regions far away from dislocations (site *c*), respectively.

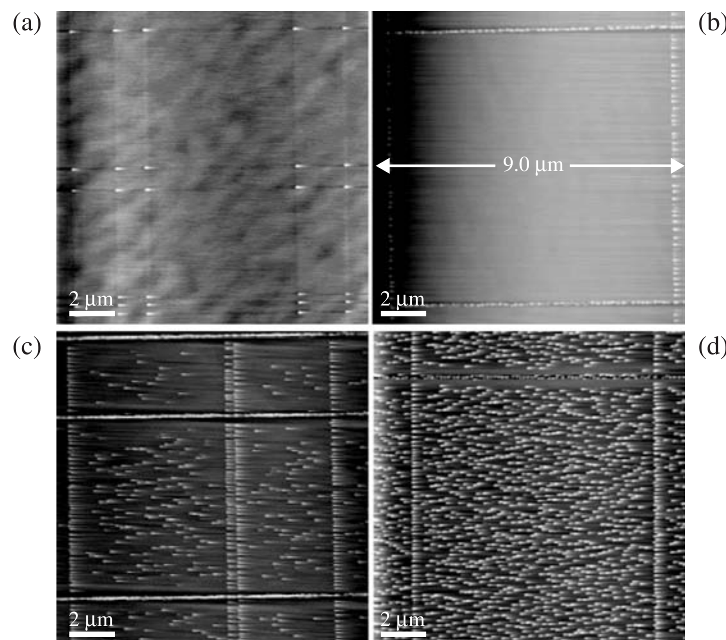

Figure 14. Two-dimensional AFM topographic images of Ge quantum dots with 4–6 Å coverage on a partially relaxed $Si_{0.9}Ge_{0.1}$ buffer layer. (a) 4.0 Å Ge coverage with Ge dots only at site A. (b) 4.5 Å Ge coverage with Ge dots at site A and B. (c) 5.0 Å Ge coverage with Ge dots at site A, B, and C. (d) 6.0 Å Ge coverage with Ge dots at site A, B, and C. Reprinted with permission from H. J. Kim et al., "Three-Stage Nucleation and Growth of Ge Self-Assembled Quantum Dots Grown on Partially Relaxed SiGe Buffer Layers," *Phys. Rev. B* 68, 205312–205317 (2003). © 2003, American Institute of Physics.

Three-stage nucleation is clearly shown as the Ge coverage increases. At 4.0 Å, Ge dots of pyramidal shape nucleate exclusively at *A* sites. These pyramids form a rectangular array with perfect registry to the network of buried dislocations. Additional 0.5 Å of Ge growth causes the preferential nucleation of Ge dots over dislocation lines. Figure 14(b) shows a large rectangle bordered by dislocations consisting of dots formed at *A* and *B* sites. Although the Ge coverage at this point is approximately the wetting layer thickness (established in the literature to be $\sim$3 ML $\approx$ 4.2 Å in the case of Ge grown on bulk Si (001) substrate [53]), it is important to notice that there is no dot in the region between dislocations. The dislocation spacing of $\sim 9\ \mu$m is much larger than surface diffusion length of Ge adatom reported in literature under similar conditions. The appearance of dots at sites *A* and *B* indicates that either the Ge adatom density is higher or the nucleation barrier is lower at these sites.

In an effort to differentiate between the two possibilities, surface topography immediately prior to the nucleation of any islands is examined in detail. The location of the buried dislocations is revealed by lines of steps such as the one shown in Fig. 15(a). Arrows indicate the step over a buried single dislocation line prior to Ge growth. Evidence of a higher density of Ge adatoms is observed at site B in the form of a ridge (not islands) of very low aspect ratio as shown in Fig. 15(b). The ridge height in samples with 3.0 Å Ge coverage is determined to be 7.5 ± 1.5 Å, a significant increase from the 2.9 ± 0.7 Å value in the sample with no Ge coverage. The original ridge height from samples with no Ge coverage agrees well with the observation by Lutz et al. who claimed a ridge height of 2.5 ± 0.3 Å for individual buried dislocations [54]. Although there are definite non-planarity at these sites, (001) remains to be the prevailing facets. The average terrace width of $\sim$240 Å calculated from the aspect ratio of the ridges is comparable to that on typical Si (001) surfaces. The only difference is the polarities of the "force dipole" at these steps are more aligned. We call these ridges "pile-ups" of Ge in order to differentiate them from dots. The lack of 3-D Ge islands at this Ge coverage indicates that the wetting-layer thickness ($>\sim$4.5 Å) at these sites is much thicker than at site C, presumably due to the much reduced misfit strain at

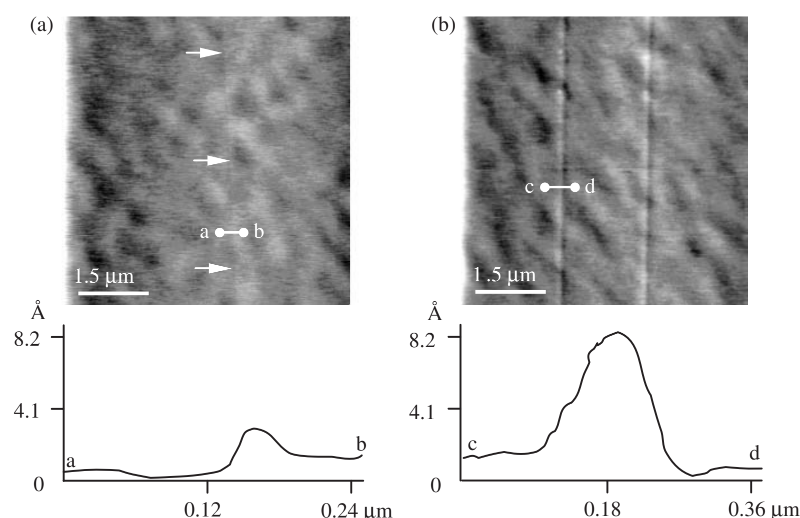

Figure 15. 2-D AFM topographic images of the sample; before Ge growth (a) and with 3.0 Å Ge (b). Arrows indicate the ridge on the top surface resulting from buried single dislocation. Line scan of a-b and c-d illustrates that ridge height is 2.9 ± 0.7 Å and 7.5 ± 1.5 Å, respectively. Reprinted with permission from, H. J. Kim et al., "Three-Stage Nucleation and Growth of Ge Self-Assembled Quantum Dots Grown on Partially Relaxed SiGe Buffer Layers," *Phys. Rev. B* 68, 205312–205317 (2003). ©2003, American Physical Society.

these sites. The above observation favors the higher Ge adatom density possibility over that of a lower nucleation barrier at *B* sites.

Similar "pile-up" of Ge is also observed at site *A*. There, due to the four-fold symmetry, the "pile-ups" are in pyramidal shape with extremely low (~1:145) aspect ratio. Furthermore, the aspect ratio seems to vary continuously with time, instead of staying at a constant value such as in the case of typical Ge pyramids on Si. The fact that no single facet is preferred indicates that such "pile-ups" of Ge are not dots. In other words, they do not represent energetically stable islands. Instead, they could be explained by the existence of a chemical potential gradient for Ge adatoms toward site *A* and *B* caused by the undulating strain field. Supporting this believe is the fact that such pile-ups are never observed at site *C*, where there is no directional diffusion of Ge adatoms.

In Fig. 16 the nucleation of Ge dots proceeds from point *A* to *B* along buried single dislocation. Dot size becomes smaller and the inter-dot spacing becomes larger as we move from the center towards the end of the dislocation half loop. This trend is symmetric towards the other end of the dislocation half loop. Three line scans reveal that ridge heights of *a*–*b*, *c*–*d*, and *e*–*f* are 7.2 Å, 4.8 Å, and 2.9 Å, respectively. This trend is a direct consequence that the accumulation of Ge adatoms by surface diffusion happens at a finite rate. The time it takes

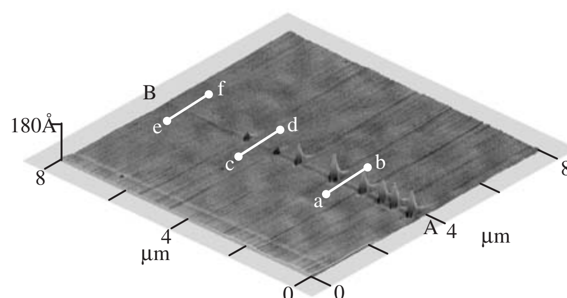

Figure 16. 3-D AFM topographic images of the sample in which the nucleation of Ge quantum dots proceeds along an underlying dislocation. Ridge heights across single dislocation of a-b, c-d, and e-f are ~7.2 Å, ~4.8 Å, and ~2.9 Å, respectively. Reprinted with permission from H. J. Kim et al.,"Three-Stage Nucleation and Growth of Ge Self-Assembled Quantum Dots Grown on Partially Relaxed SiGe Buffer Layers," *Phys. Rev. B* 68, 205312–205317 (2003). © 2003, American Physical Society.)

is comparable to the time it takes for the dislocation to expand by several μm. As a result, the time period during which directional surface diffusion happens is noticeably shorter near the end of the buried dislocation half loop comparing to that near the center. The ridge height of *e–f* is comparable to the one in samples without Ge growth corresponding to Fig. 15(a), whereas that of *a–b* is practically the value measured across any buried dislocation line in Fig. 14(a) or (b). The total length of this propagating buried dislocation is found to be $\sim$24 μm by following the ridge. Apparently, the dislocation half loop is introduced near the beginning of the Ge growth that took place at 700 °C. Such a substrate temperature is sufficient to allow a dislocation half loop to propagate at a rate that is on the order of a few μm per minute. Ge dots formed along the line is practically trailing the expanding dislocation, allowing us to observe the unfolding of such a dynamic process.

A partially relaxed buffer layer is an excellent experimental vehicle for the study of the various stages of nucleation and growth of dot following SK mode. There is a complex interplay of the directional surface diffusion of Ge adatoms with the different dot nucleation barrier at the various surface sites. The experimental results provide insight into the formation process of Ge dots on Si. At the same time, these results also raise more unknowns.

Following the evolution of Ge adatom density near the three types of sites on the surface, we can "trace" the formation of Ge dots on Si (001). At the beginning of the growth, Ge adatom density increases all across the sample surface. Together with this increase, directional diffusion takes place. There is a net flux of Ge adatoms from the surrounding region towards sites *A* and *B*, and the adatom density near these sites increases as a result. The wetting layer thickness at these sites is apparently much larger than on bulk Si surfaces. There is no SAQD nucleation at site *B* for Ge layer thickness values below $\sim$6.0 Å. Such a large wetting layer thickness can again be explained using the much lowered misfit strain between the dots and the substrate at site *A* and *B* comparing to that at site *C*. Intuitively, a zero misfit strain should lead to a wetting layer thickness approaching infinity.

Directional diffusion leads to a partial depletion of Ge adatoms near sites *A* and *B* that is later manifested as a "denuded zone" free of Ge dots. The extent of the directional diffusion is approximately the diffusion length during the experimental process and is on the order of μm. As a result, Ge adatom density in regions far away from site *A* and *B* is largely unaffected. It is expected to stay constant first until the completion of the wetting layer. At that point, step edges stop functioning as sinks for adatoms and 2-D nucleation becomes energetically unfavorable, Ge adatom density starts to increase with deposition time in a linear fashion. Figure 17 depicts the expected evolution of Ge adatom density with time.

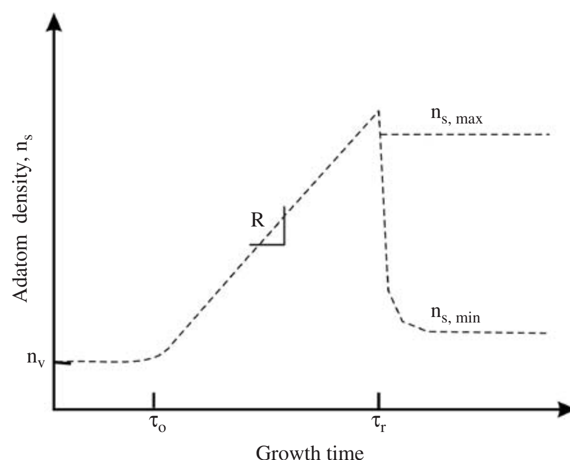

Figure 17. Schematic drawing of adatom density (n_s) as a function of growth time (t) at a growth rate of R. Wetting-layer completes at τ_o and 3-D quantum dots nucleation occurs at τ_r. n_v is equilibrium adatom density. Reprinted with permission from H. J. Kim et al., "Three-Stage Nucleation and Growth of Ge Self-Assembled Quantum Dots Grown on Partially Relaxed SiGe Buffer Layers," *Phys. Rev. B* 68, 205312–205317 (2003). © 2003, American Physical Society.

Under a growth rate of R the wetting layer completes at τ_o. The adatom density abruptly drops at τ_r with the nucleation of 3-D quantum dots.

Upon increase of Ge coverage, dot nucleation begins first at site *A*, and then at site *B*. All dots begin with pyramidal shape that is followed by a transition to dome shape. The reason that dots form at sites *A* and *B* is interpreted as a result of the abundant supply of Ge adatoms due to the strain induced chemical potential gradient. Although no appropriate experiments have been done, it is expected that the time duration that the substrate temperature is sufficiently high is the determining factor for the preferential nucleation of dots at sites *A* and *B*. The longer the duration, the more Ge adatoms gather at these sites, and therefore high degrees of super-saturation.

Further increase of Ge coverage leads eventually to the nucleation of dots at site *C*. This occurs when Ge super-saturation reaches the critical value for dot nucleation. The combined knowledge of the Ge flux and the deposition time allows a rough estimate of the critical value of Ge super-saturation necessary for the nucleation of dots. The only uncertainty in such an estimate is the precise wetting layer thickness that cannot be determined by the absence of dots, but only by monitoring the adatom density in real time. Majority of the wetting layer quoted in the literature uses the former definition and is therefore strictly speaking inaccurate.

Immediately after the onset of dot nucleation at site C, directional diffusion takes place across the entire sample surface. At this point, all existing dots function as sinks for Ge adatoms. Figure 18 shows a schematic drawing of the Ge adatom density near dots at site C. Directional diffusion contribute to the decrease Ge adatom density between dots. The rate of decrease is inversely proportional to the inter-dot spacing. Depends on the relative magnitude of the incoming Ge flux to the directional diffusion rate, the Ge adatom density between dots may increase further, leading to more dot being nucleated that is associated with a decrease in the spacing between dots as well as an increase in Ge adatom loss due to directional diffusion. During this process, experimental observations show continued nucleation of dots that corresponds to Ge coverage from 4.5 to 6.0 Å in our experiments. Eventually, the spacing between dots becomes small enough so that the directional diffusion flux overtakes the incoming Ge flux and the Ge adatom density drops below the critical super-saturation value (n_c). Dot nucleation process comes to a halt.

Many researchers have reported the surface diffusion of heteroepitaxial growths because of practical demands as well as the interest in the understanding of surface processes. Formation of Ge dots on Si (001) depends strongly on surface diffusion of Ge adatoms [55, 56]. The simultaneous processes of surface diffusion of adatoms and SK mode island nucleation and growth have greatly complicated our ability to correctly interpret experimental results. The large number of modeling attempts using molecular-dynamic (MD) technique and *ab initio* total energy calculations have contributed to the understanding of adsorption and diffusion of Ge adatoms [57, 58]. Such theoretical studies suffer from the lacking of an appropriate potential for surface processes in the case of MD simulation, and the limited computation power of modern computer in the case of *ab initio* calculation. The rate

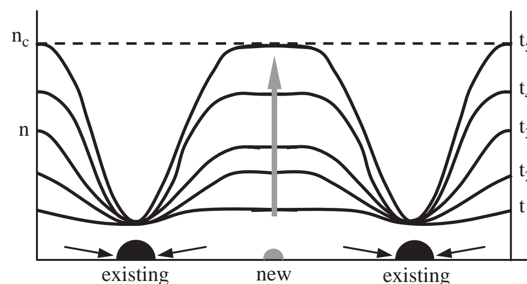

Figure 18. Schematic drawing of Ge adatom density between two existing Ge quantum dots at site C. When the distance between two dots is larger than the equilibrium inter-dot spacing, another nucleation occurs at the position Ge super-saturation reaches the critical value (n_c) with the increase of time (t_1 to t_5). Reprinted with permission from H. J. Kim et al.,"Three-Stage Nucleation and Growth of Ge Self-Assembled Quantum Dots Grown on Partially Relaxed SiGe Buffer Layers," *Phys. Rev. B* 68, 205312–205317 (2003). © 2003, American Physical Society.

equation approach has mathematically described the detailed nucleation and growth behavior [59, 60]. The correct values of the constants of the rate equation, however, could come only from experiments. Mo et al. observed anisotropic diffusion of Si adatoms on Si (001) using the denuded zone free of 2-D Si islands in the vicinity of surface steps [61]. They used extremely low Si coverage (0.07 ML) and derived the relationship between the island density, the denuded zone width, and the surface diffusion coefficient. Their result is not applicable to heteroepitaxy following SK mode since film growth is no longer via the attachment of adatoms to step edges as in the case of Frank-van der Merwe (layer-by-layer) growth mode. It can be stated that a clear understanding of the diffusion of adatoms is lacking, especially in the case of heteroepitaxy such as Ge dots on Si (001).

Now we discuss how the denuded zone width (W_{DZ}) and the inter-dot spacing (d_i) in the region far away from dislocations define the surface diffusion coefficient (D_s) and activation energy (E_s). As the growth temperature increases or the growth rate decreases, the surface diffusion length of Ge adatoms increases, resulting in both larger W_{DZ} and d_i. The activation energy of surface diffusion is obtained from Arrehenius plot of the areal dot density (N) in the region far away from dislocations as a function of the growth temperature. Figure 17 shows the schematic drawing of the adatom density (n_s) as a function of the growth time. It is generally accepted that the equilibrium saturated adatom density is much less than 1 ML [62]. The incorporation of Ge adatoms during the wetting layer growth is either via two-dimensional island nucleation or via step flow. The Ge adatom density is slightly above the equilibrium value in view of a combination of the abundance of surface steps as adatom sinks and the low incoming flux of Ge. Upon the completion of the wetting layer, Ge adatoms can no longer incorporate into the 2-D film due to the high strain energy in the film. The adatom density increases linearly with growth time until it reaches the super-saturation value for the nucleation of 3-D Ge dots. At the onset of Ge dots nucleation, Ge adatom density drops abruptly. The adatom density between dots initially nucleated increases again for another nucleation events. This process continues until the inter-dot spacing is reduced to such a value the incoming Ge flux equals to the surface diffusion flux in between dots. Based on the above postulations the mean surface diffusion length (d_s) of Ge adatoms can be expressed by,

$$ds = \sqrt{D_s \tau} = \sqrt{\frac{1}{N}} \tag{1}$$

where, τ is the mean lifetime of Ge adatom. Using Eq. (1) and Fig. 1

$$4Ds \frac{\Delta n_{s,\max}}{ad_s/2} \sim R \tag{2}$$

where, a is the hopping distance and R is the growth rate (cm^{-2} sec^{-1}). $\Delta n_{s,\max} = n_{s,\max} - n_v$, n_s and n_v are an adatom density and an equilibrium adatom density, respectively. Thus $n_{s,\max} \leq R(\tau_r - \tau_o)$, τ_o and τ_r are time of 2-D wetting layer completion and onset of 3-D island nucleation, respectively. Finally we have

$$N \propto \exp(2E_s/k_B T) \tag{3}$$

where, k_B is Boltzmann constant.

Since N is equal to $1/(d_i)^2$, the measurement of the average dot density at various substrate temperatures provides the activation energy (E_s) in Arrehenius plot. Assuming that the volume increase of dots over the buried dislocations is contributed by the incorporation of Ge adatoms impinging within the corresponding denuded zones, the volume changes of dots over dislocations are carefully measured. Fick's first law is used to obtain the pre-exponential factor base on the fact that there is an adatom concentration gradient.

Figure 19 shows AFM topographic images corresponding to 6.0 Å Ge coverage grown at growth temperatures ranging from 650 °C to 750 °C. Fig. 19(a)–(e) are samples with a growth rate of 0.05 Å/s, while (f)–(j) are samples with a higher growth rate of 0.1 Å/s. Dot-free denuded zone exists on both sides of buried dislocations along the two $\langle 110 \rangle$ directions.

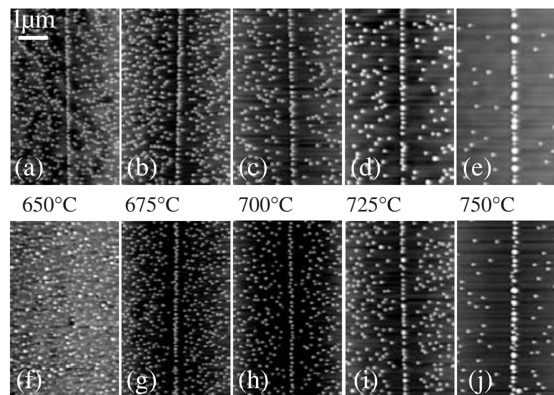

Figure 19. Two-dimensional AFM topographic images of 6.0 Å Ge coverage grown at five different growth temperatures on partially relaxed $Si_{0.9}Ge_{0.1}$ buffer layers in which buried dislocations provide the preferential nucleation sites. The growth rate of low-temperature Ge wetting-layer (3.4 Å) is 0.05 Å/sec. Subsequent 2.6 Å Ge are grown at 0.05 Å/sec for (a)–(e) and at 0.1 Å/sec for (f)–(j). Particularly, (e) and (f) show two extremes caused by high and low surface diffusion coefficients, respectively. Reprinted with permission from H. J. Kim et al., "A Technique for the Measurement of Surface Diffusion Coefficient and Activation Energy of Ge Adatom on Si(001)," *J. Appl. Phys.* 95(11), 6065–6071 (2004). © 2004, American Institute of Physics.

Furthermore, the denuded zone is wider as the growth temperature of Ge dots increases, indicating the increase of diffusion coefficient. It is important to note the necessity of using properly designed relaxed SiGe buffer layers with the dislocation spacing larger than the surface diffusion length of Ge adatoms. Failure to do so will lead to the absence of random dots, and with that, plenty of useful information [63]. Figure 19(f) shows no preferential nucleation of Ge dots over dislocations but the random nucleation of Ge dots in the region away from dislocations. The resulting quantum dot morphology reveals that the surface diffusion length of Ge adatoms is too short to be influenced by the chemical potential gradient over buried dislocations. Particularly, incident Ge flux is expected to be drastically higher than the diffusing Ge adatoms on the surface before the formation of dots. Super-saturation decreases abruptly with the nucleation of large number of dots. The average surface diffusion length is the longest for the sample of Fig. 19(e) grown at the highest growth temperature (750 °C) with the slowest growth rate (0.05 Å/sec). Therefore, more Ge adatoms incorporate into the region over buried dislocations and the probability of the nucleation of random dots decreases due to the lack of Ge adatoms. Eventually larger denuded zone widths form compared to the other samples grown at lower growth temperature or higher growth rate. The AFM images of Fig. 19(e) and (j) show the relatively non-uniform size distribution of dots grown over dislocations comparing to other samples. Coarsening (Ostwald ripening) is believed to cause the broader size distribution as well as the larger average size of dots at the expense of the decrease of dot density. The inter-dot spacing over dislocations is much smaller than that in the region between dislocations in all samples. Thus coarsening occurs in dots over dislocations at an earlier stage. Moreover, dots over dislocations in Fig. 19(e) show an additional event leading to the broad size distribution, i.e., coalescence among two or more dots. The perimeters of two adjacent dots overlap, leading to a two-hump configuration to be observed prior to becoming one bigger dot. The small spacing among dots over dislocations causes the rapid increase of average size. In contrast, coalescence is not observed in Fig. 19(j) that is grown at same growth temperature with a higher growth rate of 0.1 Å/sec. The density of random dots in the region far away from dislocations is strongly dependent of the surface diffusion of Ge adatoms. It decreases with the increase of growth temperature and the decrease of growth rate. Coarsening is manifested in this region as deviation from the linear relationship in Arrehenius plot of the dot density (N) as a function of the growth temperature. It will be discussed below.

From AFM images in Fig. 19, we further notice that denuded zone widths are symmetric with respect to the two perpendicular $\langle 110 \rangle$ directions. In other words, the anisotropic diffusion induced by the two types of terraces on a Si (001) surface [64] is not observed

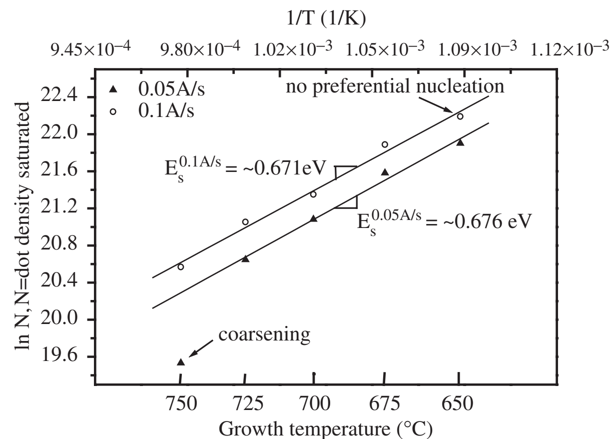

Figure 20. Arrehenius plots of the areal density of randomly nucleated dots in the region between dislocations versus the growth temperature. Reprinted with permission from H. J. Kim et al., "A Technique for the Measurement of Surface Diffusion Coefficient and Activation Energy of Ge Adatom on Si(001)," *J. Appl. Phys.* 95(11), 6065–6071 (2004). © 2004, American Institute of Physics.)

presumably due to the fact that the denuded zone widths are much larger than typical terrace widths and the anisotropy in diffusion is averaged out as a result.

Figure 20 shows Arrehenius plot of the areal density of random dots in the region away from dislocations as a function of the growth temperature between 650 °C and 750 °C. The areal dot densities are obtained from the saturated stage. The figure shows near perfect Arrehenius behavior with one exception. The only data point that deviates significantly is grown at 750 °C with the low growth rate of 0.05 Å/s. We believe the deviation is a result of the extremely long surface diffusion length of Ge adatoms on the surface leading to non-negligible coarsening. The apparent spacing between dots increases when smaller dots disappear as a direct consequence of coarsening. Based on the equation of $N \propto \exp(2E_s/k_BT)$, the activation energies obtained from two different growth rates of 0.05 Å/sec and 0.1 Å/secare 0.676 ± 0.03 eV and 0.671 ± 0.03 eV, respectively. Excluding the sample undergoing coarsening, similar activation energies are obtained from two growth rates. The experimental activation energies are comparable to the ones calculated in the literatures.

Now we obtain the pre-exponential factor from the volume increase of dots over dislocations as shown in Fig. 21. Additional two samples with 5.0 Å Ge coverage were grown at 700 °C with both growth rates of 0.05 Å/s and 0.1 Å/s, respectively. The average volumes of dots were carefully measured to compare with two other samples with 6.0 Å Ge coverage. At this growth temperature the dot size distributions are found to be relatively uniform at positions over buried dislocations and the region away from dislocations, respectively. Moreover, no coarsening effect is observed at two different Ge coverages. The average volume of dots over buried dislocation is apparently larger than that in the region away from dislocations. It is known that much more Ge adatoms are incorporated into the region over buried dislocations due to the chemical potential gradient. The volume increase of dots over dislocation is approximately proportional to the denuded zone width and larger than that of those in the region away from dislocations. We found that the total number of Ge atoms impinging onto the denuded zones is slightly larger than that for the average volume increase of dots over dislocations at both growth rates. This is an apparent evidence that the majority of Ge adatoms incident within the denuded zone incorporates into the existing dots over dislocations between 5.0 Å and 6.0 Å Ge coverage. Furthermore, the line density of dots over dislocations is identical at two Ge coverages with complete dome. This observation implies the absences of additional dot nucleation as well as pyramid-to-dome shape transition. Based on the simple assumption that there is a concentration gradient of Ge adatom in the denuded zones caused by the chemical potential gradient, surface diffusion coefficient

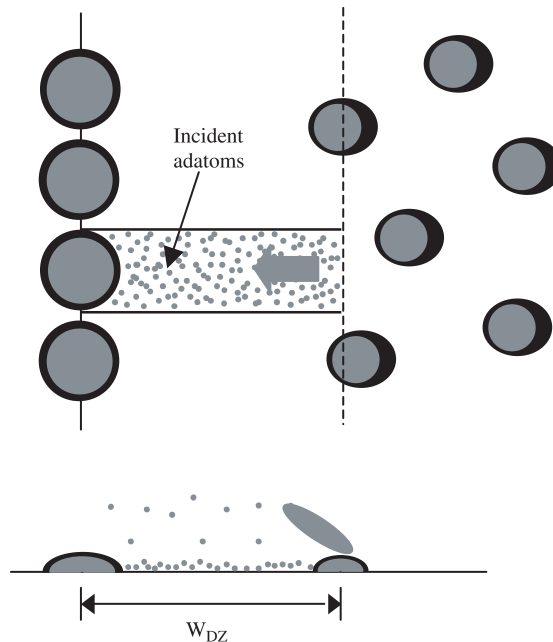

Figure 21. Schematic drawing showing preferentially nucleated quantum dots over a buried dislocation and randomly nucleated ones in the region far away from a dislocation. The increase of dot volume is equivalent to the number of adatoms incorporated from the denuded zone. Grey and black dots indicate the average sizes of 5.0 Å and 6.0 Å Ge coverages, respectively. Reprinted with permission from H. J. Kim et al., "A Technique for the Measurement of Surface Diffusion Coefficient and Activation Energy of Ge Adatom on Si(001)," *J. Appl. Phys.* 95(11), 6065–6071 (2004). © 2004, American Institute of Physics.

(D_s) is calculated using Fick's first law.

$$J = -D_s \frac{\Delta n}{\Delta x}$$

Flux J (atoms/sec) is given by the average volume increase of dots over dislocation between two different Ge coverages of 5.0 Å and 6.0 Å. The number of Ge atoms impinging directly onto the existing dots is negligible because the area of denuded zone on both sides is significantly larger than that of dots. $\Delta n / \Delta x$ (atoms/cm^2) is the number of Ge atoms arriving onto the unit area of denuded zone. In the samples grown with a growth rate of 0.05 Å/s, the volume measurement reveals that $\sim 7.1 \times 10^5$ atoms are used for the volume increase of an individual dot over buried dislocations for 20 seconds (2000 nm$^3 \approx 88,400$ Ge atoms). Based on the fact that 1.0 Å Ge coverage corresponds to $\sim 4.48 \times 10^{14}$ atoms/cm^2, it is found that $\sim 8.0 \times 10^5$ atoms arrive onto the square region in the denuded zone as shown in Fig. 21. As a result, $D_s = \sim 7.97 \times 10^{-11}$ cm^2/sec. Using the well-known equation of $D_s = D_o \exp(-E_s/kT)$ and the activation energy (0.676 eV), a pre-exponential factor (D_o) is $\sim 2.53 \times 10^{-7}$ cm^2/sec. At the higher growth rate of 0.1 Å/s much less number of Ge atoms ($\sim 1.1 \times 10^5$ atoms) incorporate for the volume increase presumably due to the smaller denuded zones. Consequently, the volume increase of dots over dislocations is considerably smaller compared to that of the sample with 0.05 Å/s. Using the activation energy (0.671 eV) obtained from the samples of 0.1 Å/s we obtain a slightly smaller pre-exponential factor ($\sim 1.0 \times 10^{-7}$ cm^2/ sec), implying a slower surface diffusion rate.

The incorporation of Ge adatoms during the wetting-layer growth is either via 2-D island nucleation or via step flow. The Ge adatom density is only slightly above the equilibrium value in view of a combination of the abundance of surface steps as adatom sinks and the low incoming flux of Ge. Upon the completion of the wetting layer ($t > \tau_o$), Ge adatoms can no longer incorporate into the 2-D film, presumably due to the high strain energy in the film. The critical adatom density for dot nucleation is first achieved in the regions near the intersections of dislocation lines and then above the dislocation lines themselves. These dots start

acting as adatom sinks, leading to strips of decreased adatom density near the dislocation lines. If the spacing between dislocations is larger than the adatom diffusion length, then the adatom density in the region away from the dislocations continues to increase approximately linearly with time, as shown for $\tau_o < t < \tau_r$ in Fig. 17, until it reaches the super-saturation value for the nucleation of 3-D Ge dots. At the onset of the Ge quantum dot nucleation, the density of Ge adatoms drops abruptly. The adatom density between the initially nucleated dots increases again with incoming Ge flux until another dot nucleates between two initially widely spaced dots. This process continues until the inter-dot spacing is reduced to a value for which the incoming Ge flux equals to the surface diffusion flux between dots. Qualitatively, the spatial distribution of dots and the existence of a denuded zone without dots near the dislocation lines can be traced back to the adatom density profile at times preceding the formation of randomly nucleated dots ($t < \tau_r$ in Fig. 17). The adatom density $n(x, y, t)$ obeys the Fick's diffusion equation

$$\frac{\partial n}{\partial t} = \nabla(D_s \nabla n) + F \tag{4}$$

where D_s is the surface diffusion coefficient and F is the deposition rate. Equation (4) can be used to describe the adatom density in a rectangular area $L_x \times L_y$ between the dislocations. We consider the time period when dots have already nucleated both on the intersections and dislocation lines, i.e., along the edges of this rectangular region. dots will grow by incorporating adatoms from the surrounding areas, in other words, dots over the dislocation lines act as adatom sinks, which can be modeled in the framework of Eq. (4) by the following boundary conditions:

$$n|_{x=0} = n|_{x=L_x} = n|_{y=0} = n|_{y=L_y} = n_v \tag{5}$$

where n_v is the equilibrium adatom density. To keep things simple, we assume that n_v is not affected by the strain due to the dislocation and growing dots. Furthermore, we neglect possible spatial variation of the diffusion constant D_s in the strained regions. Finally, we set the initial density at $t = 0$ as uniform, $n = n_v$. These assumptions are justified if, as in our case, one's aim is to arrive at qualitative conclusions regarding the time evolution of the density profile. Our methods for obtaining quantitative estimates of D_s, described below, do not rely on these approximations. Equation (4) can be solved analytically using Fourier series expansion in spatial coordinates. The calculated density profile $n(\tau, t)$ is shown in Fig. 22 at consecutive times. The critical density for nucleating dots is shown schematically as a dashed line. It is seen that the adatom density increases linearly in time over an extended region between the dislocation lines, where $n(\tau, t)$ stays practically flat. At a certain time, the critical density is reached simultaneously everywhere in this central region, leading to a sudden appearance of randomly nucleated dots and growth. In contrast, near the dislocation

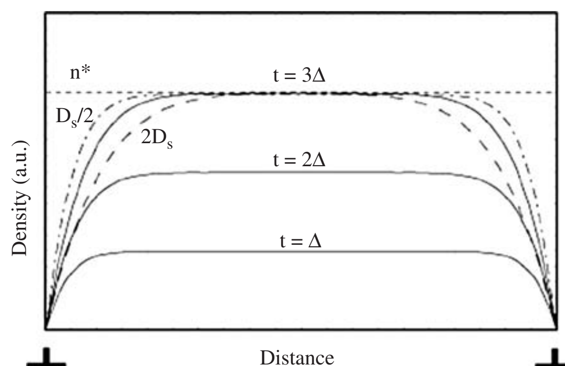

Figure 22. The simulation result of Ge adatom density profile in the region between two dislocations. Reprinted with permission from H. J. Kim et al., "A Technique for the Measurement of Surface Diffusion Coefficient and Activation Energy of Ge Adatom on Si(001)," *J. Appl. Phys.* 95(11), 6065–6071 (2004). © 2004, American Institute of Physics.

lines the density remains below the critical value, leading to the formation of denuded zones. The width of these zones depends on the ratio D_s/F, and increases with D_s/F if $n*$ is unchanged. Increase in growth temperature should increase both $n*$ and D_s, but the effect of increase in D_s should dominate and lead to a widening of the denuded zone.

This approach represents a new method to obtain the surface diffusion coefficient of heteroepitaxial growth. The behavior of Ge dots grown on the relaxed SiGe buffer layer is considerably dependent on the surface diffusion of Ge adatoms. All experimental observations are based on the fact that the denuded zone width and the inter-dot spacing of random dots are strongly dominated by the surface diffusion process. Two different values carefully measured at different growth temperatures and growth rates provide insight into surface diffusion process and the subsequent formation of Ge dots on Si substrate.

Alternative approaches for measuring the surface diffusion coefficient have used elaborate equipments consisting both of evaporation sources and *in-situ* surface analytical tools such as scanning Auger microscopy or ion scattering. In contrast, the new approach has practically employed 3-D Ge dots formation on Si surface following SK mode. Surface diffusion process in heteroepitaxial growth has been characterized by AFM observations of the morphology changes as functions of growth temperature and rate. Moreover, the buried dislocation network used in this study is the excellent tool to investigate the surface diffusion of adatoms. The approach is not limited to Si/Ge system but can be used for other heteroepitaxial systems in SK growth mode and in the presence of surfactants such as Sb, As, H, or C.

It is worth investigating the effect of surfactants because they have been frequently used for surfactant mediated epitaxial growth. It has been well established that the presence of surfactants has a significant effect on heteroepitaxial film morphology [65–69]. Surfactant refers to elements that do not incorporate into the film matrix, i.e., elements that have large surface segregation coefficients. In the case of Ge growth on Si, Sb is commonly employed as surfactant. The surface segregation coefficient of Sb in Ge is $> 10^4$ when the substrate temperature is above 500 °C [70, 71]. If a fraction of a monolayer of Sb is deposited at the beginning of the growth, the surface coverage stays approximately constant at the end of the film growth of moderate film thickness, e.g., 10 nm.

The actual function of surfactants remains somewhat controversial. Most of the experimental observations can be explained by reduced surface mobility of adatoms. Take Ge growth on Si as an example, the presence of Sb with a fraction of monolayer coverage significantly reduces the Ge adatom diffusivity. The quenched surface migration of Ge adatoms kinetically limits the surface from approaching the equilibrium configuration, which means the formation of Ge islands. Consequently, the surface stays flat as if the growth was carried out at much lower surface temperature than it actually is. Because elastic relaxation of misfit strain is not possible in a flat film, plastic relaxation via dislocation becomes the preferred mechanism for relieving the misfit strain when the critical film thickness is exceeded. This was observed by Thornton et al. in the early 1990s [6]. The model of reduced adatom diffusivity is also consistent with the experimental observations of Peng et al. [8] showing that the presence of Sb results in significantly increased Ge dot density. Two factors could be responsible for the seemingly controversial observations of Thornton et al. and Peng et al., substrate temperature (T_{sub}) and the surface coverage of Sb. It is intuitively obvious that either raising (T_{sub}) or reducing Sb coverage should result in surface morphology that is less limited by kinetics, i.e., the development of Ge islands. Since the density of Ge islands is determined by the diffusion length of Ge adatoms as shown above, it is natural that a somewhat reduced diffusion length renders higher Ge island density. Finally, it has been observed by Katayama et al. [7] that the use of Sb as surfactant during growth also reduces the intermixing between Ge and Si. This observation can again be explained by the reduced diffusion of adatoms. When less than a monolayer of Ge is grown on Si substrate at elevated temperatures, the surface adatom population is composed of both Ge and Si. The concentration of Si decreases with increasing Ge film thickness. Intuition tells us that reducing the adatom mobility should result in a more abrupt interface, i.e., less intermixing. This becomes more obvious by considering the hypothetical case of zero mobility. Incident atoms stay exactly

where they landed. It is obvious that in this case the interface is as sharp as the flatness of the original Si substrate surface.

There is no doubt that Sb surfactant also alters the surface energy of a growing film. The question is whether the change in surface energy or in adatom mobility is the dominant factor that determines the prevailing surface morphology. Most of the experimental evidence in the literature appears to support the scenario that the main function of Sb in Ge growth on Si is impeding the surface kinetics. It is worth pointing out that it is not necessarily true that a species that segregates on the surface always impedes adatom diffusion. Alternatively stated, the function of surfactants is in general materials system dependent.

5. InAs QUANTUM DOTS ON GaAs

InAs quantum dots grown on GaAs substrates are especially interesting due to type-I band alignment in which both electrons and holes are confined in quantum dots, making them suitable candidates for optoelectronic devices such as LEDs and lasers. Successful demonstration of InAs quantum dot lasers and photo-detectors are good examples [72, 73]. Nearly all these quantum dots are fabricated by epitaxy via self-assembled Stranski-Krastanow growth.

For epitaxy of quantum dots, it is very important to control dot density, size and uniformity, by controlling growth kinetics, such as nucleation, surface diffusion and coarsening. For epitaxy of self-assembled InAs quantum dots, specific growth parameters that can affect growth are As beam equivalent pressure, In flux, and growth temperature. The difference in growth conditions causes difference in both structure and optical properties of dot assemble. And this is the subject of many publications. Here the progress of both experimental and theoretical work that probed the InAs on GaAs self-assembled quantum dots via epitaxy is reviewed.

5.1. Growth Parameters that Strongly Affect Dot Formation

By modifying growth parameters that strongly influence the formation of InAs dots on GaAs, quantum dot shape, density and uniformity can be changed to satisfy the specific requirement [74, 75]. Quantum dot density and uniformity in both shape and size is important for optoelelectronic applications. Quantum dot density is strongly affected by surface nucleation processes. Surface nucleation has been well studied in both experimental and theoretical aspects [76–80]. However, uniformity of quantum dots is still a subject that needs more study to be understood. There is no well-established model that can explain the main features of quantum dot uniformity. Therefore, here the nucleation model is only reviewed.

Surface diffusion, which is a function of substrate temperature, strongly affects the quantum dot nucleation and later growth. Surface diffusion can be described as random walk (as shown in Fig. 23)

$$D_{\text{adatom}} = f n_c \lambda^2 \nu_0 \exp\left(\frac{\Delta S}{k}\right) \exp\left(-\frac{\Delta H}{kT}\right) = D_s \exp\left(-\frac{E_a}{kT}\right) \tag{6}$$

where f is correlation factor, n_c is the nearest neighbor sites where adatom can jump, λ is jumping step which is on the order of lattice constant, ν_0 is trial frequency for adatom jumping on the surface, ΔS is entropy change, ΔH is the enthalpy change, k is the Boltzman constant, T is substrate temperature in degree Kelvin. All of the temperature independent constant can be simplified in D_s, the ΔH will be the activation energy that is often used. Surface nucleation can be characterized by dot density n_{dot} or characteristics distance l between dots or islands. l has power law dependence on diffusion and incoming flux F for deposition [81]

$$l \sim \left(\frac{D_{\text{adatom}}}{F}\right)^{\gamma} \tag{7}$$

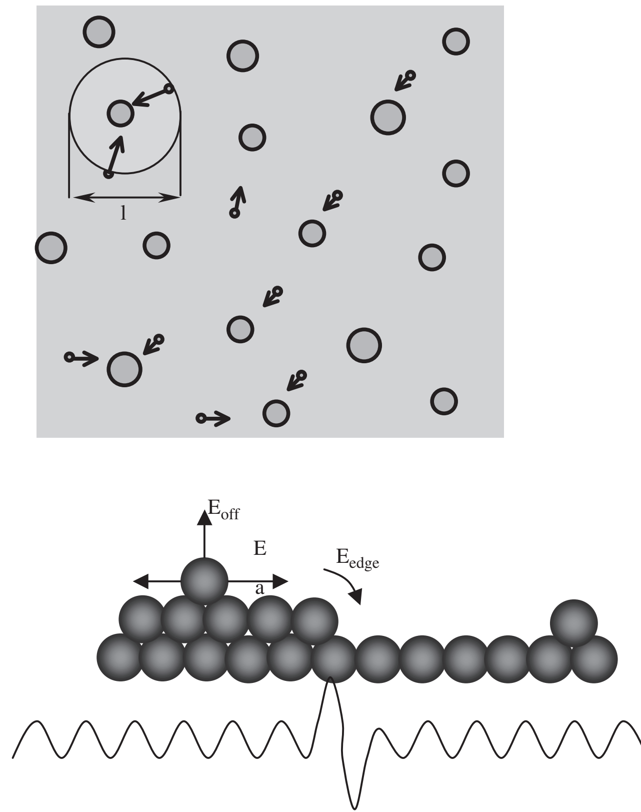

Figure 23. Schematic picture for surface diffusion.

where γ is characteristic constant for system, which is related to critical size for stable cluster on the surface. The dot density will be

$$n_{dot} \sim l^{-2} \sim \left(\frac{D_{\text{adatom}}}{F}\right)^{-2\gamma} = D_0^{-2\gamma} F^{2\gamma} e^{\frac{2\gamma E_a}{kT}} \tag{8}$$

Theoretical analysis shows [82]

$$\gamma = \frac{i^*}{2i^* + 2 + d_f} \tag{9}$$

here i^* is the critical cluster size, d_f is the fractal dimension for nucleation. Figure 24 shows the value of γ dependence on i^* for two dimension nucleation. Increasing critical cluster size, γ is saturated to 0.5. Although this model is based on two-dimension growth, it still can give good agreement to three-dimension growth. This is because three-dimension growth begins from two-dimension nucleation. From Eq. (8), it is very clear that decreasing substrate temperature or increasing growth rate can increase dot density. For InAs quantum dots growth on GaAs substrate, As BEP is another parameter that affects the dot nucleation. However, the mechanism is not well understood. Experimental results and current understanding of effects from growth parameters, such as substrate temperature, growth rate, and As BEP, are discussed in the following.

5.1.1. Substrate Temperature

InAs dots growth within the substrate temperature range of 420 to 500 °C shows a clear dot density dependence on substrate temperature [83]. The dependence is nearly linear in Arrhenius plot except at very low temperature indicating the existence of a single activation energy. There is also a somewhat counter-intuitive trend of improved dot size uniformity at high substrate temperature. Shiramine et al. studied InAs adatom migration on GaAs (001) using the dot density dependence on growth temperature [84]. The adatom migration

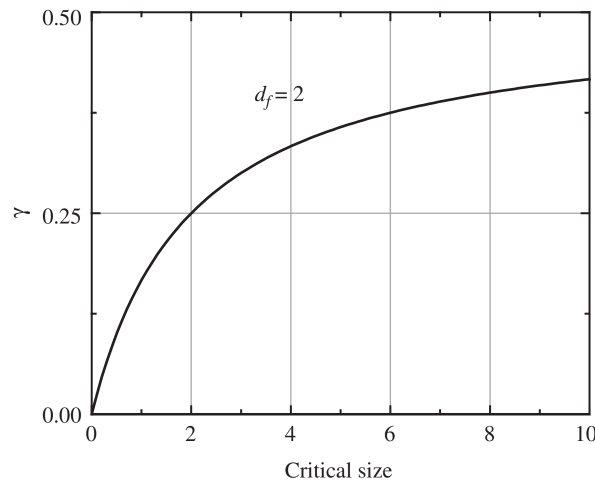

Figure 24. Dependence of power constant for nucleation on critical size.

activation energy is obtained from the associated Arrhenius plot. The activation energy obtained in this fashion is completely dependent on the choice of γ. For the critical nucleus size of 2 atoms as commonly assumed by the community, we have $\gamma = 0.25$ that leads to an activation energy value of 4.0 eV. This value is the same as In desorption activation energy for InAs homoepitaxy [85] and therefore is unreasonable for surface migration. This observation provides an indirect evidence of the critical nucleus size is substantially larger than 2 atoms. For a hypothetical critical size of 10 atoms, the activation energy becomes $\sim$2 eV. The main point is that the nucleation model is consistent with the main features of InAs quantum dots growth under various substrate temperatures. InAs dots with high density can be obtained by epitaxial growths at lower temperature, although high temperature leads to low density but better uniformity.

5.1.2. Growth Rate

As shown in Eq. (8), increasing growth rate can increase dot density. Joyce et al. report InAs QDs grown at 490 °C with different growth rates which were changed from 0.55 to 0.0065 ML/s. STM results show a significant decrease of dot density with decreasing growth rates [86]. When growth rate was vaired from 0.094 ML/s to 0.016 ML/s, the dot density was changed from 1×10^{11} to 0.2×10^{11} cm^{-2} and the dot size deceased accordingly as shown in Fig. 25. Nakata et al. conducted a more detailed investigation on growth rate effect [87]. The dot density decreases linearly with decreasing growth rate from 1×10^{-1} to 2×10^{-3} ML/s at the substrate temperature of 510 °C as shown in Fig. 26. According to Eq. (8), it means that the power of γ is near to 0.5. From Fig. 24, we can conclude that the critical cluster

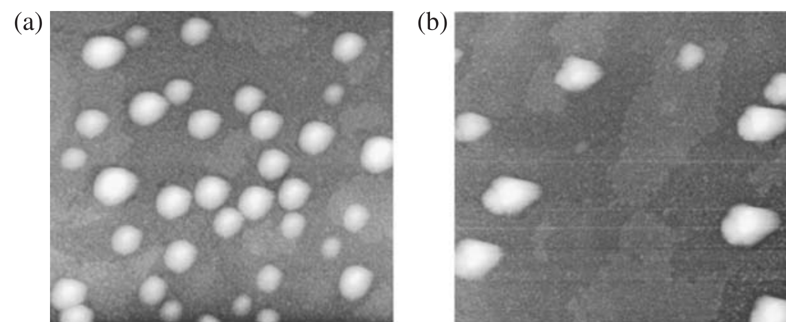

Figure 25. STM images (0.2×0.2 μm^2) of 2.2 ML of InAs deposited on GaAs(001) at 490 °C with rates of (a) 0.094 ML/s and (b) 0.016 ML/s. Reprinted with permission from [86], P. B. Joyce et al., "Effect of Growth Rate on the Size, Composition, and Optical Properties of InAs'GaAs Quantum Dots Grown by Molecular-Beam Epitaxy," *Phys. Rev. B* 62(16), 10891–10895 (2000). © 2000, The American Physical Society.

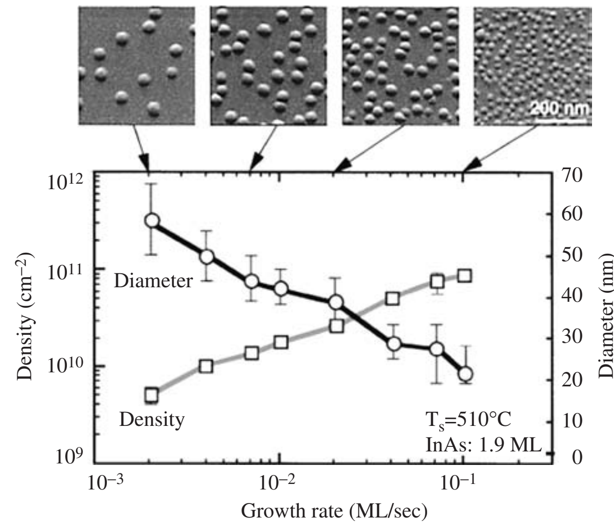

Figure 26. Base diameter and density of the islands measured by AFM as a function of growth rate, together with AFM images ($0.5 \times 0.5\ \mu m^2$). Reprinted with permission [87], Y. Nakata et al., "Molecular Beam Epitaxial Growth of InAs Self-Assembled Quantum Dots with Light-Emission at 1.3 μm," *J. Cryst. Growth* 208, 93–99 (2000). © 2000, Elsevier Science B.V.

size for InAs nucleation on GaAs is pretty large (much more than 3 atoms). Later reported results confirm the trend of dot density dependence on growth rate [88]. These experimental observations are consistent with the dot density being determined by surface migration of adatoms and show that growth rate is another parameter that can be modified to control dot density.

5.1.3. As Beam Equivalent Pressure (BEP)

As BEP is another factor that affects the InAs dot formation. This factor makes InAs dot growth on GaAs more complex than Ge dots growth Si. Madhukar et al. investigate the As_4 dependence of dot formation as Fig. 27 shown [89]. At low temperature of 420 °C, the dot density increases with decreasing As_4 BEP. The authors suggest that this is related to As_4 dissociative reaction. At low temperature, As_4 dissociative reaction rates are relatively slow,

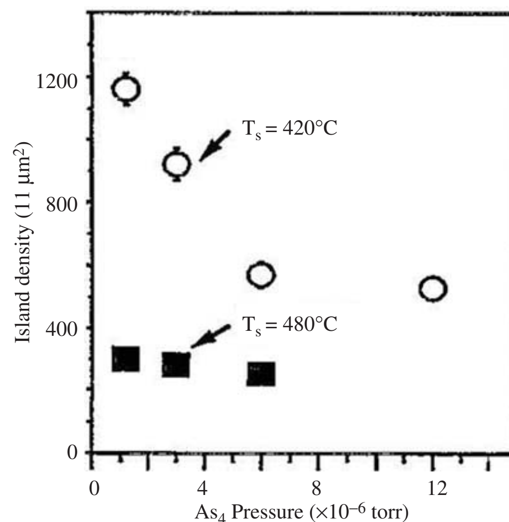

Figure 27. Variation of the density of InAs islands grown on GaAs (001) as a function of the As_4 pressure for substrate temperature of 480 and 420 °C. Reprinted with permission from [89], A. Madhukar et al., "Nature of Strained InAs Three-Dimensional Island Formation and Distribution on GaAs(100)," *Appl. Phys. Lett.* 64(20), 2727–2729 (1994). © 1994, American Institute of Physics.

as a result, In incorporation to dots can be enhanced by increasing As_4 BEP. Efficient In incorporation into existing dots leads to lower density of In adatoms making dot nucleation less probable. The consequence is low dot density at high As BEP. At temperatures higher than 480 °C, As_4 dissociative reaction is no longer the limited process resulting in the dot density being nearly independent on As_4 BEP [90]. Later study at 500 °C confirms the near independence of dot density from As_4 BEP. And the dot density only decreases a little. Yamaguchi et al. observed a slight decrease in dot density at high temperature under very low As_4 BEP ($<5 \times 10^{-7}$ torr) and attributed this to diffusion enhancement at low As BEP. However, there is also a drop in dot density at very high As_4 BEP ($>1.7 \times 10^{-6}$ torr), which is still not well understood [91]. Experiments of Solomon et al. show that maintaining the growth rate and increasing As_2 BEP result in decreasing dot density. The reason is not clearly explained. Clearly, more studying is necessary to understand the role of As BEP in the InAs dots formation on GaAs substrates.

5.1.4. Dot Size and Shape

The energy levels in quantum dots are determined by quantum dot shape and size, which are most commonly characterized using TEM and STM. Reflection high-energy electron diffraction (RHEED) is one of the important tool for monitoring dot shape evolution during epitaxy growths [96]. InAs dots on GaAs mostly show pyramid shape. Atomic structure of InAs quantum dots on GaAs was reviewd by Jacobi et al. STM results show {137} facets for InAs on GaAs (001) as Fig 28. The atom unit cell on the facets was distinguished by STM [97]. Other groups report that there are other facets observed. It is reported that {113} facet appears in MBE growth [98, 99]. Costantini et al. reported the observation of {110} and {111} facets from samples grown at 0.008 ML/s, 1.8 ML InAs at 500 °C (Fig. 29) [100]. This agrees with ab initio calculations for equilibrium shapes of InAs dots on GaAs (001) [101]. Experimental results from Saito et al. show that dots are in pyramidal shape with {136} facets at low temperature (440–500 °C), and change into multifaceted shape with the lower portion surrounded by {110} facets and the upper portion surrounded by {136} facets at high temperature (510–550°*C*). The dots with {302} facets were also observed after 1.74 ML of InAs growth at 500 °C [102]. Mukhametzhanov et al. [103] suggest that there exists a maximum lateral size for InAs dots (~24 nm with 500 °C and 0.22 ML/s) based mainly on the consideration of the build up of elastic strain energy in the substrate and dot combined. Further addition of material goes primarily towards raising the island heights. This means the dot facets evolve from low angle facets to high angle facets.

TEM is another method to characterize the shape of dots. Plan-view TEM done by Grundamnn et al. shows a very clear pyramidal shape [104]. Careful X-TEM [105] shows that InAs dots on GaAs have square base and they are locally arranged in a two dimensional square lattice with main axes along ⟨100⟩ crystallographic directions.

Figure 28. Left-hand side: STM image of a InAs quantum dot on GaAs(0 0 1). Right-hand side: Model derived from the STM data. Reprinted with permission from [97], K. Jacobi, "Atomic Structure of InAs Quantum Dots on GaAs," *Prog. Surf. Sci.* 71, 185–215 (2003). © 2003, Elsevier Science Ltd.

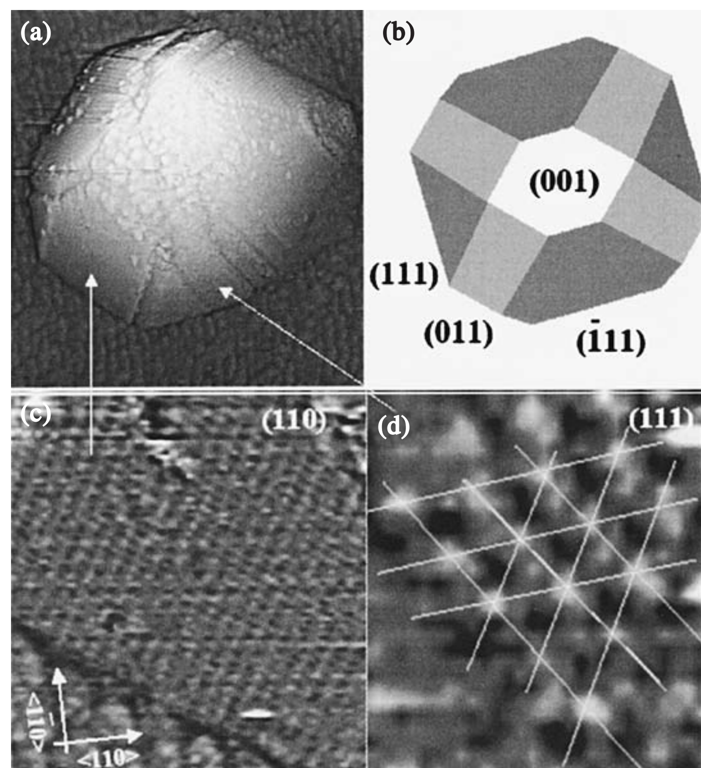

Figure 29. (a) 50×50-nm^2 STM topography of a large island. (b) Equilibrium shape of an InAs island. High-resolution views of (c) the (110) facet (12×12 mm^2) and (d) the (111) facet (4×4 nm^2) of the same island. Lines showing the (2×2) reconstruction have been superimposed in (d). Reprinted with permission from [100], G. Costantini et al., "InAs/GaAs(001) Quantum Dots Close to Thermodynamic Equilibrium," *Appl. Phys. Lett.* 82(19), 3194–3146 (2003). © 2003, American Institute of Physics.

From these various facets reported under different growth conditions, we can conclude that facet formation is kinetic limited. Under low growth rate and high temperature, adatoms are energetic enough to approach the more energy favorable configuration with low index facets as expected by theoretical calculation. At low temperature or high growth rate, other less stable facets start to be observed.

5.2. Optical Properties for Optoelectronic Applications

Optoelectronic application makes the study of optical properties for InAs quantum dots important. One of the unique properties for a single quantum dot is its atom-like energy levels. Carriers are confined in three dimensions, quantum dots can be referred to as zero-dimensional systems. Here studies for InAs quantum dots optical properties related with their special energy structures are discussed. Works for particular applications, such as 1.3 μm emission, is also covered.

InAs quantum dots on GaAs substrates have type-I band lineup which was confirmed by XPS [116]. This allows for the simultaneous confinement of both electrons and holes. The energy bands change to atomic-like discrete energy levels and density of state in quantum dots is δ-function like. Grundmann et al. report ultra narrow luminescence lines from single quantum dots [117]. The high-resolution cathodoluminescence gives very sharp peaks from single quantum dots. The FWHM is below 0.15 meV. This result confirms the atomic-like density-of-state in quantum dots. Later studies by near-field scanning optical microscopy showed more detailed quantized energy levels [118]. The true FWHM is below 0.25 meV.

5.2.1. Luminescences from InAs Quantum Dots

Photoluminescence (PL) from quantum dots is studied by many groups. Due to the difference in shape and size distribution, the PL peak position and shape are always different.

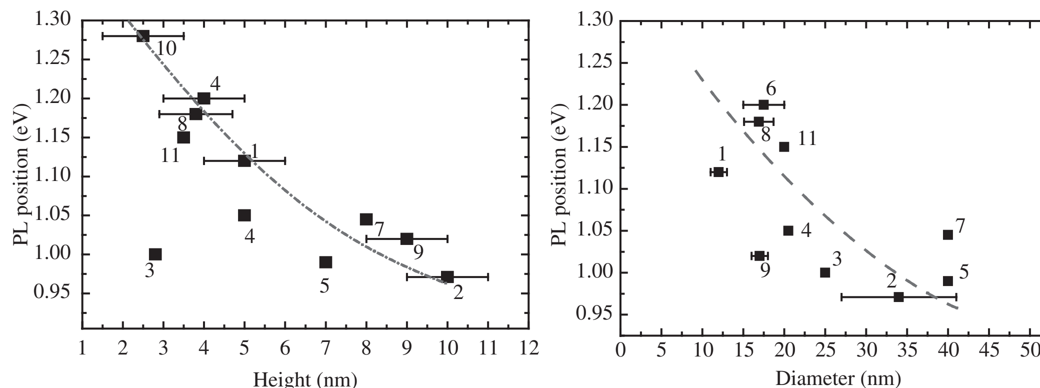

Figure 30. PLs from different groups with different size. 1: M. Grundmann et al., *Phys. Rev. Lett.* 74, 4043 (1995), 2: Garcia et al., *Appl. Phys. Lett.* 71, 2014 (1997), 3: Choi et al., 4th Internatinal Workshop SQSand Np, 4: Kim et al., *J. Appl. Phys.* 94, 6603 (2003), 5: Choi et al., 4th Internatinal Workshop SQSand Np, 6: Sugawara et al., *Semiconductor and Semimetals*, V60, 7: Yamaguchi et al., *Jpn. J. Appl. Phys.* 39, 1245 (2000), 8: Mukhametzhanov et al., *Appl. Phys. Lett.* 73, 1841 (1998), 9: Ferdos et al., *J. Cryst. Growth* 227–228, 1140 (2001), 10: Ours, 11: Joyce et al., *Phys. Rev. B* 62, 10891 (2000).

The difference in shape and size distribution of InAs dots is mainly caused by difference in growth method and conditions. Grundmann et al. report the PL around 1.32 eV for 0.6 nm thick InAs and 1.10 eV for 1.2 nm thick InAs grown at 450 °C [122]. Leonard et al. reported PL at 1.27 eV for 2 ML InAs grown at 530 °C. Figure 30 compares the PL energy reported by different groups. Although the data are scattered in a very large range, there is still a clear trend that energy shifts toward low energy with increasing dot diameter or height as expected by quantum mechanics.

According the quantum confinement of quantum dots, the energy levels are shifted with quantum dot size. The three different confinement regions, weak confinement, strong confinement and medial confinement, have been reviewed by Yoffe [123]. Theoretical calculation can render reasonably satisfactory results using simple effective mass approximation for weak confinement with dot radius $R \gg a_b$ exciton Bohr radius as well as for strong confinement with $R \ll a_b$. For InAs quantum dots on GaAs, the dot size R is approximately equal to a_b, $R < a_e$ (35 nm) electron Bohr radius and $R > a_h$ (2 nm) hole Bohr radius, the simple approximation cannot give a quantitative agreement with experiments results. Theoretical calculation considering strain and shape of quantum dots can be compared with experimental results [124, 125].

In order to get PL, capping layers have to be deposited to reduce surface recombination. The effect of capping on PL was studied by García et al. [126]. Quantum dots capped with 5 nm or more GaAs give a strong luminescence intensity. Analysis of the AFM profiles shows that a large anisotropic redistribution of the island material is taking place during the initial GaAs overgrowth. For small GaAs coverages (below 5 nm), atomic force microscopy (AFM) images show partially covered island structures with a regular size distribution which is elongated in the [011] direction. In addition, based on the redshifted PL spectrum of the annealed sample together with the AFM measured reduction of 30% in height of the partially covered islands, García et al. suggest an enhanced In intermixing in the vicinities of the quantum dots. Therefore, the GaAs capping after InAs growth is mostly done immediately at low temperature then raising the temperature for later growth.

Besides capping processes, growth conditions for dots also affect both PL position and intensity from InAs quantum dots [127]. First is the InAs coverage. Alessi et al. report a common trend for PL position dependence on growth coverages, there are three regions clearly distinguished in different InAs coverages as Fig. 31 shown [128]. In region I ($L \leq 1.5$ ML), the recombination energies Ep depend linearly on L, with a slope of the order 40 meV/ML. In region II ($1.5 \leq L \leq 2$ ML), which is around the critical thickness, Ep decreases much faster with increasing L (about 0.6 eV/ML) than in region I. With selecting excitation and detection conditions, the PL spectra of the samples in region II often give rich structures and the spectral weight shifts from higher to lower energy with increasing coverage. In region III

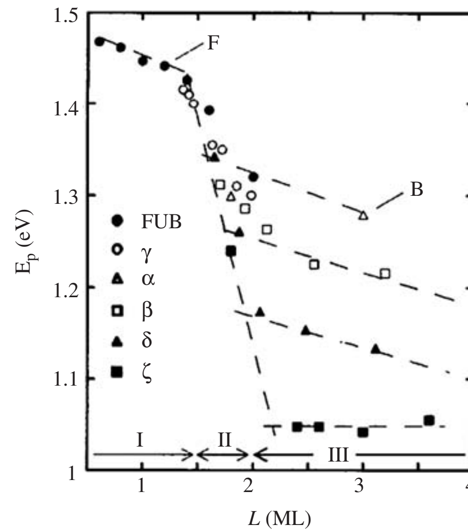

Figure 31. For PL trend: Peak emission energies vs L of the main bands observed in the present work in the PL spectra of samples grown by MBE or ALMBE under various conditions. Dashed lines are guides to the eye and define three different regions in the plane. Cross-sectional HRTEM micrographs have been obtained for samples labeled by capital letters. FUB = consist of a single InAs quantum well with $0.6<L<2$ ML, grown at 420 °C by MBE. α, β = consist of quantum dot's deposited at 500 °C and GaAs cap layers grown at 350 °C for 5 ML and then at 600 °C by MBE. γ = consist of quantum dot's and GaAs cap layer deposited entirely at 500 °C by MBE. δ = consist of quantum dot's and GaAs cap layer deposited entirely at 520 °C by MBE. ζ = consist of quantum dot's and caps grown at 460 °C and at 360 °C, respectively by ALMBE. Reprinted with permission from [128], M. Grassi Alessi et al., "Optical Properties of InAs Quantum Dots: Common Trends," *Phys. Rev. B* 59(11), 7620–7623 (1999). © 1999, The American Physical Society.

($L \geq 2$ ML), the rate of change for Ep with Lbecomes slow again. The slope is similar to that observed for $L \leq 1.5$ ML. And each series of samples saturate to certain emission energy with further increasing coverage. The only exception is the ALMBE samples whose emission energy is the lowest among all investigated samples and is independent of deposited InAs coverage. The peak shape also changes with coverage. With increasing coverage, the high order peak becomes clear and FWHM of ground state decreases [129–131].

Growth temperature and As BEP are another two factors that can affect dot size and shape, thus causing PL difference [132]. InAs quantum dots grown with higher substrate temperature or lower As BEP show a higher intensity and smaller FWHM compared to quantum dots grown with lower substrate temperature or higher As BEP. Chu et al. suggest that this is related with crystal quality [133, 134].

Different quantum dot assembles grown with different growth parameters have different carrier dynamics. This can affect the applications of quantum dots. Therefore, carrier dynamic properties are investigated. Carrier dynamic information can be obtained from PL with different temperature and excitation density. The temperature and excitation power dependence of InAs quantum dots emission is different from bulk materials [135]. Figure 32 schematically shows the carrier relaxation in InAs quantum dots on GaAs. For excitation energy higher than GaAs band gap, which is mostly used for PL, such as Ar ion laser with energy around 2.41 eV for 514.5 nm and 2.54 eV for 488 nm, a large portion of carrier will be generated in GaAs layer. The carrier relaxation from GaAs to quantum dots include many processes that determine optical properties of quantum dots. The processes happened in GaAs include carrier generation, carrier relaxation to wetting-layer, carrier recombination and carrier escaping from wetting-layer to GaAs. The characteristic times are $\tau_{cw} \leq 10$ ps for carrier relaxation to wetting layer, $\tau_g \sim 100$–1000 ps for carrier recombination depended on material quality, and the escape time from wetting layer to GaAs barrier $\tau_{ew} \ll \tau_{cw}$ at low temperature [136, 137]. The carrier escape time is strongly dependence on temperature ($\sim \exp(E_a/kT)$). The processes in wetting-layer are recombination, relaxation to quantum dots and escaping to GaAs and from quantum dots. The recombination time in wetting-layer τ_w is around 200–400 ps [138, 139]. The relaxation time from wetting-layer to quantum dots

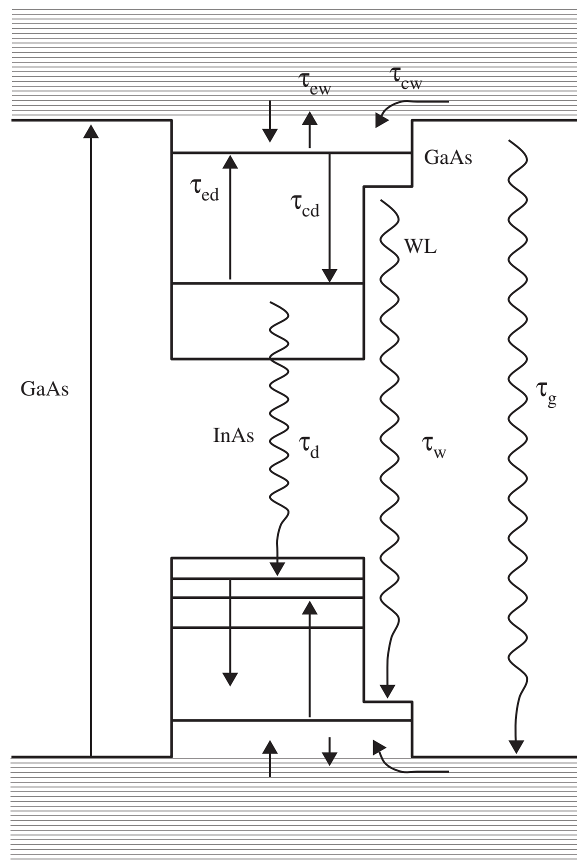

Figure 32. Carrier relaxation processes happened in InAs quantum dots embedded in GaAs.

is $\tau_{cd} < 10$ ps. The escaping from quantum dots is similar as escaping from wetting-layer to GaAs, which is strongly dependent on temperature. At low temperature (<100 K), it is negligible. But when the temperature increases, it becomes very important. And carrier escaping can quench the PL when the temperature is high enough. The processes in quantum dots are carrier recombination and carrier escaping. The carrier recombination time is 400–2000 ps depending on growth conditions. For carriers generated by high-energy excitation, they relax from GaAs barrier layers through a ladderlike process [140, 141]. Specifically, electron transfer from GaAs barrier to InAs wetting layer and then relax to ground state and finally recombine at ground state; hole transfer firstly from GaAs barrier to highest excited state, then it relax to second highest excited state, thus step by step, at the end it recombines at ground state. Additionally, the carrier relax in a single dots by multiphonon-assistance due to the large energy gap cause by quantum confinement in such small dots (less than 10 nm in height) [142–144]. In all of these processes, carrier relaxation has to compete with nonradiative recombination centers caused by defects. The excited-state emission only appears at high excitation density due to the saturation of ground state. At low temperature, integrated PL properties show constant intensity and FHWM below 100 K [145, 146]. At high temperature, carrier escape from dots to GaAs becomes important. The PL is quenched at certain temperature [147].

From the widely scattered data from many groups, it is very clear that carrier relaxation in InAs quantum dots is strongly dependent on the sample structure. The growth methods and condition variation causes the different dot size, size distribution and density. The widely expected phonon bottleneck effect, an intrinsic slow carrier relaxation from exciation states to ground state [148], is a solid evidence of the difference between different dot structures. Adler et al. claim the existence of phonon bottleneck in InAs quantum dots grown by MOCVD [149]. The effect of phonon bottleneck is absent in structures with laterally and/or vertically coupled InAs quantum dots with GaAs barriers presumably due to the availability

of alternative relaxation pathways [150,151]. Therefore, it is possible to modify growth procedures and quantum dot structures to get the properties that is conducive to applications and avert the effects that is unfavorable to devices.

5.2.2. Stacked Structures for Device Application

Stacked muti-layer quantum dots are often preferred in device application. If the GaAs spacer layer thickness is controlled to certain value, InAs quantum dots align along the vertical direction. In stacked structures, due to increasing of gain medium volume, gain saturation can be extended. Carrier relaxation processes in stacked quantum dot structures are investigated by Heitz et al. [182]. The experimental results show that the dot shape and size uniformity are both improved with increasing number of stacked InAs quantum dot layers. A clear redshift and FWHM narrowing are observed with increasing stacked layers. This feature is attributed to the vertical coupling of quantum dots. Other studies confirm this property in InAs quantum dots [183]. Another effect of stacked structure is the absence of phonon bottleneck when GaAs barrier layer is thin enough to cause coupling vertically between aligned dots. Quantum dot lasers using stacked structure are also demonstrated [184]. The effects of stacking on gain and threshold of InAs quantum dot lasers on GaAs substrates are discussed both experimentally and theoretically [185, 186]. The stacked quantum dot structure have a high gain and low threshold current for laser applications.

5.2.3. Works for 1.3 μm Emission

As Fig. 31 shown, the wavelength of light emission from InAs quantum dots on GaAs substrates are mostly short than 1.2 μm. Currently, the long-wave length fiber communications are using silica-based optical fibers. There is a zero-dispersion at 1.3 μm. Application in optical communications require the laser wavelength to be in the range of 1.3–1.5 μm. Efforts have been paid to extend the InAs dots emissions to 1.3 μm. One direct way is to grow large dots without dislocation. Murray and Joyce report the direct growth of InAs dots on GaAs to get the 1.3 μm emission at room-temperature [192, 193]. STM showed that InAs dots on GaAs could be grown at very low growth rate of below 0.015 ML/s continuously up to 5 ML without quantum dot coalesence. The light emission saturates around 1.04 eV at 10 K (corresponding to 1.3 μm at room temperature). The dot height saturated at 100 ± 5 Å. But increasing the coverage beyond certain value, such as 3.5 for 0.15 ML, the PL intensity will be reduced. AFM shows the large irregular islands formed at high InAs coverage. TEM reveals the dislocation presence in these dots. This means that the limit of long-wave length emission from InAs dots grown directly on GaAs is 1.2 μm at low temperature (below 10 K) and 1.3 μm at room temperature. Other methods are also used for 1.3 μm emissions. These include growing islands via an alternate growth of sub-monolayers of In, Ga and As using molecular beam epitaxy (MBE) [194, 195] and metal-organic chemical vapor deposition (MOCVD) [196], stacking islands closely [197], and embedding islands with InGaAs or InAlAs alloys [198–200]. And the laser emission at 1.3 μm wavelength is reported by Nakata et al. [201].

5.3. Strain and Dislocations in Quantum Dots

The lattice misfit strain between InAs and GaAs can be released either by 3-D growth or by misfit dislocations. For device applications, dislocations should always be avoided. Dislocation formation is due to the misfit strain accumulation over the value than lattice can endure. Study for strain distribution and relaxation can give information of misfit dislocation. And strain also changes the band structures of semiconductors. Therefore, investigation of strain in quantum dots is very important for avoidance of dislocations and device design. Here strain and dislocations in InAs quantum dots are discussed.

5.3.1. Strain in Quantum Dots

Strain is one of the reasons for quantum dot formation. It affects the electrical and optical properties of quantum dots. The effects of strain on electrical properties can be described

by deformation potential [212]. The band lineup for conduction and valence band in quantum well can be predicted very well by this treatment. But for quantum dots, the situation becomes more complex due to complex strain distribution. Strain distribution in InAs quantum dots was calculated using atomistic model [213, 214], finite-element [215], and analytical. solutions [216, 217] based on continuous model. Finite-element is a very successful method in the mechanical engineering field. But when it was applied to quantum dots, there are difficulties to treat the interface and boundary. Analytical solutions based on continuous model are the simple methods to analyze the strain in quantum dots. But the atomic scale information was lost; as a result, crystal symmetry and anisotropy stress cannot be included. Atomistic model is an accurate method to calculate the strain for quantum dots in principle. But the accurate results need enough dot size and proper interaction potential between atoms. Due to this reason atomistic model require very high computer power. With the increasing of computer power, atomistic model has become a preferred method. The complexity of strain distribution makes the energy level complicated, several detailed discussion can be found in the references [218, 219].

5.3.2. Dislocations in Quantum Dots

Defects become very important for device application. Dislocation is one type of defects that is first investigated. When InAs coverage is larger than certain value, the dislocation begins to form. At this point, quantum dots are no longer coherent to substrates, as shown schematically in Fig. 33. A theoretical analysis is given by Johnson et al. [220]. In their analysis, a 2D model assuming linear elastic behavior is used to analyze an isolated arc shaped island with elastic properties similar to those of the substrate. Finite element analysis shows that in order to minimize the total energy, which consists of strain energy, surface energy, and film/substrate interface energy, a coherent island adopts a particular height-to-width aspect ratio that is a function of the island volume. This analysis indicates that mismatch strain relieving by activating an edge dislocation is favorable for an island with volume greater than a certain critical size. The criterion for the critical size is based on a comparison of the configurational forces acting on the edge of the island in the presence of an edge dislocation. Combining the minimum energy morphology studies for the coherent and dislocated systems with the dislocation nucleation criterion, Johnson and Freund give a model for strained epitaxial island growth [221]. This model gives a qualitative idea for critical size. But it cannot agree quantitatively with experiments. For real quantum dots growth, due to the small size of InAs/GaAs dots, the surface become very important. Different shape will result in difference in elastic strain relaxation and distribution in dots. Therefore, the facets and surface reconstruction must be considered.

Madhukar et al. imaged the dislocation indirectly through terminated morie fringes from plan-view TEM [222]. It is found that the critical size is 21 nm for 420 °C and 22 nm for 480 °C with As_4 pressure of 3×10^{-6} Torr and growth rate of 1/8 ML/s.

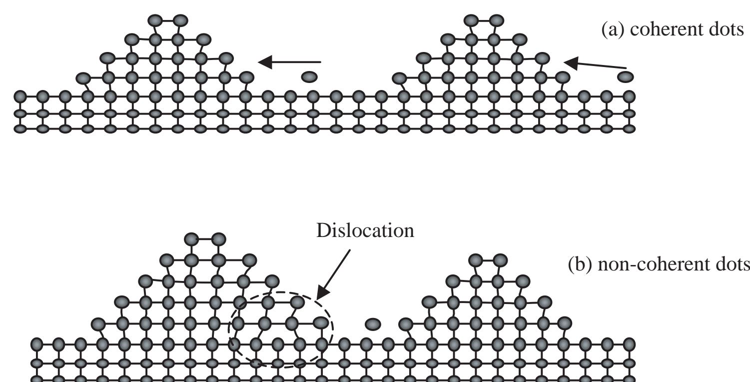

Figure 33. Coherent and non-coherent dots relaxed through dislocation.

5.4. Summary

From above discussion, we can see tremendous progress has been achieved in the past decade. However, current understanding of quantum dot formation still cannot give a complete explanation to all of these detailed self-assembled processes, such as simultaneous appear of these quantum dots at a critical coverage and very narrow size and shape distribution for quantum dots. Theoretical studies is being carried out to explore these questions, but disagreement between experimental results still exists there [223, 224]. For InAs quantum dot epitaxy, there are many details that are not well understood, for example, the role of As BEP. Therefore, many works still have to be done in order to completely understand all these features from experiments.

6. OTHER GROUP QUANTUM DOTS

6.1. Self-Organized GaN Quantum Dots on AlN

The prospects of light emitters and detectors in the blue-UV wavelength range have led to substantial research interests in quantum dot structures of III–V nitrides, especially the AlGaN family that spans the composition range from AlN to GaN. The lattice constant of GaN is 2.7% larger than that of AlN. GaN grown on AlN is under compressive stress and the growth proceeds in Stranski-Krastanov (SK) mode under particular growth condition [225].

One unique feature of AlGaN alloy is that it is polymorphic with either wurtzite or zinc-blende structures. Figure 34 shows a high resolution electron micrograph (HRTEM) of GaN quantum dots separated by AlN spacer layers grown on an AlN(0001) substrate. The GaN wetting layers of approximately 2 MLs thick in between GaN dots are clearly visible showing that the growth is indeed in SK mode. Moreover, there is obvious vertical correlation between GaN dots [226]. Similar correlation has been observed in other materials systems including Ge dots on Si (001) [227, 228] and InAs dots on GaAs. In GaN on AlN, the GaN quantum dots remain vertically correlated up to 20 nm of the AlN spacer layer thickness. Vertical correlation leads to narrower dot size dispersion. A mechanism is proposed for the improved dot size uniformity in Ge/Si materials system.

Aside from the SK growth mode, there are distinct differences between GaN quantum dots on AlN substrates in wurtzite versus zinc-blende structures. Probably the most important difference from the standpoint of optoelectronic application is that GaN in wurtzite

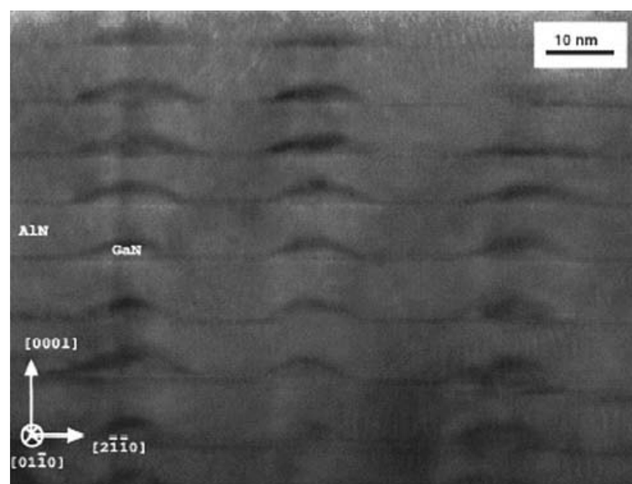

Figure 34. HREM image, taken along the [01–10] direction of a superlattice of GaN dots capped by AlN. The growth temperature was 720 °C. Because of the low magnification of the printed image, the atomic columns are not seen although they are present. The two-dimensional GaN wetting layer is clearly visible. Note the dislocation line running through the column of dots at the left-hand side. Reprinted with permission from [226], F. Widmann et al., "Growth Kinetics and Optical Properties of Self-Organized GaN Quantum Dots," *J. Appl. Phys.* 83, 7618–7624 (1998). © 1998, American Institute of Physics.

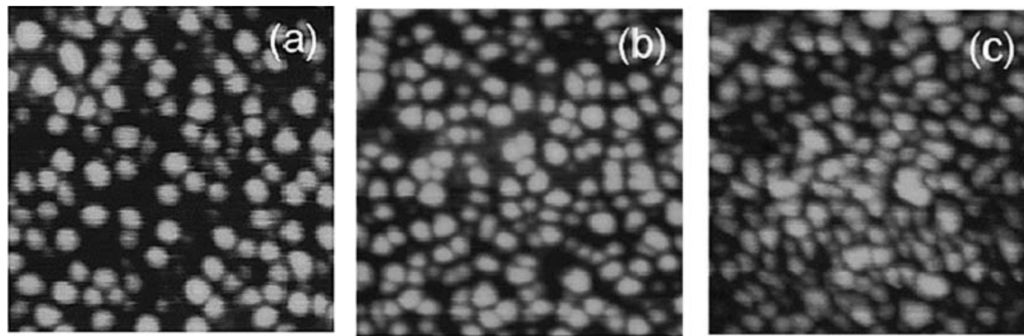

Figure 35. 200 nm×200 nm AFM image obtained in tapping mode. T_s = 725 °C (b) T_s = 705 °C (c) T_s = 685 °C. Reprinted with permission from [226], F. Widmann et al., "Growth Kinetics and Optical Properties of Self-Organized GaN Quantum Dots," *J. Appl. Phys.* 83, 7618–7624 (1998). © 1998, American Institute of Physics.

structure comes with an internal electric field [229] which is absent in GaN in zinc-blende structure. The internal field results in several undesirable properties including low exciton oscillator strengths and long radiative lifetime. Moreover, zinc-blende quantum dots show strong ultraviolet PL emission that is blue-shifted with respect to bulk GaN band gap energy, presumably due to quantum confinement. This is in clear contrast to luminescence from wurtzite GaN dots in which the peak is shifted towards long wavelength side. It has been attributed to the well-known quantum confined Stark effect due to the strong internal field. To avoid the undesirable consequences of the internal field, zinc-blende nitride structures are grown along the non-polar [001] axis on GaAs (001) or 3C-SiC (001) substrate.

Structurally, GaN quantum dots in the two different crystalline structures have different aspect ratio: 1:8 for zinc-blende versus 1:5 for wurtzite. This can be explained by the different surface energy between the two structures.

The growth mechanism of GaN quantum dot has been investigated experimentally by many groups. Widmann et al. [230] studied the influence of the growth temperature on the GaN quantum dots by depositing GaN at 685 °C, 705 °C, and 725 °C. The resulting surface morphology was measured using 200 nm × 200 nm scans of AFM in tapping mode (Fig. 35). The trend of decreasing dot density with increasing substrate temperature is clearly visible. This trend is plotted in Fig. 36. Uncertainties in dot density measurements prevent a confident fit of the data to one single Arrhenius behavior. Despite this ambiguity, such monotonic behavior is consistent with the dot density being determined by the diffusion length of Ga adatoms.

Oswald ripening of GaN dots has been experimentally observed. Figure 37 shows the morphological differences of GaN quantum dots grown under identical conditions at 700 °C

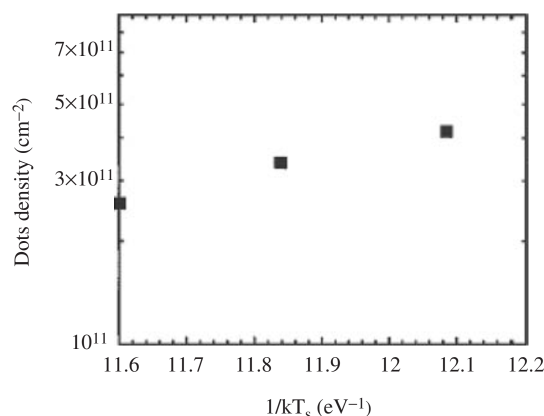

Figure 36. Dependence of GaN dot density on substrate temperature. Reprinted with permission from [226], F. Widmann et al., "Growth Kinetics and Optical Properties of Self-Organized GaN Quantum Dots," *J. Appl. Phys.* 83, 7618–7624, 1998. © 1998, American Institute of Physics.

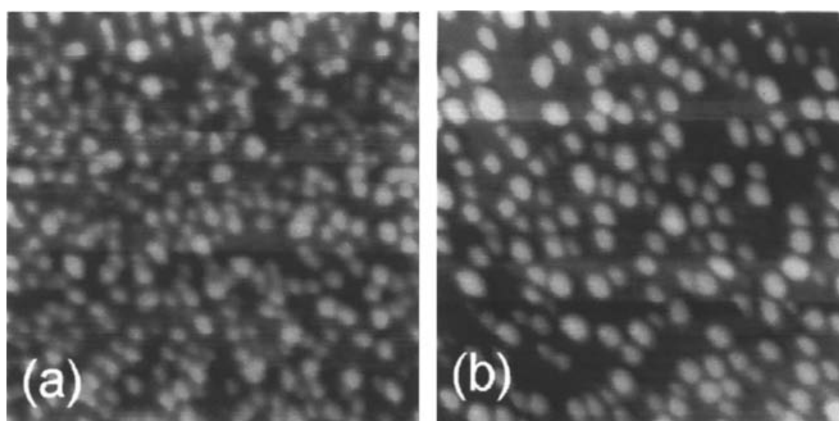

Figure 37. 200 nm×200 nm AFM image obtained in tapping mode for GaN dots grown at 700 °C. (a) Cooled under N plasma flux; (b) cooled under vacuum. Reprinted with permission from [226] F. Widmann, et al., "Growth kinetics and optical properties of self-organized GaN quantum dots", *J. Appl. Phys.* 83, 7618–7624, 1998. © 1998, American Institute of Physics.

with the only difference being the ambient during cooling at the end of the growths. Oswald ripening characterized by lower density and broader dot size distribution is observed from the sample cooled in vacuum [Fig. 37(b)]. In the present growth conditions, (2×2) reconstruction representative of N-terminated surface is observed under active nitrogen flux for temperatures lower than 700 °C. N coverage on the surface is believed to impede surface diffusion of Ga. Oswald ripening is kinetically quenched in this case.

This explanation is corroborated by the annealing experiment at above 700 °C when the reconstruction is faint and eventually disappears indicating the absence of N on the surface. Under this condition, dot ripening was observed both under vacuum and under active nitrogen.

In summary, the polymorphic nature of GaN results in observable differences in the corresponding quantum dot morphology. From the standpoint of optoelectronic device applications, zinc-blende is preferred over wurtzite structure because of the absence of the internal electric field. From the perspective of growth kinetics, Oswald ripening is inhibited on N-terminated surface presumably due to reduced diffusivity of Ga adatoms.

6.2. Self-Assembled PbSe Quantum Dots on PbTe(111) Under Tensile Strain

Despite of the relative scarce in published literature on this family of heterostructures, it is the only known example of epitaxially grown quantum dots that are under tensile strain. This unique feature warrants further discussion as it challenges the validity of the theory making compressive strain a pre-requisite for epitaxial growth of quantum dots.

Pinczolits et al. [231] have investigated the PbSe quantum dots grown on PbTe buffer layers, which were deposited on cleaved $BaF_2(111)$ substrates. The lattice mismatch between PbSe and PbTe is 5.5%. These narrow bandgap semiconductors could be used for mid-infrared diode lasers. It is observed that the PbSe quantum dots are nucleated after the first 1.5 ML, indicating the existence of a wetting layer. In other words, the growth mode is Stranski-Krastanow. They have also investigated $PbSe_{1-x}Te_x$ alloy grown on PbTe(111) with varying composition. It is found when the misfit strain is below 1.6%(Se content <30%), there is no 3D nucleation for the PbSe on PbTe and growth proceeds in Frank van der Merwe mode.

Morphology evolution of PbSe deposited on PbTe(111) was characterized using AFM. The formation of the wetting layer of approximately 1.5 ML thick proceeded via step flow. As the coverage reaches 2 ML, dots of 15 nm height began to appear. It is interesting to note that the dots are not randomly distributed but instead are ordered in pairs, chains or even closed rings. At 3 ML coverage, another type of PbSe dots appears and the sizes of these

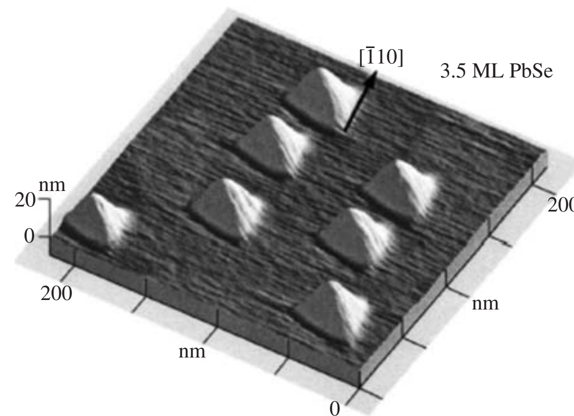

Figure 38. Enlarged 3D AFM image of the PbSe islands at a coverage of 3.5 ML, showing their highly faceted pyramidal shape with their base all aligned along the ⟨110⟩ directions on the surface. The steep {100} side facets are inclined by 54.7 °C out of the surface. Reprinted with permission from [4] M. Pinczolits, et al., "Direct formation of self-assembled quantum dots under tensile strain by heteroepitaxy of PbSe on PbTe (111)", *Appl. Phys. Lett.* 73, 250–252. ©1998, American Institute of Physics.

dots are much smaller than the previous ones. They nucleate randomly in between the large dots. The dots of both types are highly faceted pyramids as shown in Fig. 38. The facets are three intersecting {100} planes inclined at 54.7° with respect to the (111) substrate norm. These (001) planes are the lowest free energy surfaces of the lead salt compounds. The aspect ratio is 1:2.2 and the size distribution of these dots is extremely narrow. The relative height variation is ±12%–17% for the large dots and ±7%–15% for the smaller dots. It is also found that the size distribution is much narrower with increasing coverage of PbSe. It is different from the InAs/GaAs system. Dot size dispersion as narrow as 2% was obtained by Alchalabi et al. [232] in PbSe dots on PbTe quasi-substrate, where the quasi-substrate layer is grown on Si(111).

The physics behind the requirement of compressive strain for epitaxial growth of quantum dots is in the dependence of surface energy on the detailed surface reconstruction and specifically, surface steps. For growths on (001) substrates, the prevailing steps are under tensile strain. These steps are energetically "less expensive" if the film is under compressive strain. Since a rough crystalline surface means higher density of steps, the surface energy of a rough surface of compressively strained films is significantly lower than films under tensile strain. As a result, compressively strained films are more prone to surface roughness.

However, the details of this argument are only applicable to cubic semiconductors grown on (001) oriented substrates. For growth on substrates oriented along different crystallographic directions such as (111) in the case of PbSe on PbTe, the dots have {001} facets with no steps. Consequently, surface roughening is no longer dependent on whether the film strain is tension or compression. In other words, the experimental observation does not contradict the understanding that led to the conclusion with regard to compressive strain.

7. InGaAs QUANTUM DOTS ON Si

7.1. Introduction

The potential application in Si-based optoelectronic devices makes the subject of III–V quantum dots on Si very attractive. Si VLSI technology will benefit greatly if there is a high bit-rate communication channel, such as that used in fiber optic communication, which can be integrated with Si chips. For this very reason, epitaxial growth of various III–V semiconductors on Si has been extensively studied more than 15 years ago [233]. Although an array of devices has been demonstrated, the high density of dislocations in the III–V films prevented them from ever reaching manufacturing. Quantum dots consist of only a few monolayers (MLs) of the active materials, allowing the integration of materials with large lattice mismatch without dislocation. One of such materials combination is InAs quantum

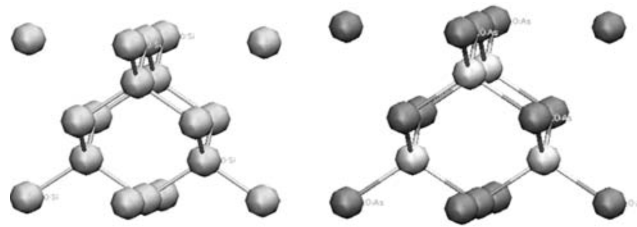

Figure 39. Si and III-asenide bonding configuration along (001) direction.

dot on Si [234–236]. Along with its device application prospects, InAs quantum dot on Si is associated with a particular set of materials challenges including misfit strain and chemical mismatch, i.e., polar materials (III–V materials, such as InAs) on non-polar materials (such as Si). Group IV materials are diamond structure, which is composed by two interpenetrating face-centered cubic (FCC) lattices displaced by one quarter of the body diagonal. Every layer of atoms is composed of the same element as shown in Fig. 39(a). The bonding between atoms is 100% covalent. In contrast, III–V arsenide materials are zinc-blende structure. The inversion symmetry of Si lattice no long exists. Along the (001) direction, which is the orientation of most commonly used substrates, the lattice is composed of alternate layers of group III and group V elements. The bonding between atoms is partially ionic. When III–V material grown on IV substrates, atoms have to rearrange themselves to avoid interface dipole or charge accumulation at interface. This issue is better understood by looking at the picture of proton transfer as shown in Fig. 40 [237]. Imagine a (001) plane with Ge atoms extend infinitely on both sides of this plane. The electronic states in this system have no dipole across this plane. Further imagine now we freeze the electronic structure and transfer protons between the nuclei on one side with another side of the imaginary plane. This operation will change half of atoms to Ga and half atoms to As. The imaginary plane becomes the Ge/GaAs interface. After the proton transfer, the system is allowed to relax to its local energy minimum. Theoretical calculation using LCAO (linear combination atomic orbital) method shows that electron redistribution in the bonds at the interface cannot remove the charge accumulation that arises from the proton transfers. The high interface

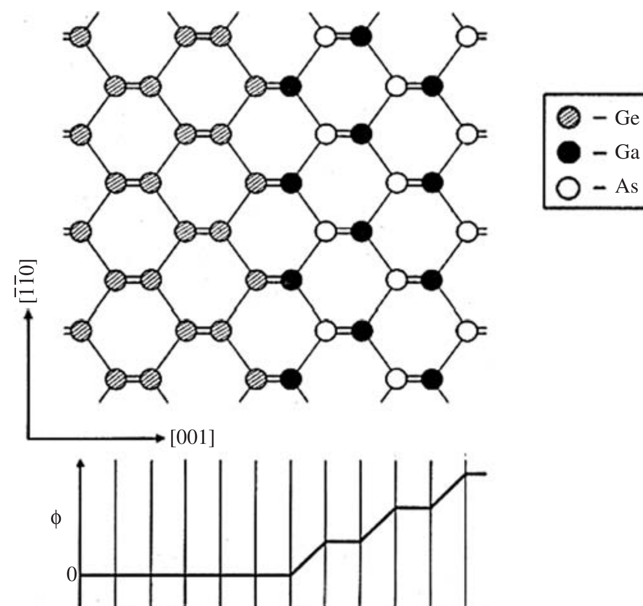

Figure 40. A (001) heterojunction between Ge and GaAs. The potential averaged over planes parallel to the junction, is obtained by integrating Poisson's equation from left to right. A nonzero average electric field has arisen to the right of the junction due to charge accumulation. Reprinted with permission from [5] W. A. Harrison, et al., "Polar heterojunction interfaces", *Phys. Rev. B* 18(8), 4402–4410, 1978. © 1978, The American Physical Society.

energy resulting from the charge imbalance prevents the formation of a sharp interface. Although this picture cannot give the quantitative value for interface dipole, it is very helpful in understanding the chemical mismatch. Here both experimental results and theoretical understanding of III–V quantum dots grown on group IV substrates are discussed.

7.2. III–V Quantum Dots on IV Substrates

For quantum dot epitaxy growth, the surface energy becomes very important. From thermodynamic point of view, the dot formation is the result of total energy minimization. Total energy includes surface energy, interface energy and strain energy. For systems such as InAs/GaAs and Ge/Si, there is no chemical mismatch. The interface energy is very small compared to surface energy. But for III–V on Si or Ge, the interface energy becomes comparable to surface energy [238] and the surface energy is changed due to group V element terminated on the group IV surface. As passivation is one of typical case [239]. In this case, arsenic atoms get on Si or Ge surfaces, they form 2×1 reconstruction and passivate the surface. Replacing Si-Si or Ge-Ge dimmers with As-As dimmers (breaking up the Si-Si or Ge-Ge dimmers and adding As-As dimmers on top) leads to a fully coordinated surface with 2×1 symmetry, as shown in Fig. 41. Every Si (or Ge) has 4 bonds, two with Si (or Ge) itself, two with arsenic. Every arsenic has three bonds, two with Si (or Ge), one with another arsenic, making it an eight-electron outer-shell. As a result, surface energy is very low. Theory shows that under high arsenic flux, the As-dimerized surface has the lowest energy comparing to other configurations including Ga-As dimmer, Si-Si dimmer or Ga-Si dimmer [240]. Total energy calculation by Northrup shows that the layer-by-layer growth of GaAs on Si is not preferred. The initial stage of growth of GaAs on Si shows island formation without any wetting-layer growth [241]. RHEED observation and AFM study of the initial stages for GaAs growth on Si confirmed the Volmer-Web growth mode for GaAs on Si. Figure 42 shows the RHEED pattern before and after 0.4 ML GaAs growth on Si with substrate temperature 370 °C, growth rate 0.01 ML, and As BEP 1.4×10^{-6} Torr. Figure 43 shows the AFM images of GaAs 0.4 ML, and 1.2 ML grown on Si (001). The clear island formation starts from very beginning without 2D wetting-layer growth.

In order to get the properties of chemical mismatch alone. GaAs-Ge system is a simplest and very suitable system to understand the chemical mismatch due to their negligible lattice mismatch (<0.1%). Growth of GaAs on Ge showing island formation indicates that the chemical mismatch can play a dominant role for dot formation. Figure 44 shows the GaAs growth of 30 nm on Ge at 500 °C, with growth rate of 0.12 Å/s, and As BEP of 1.6×10^{-5} Torr. The clear feature of growth is that there is some area without growth. This indicates III–V materials GaAs prefer to grow with island formation at the initial stage with IV material surface exposed or passivated by As. Figure 45 showed the RHEED pattern for GaAs growth of 0.7 ML. Clear 3D growth at initial stage indicates the Volmer-Web growth of GaAs on Ge. Therefore, chemical mismatch (polarity mismatch) alone can push the growth into V–W mode.

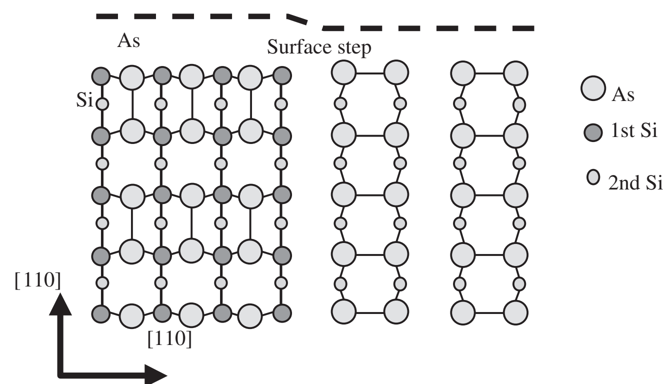

Figure 41. As-terminated Si surface reconstruction.

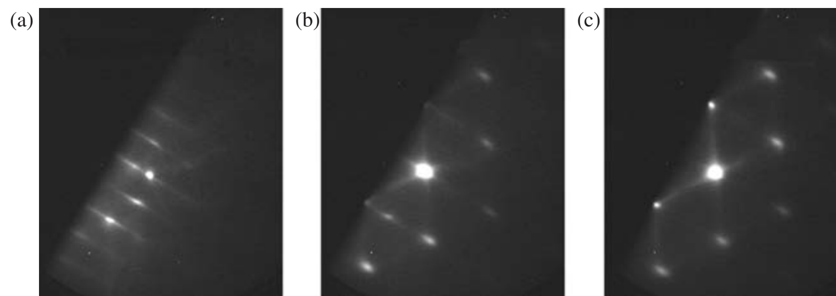

Figure 42. RHEED pattern of GaAs growth on Si, (a) before growth, (b) 0.4 ML growth, (c) 1.2 ML growth.

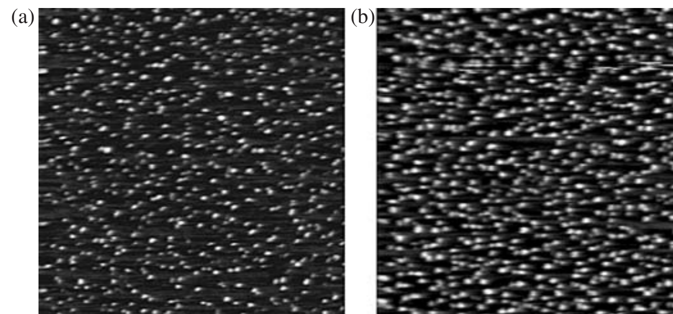

Figure 43. AFM image of GaAs growth 0.4 ML (a) and 1.2 ML (b) on Si.

Figure 44. Bright-field cross-section TEM for GaAs growth on Ge (001) 33 nm.

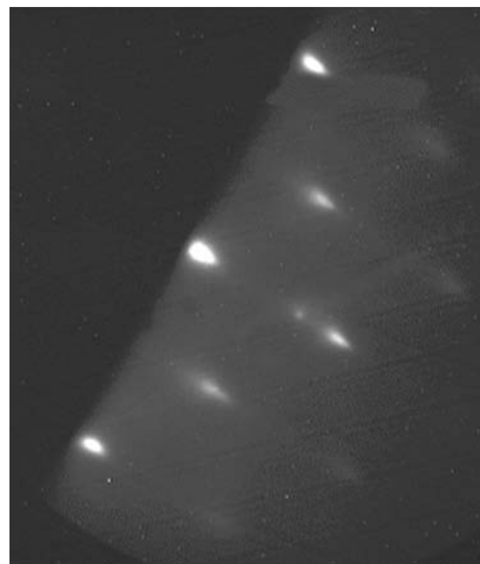

Figure 45. RHEED for 0.7 ML GaAs on Ge.

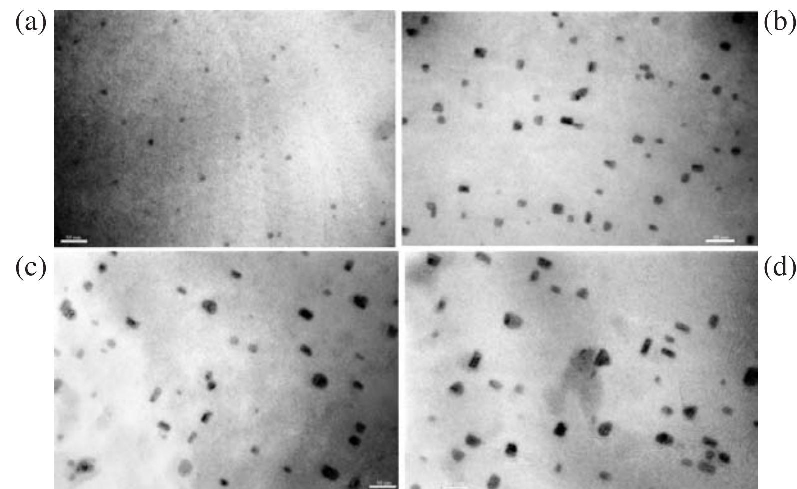

Figure 46. Bright-field plan-view TEM of InAs dots with various InAs nominal coverage (a) 0.3 ML, (b) 0.7 ML, (c) 1.0 ML, (d) 1.4 ML.

For InAs growth on Si (100), the situation becomes more complicated due to both large lattice mismatch (11%) and large chemical mismatch. TEM and RHEED indicate a clear V-W growth. Plan-view TEM images of InAs dots with different InAs nominal coverage are shown in Fig. 46. The density and size dependence on InAs coverage are shown in Fig. 47. TEM results indicate that dot formation begins at very early stage of the growth (<0.3 ML). At 0.3 ML of InAs coverage, the dot density is approximately 1.7×10^{10} cm^{-2} indicating V–W growth mode. Oostra et al. has done Auger experiments on In grown on As-terminated Si surface [242]. The authors claim the V-W growth mode for InAs growth on Si. Figure 47 shows InAs dot density increases slightly up till a coverage of 0.7 ML. Further growths result in a significant broadening of dot size distribution indicating coarsening. Figure 48 shows the cross-section TEM of typical InAs dots with the different coverage. With increasing InAs coverage, not only dot size but also shapes of the dots change. Most dots have an irregular shape at 0.3 ML coverage. That changes to highly regular huts with (111) facets at 0.7 ML. At 1.0 ML, portion of dots evolves into dome shape with no clear facets. At 1.4 ML, nearly 100% of the dots are dome shape.

One unusual feature for InAs dots on Si is the weak dependence of dot density on substrate temperature. Dot density dependence on substrate temperature is not an exponential feature that has been expected by Eq. (8). Figure 49 shows the bright-field plan-view TEM of samples grown at different substrate temperature. Substrate temperature was increased from 295 °C for (a) to 410 °C for (e) in Fig. 49. From the right side of Fig. 49, it is very clear that increasing substrate temperature results in broadening of dot size distribution. The

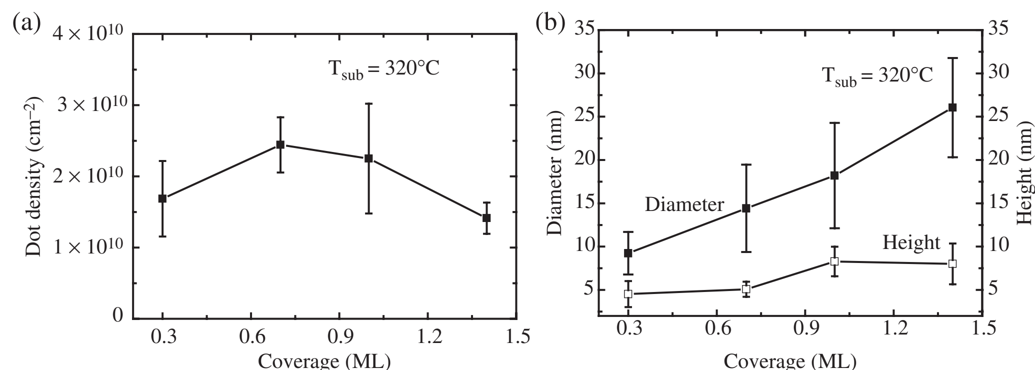

Figure 47. (a) Plot of InAs dot density dependence on the nominal coverage and (b) Plot of InAs dot size dependence on the nominal coverage.

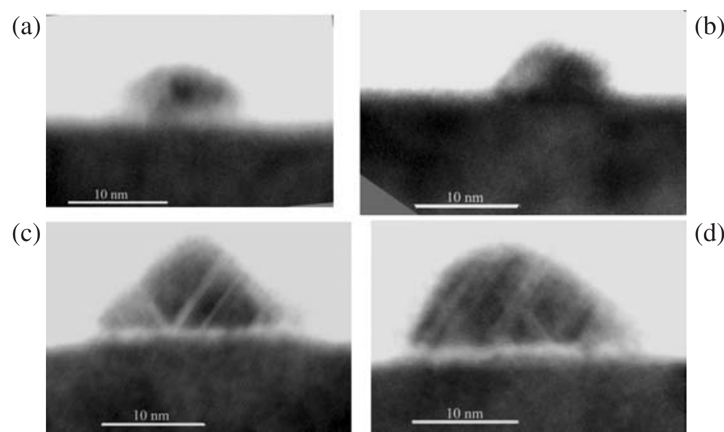

Figure 48. Bright-field cross-section TEM of typical InAs dots with different InAs nominal coverage: (a) 0.3 ML, (b) 0.7 ML, (c) 1.0 ML, (d) 1.4 ML.

peak width from Guassian fitting of the size distribution increased from 8 nm to 14 nm when substrate temperature was increased from 295 °C to 410 °C. It is likely that the broadening of dot size distribution is due to coarsening with larger dots having lower chemical potential. Higher substrate temperature causes more rapid surface diffusion and subsequently more significant coarsening. Dot density is only lightly dependent on substrate temperature as shown in Fig. 50. This behavior suggested that nucleation model based on surface diffusion is not applicable for InAs dot formation on Si, although it affects dot size distribution. There is other dominant factor controlling the dot formation. Experimental results indicate the As BEP and In flux control the dot density. Figure 51 shows the bright-field TEM images for dots grown with different As BEP at growth temperature 320 °C. The dot density increased tremendously with decreasing As BEP. Figure 52(a) shows the plot of density versus As BEP. Dot density increases nearly two orders of magnitude with decreasing As BEP by two orders of magnitude. InAs dot density increases in a near power-law fashion from 4.3×10^9 to 1.8×10^{11} cm^{-2} as As BEP is decreased from 9.2×10^{-6} to 1.2×10^{-7} torr. The dot size and dot volume change with As BEP is shown in Fig. 52(b). InAs dot size and volume change with decreasing As BEP. The total dot volume decreases at low As BEP. This indicates that there are 2-dimensional InAs structures formed between dots at low As BEP. This is likely attribute to the increasing of surface energy with decreasing As BEP as calculated by Northrup [243].

Compared with InAs on Si, GaAs dot growth on Si (001) is independent with As BEP. Figure 53 shows the InAs dot density and GaAs dot density change with As BEP in log-log scale. A clear contrast can be distinguished from this plot. This suggests that there is fundamental difference in dot formation between InAs and GaAs on Si.

To understand this particular behavior, first-principle calculation was carried out with the plane-wave pseudopotential method within the generalized gradient approximation (GGA). A conjugate-gradient algorithm is used to minimizing the total energy therefore obtain the atom positions. Figure 54 shows the positions of atoms in different systems with different InAs overlayers on silicon (001). We calculated the total energies of systems with different thickness of InAs on silicon substrate, which is shown in Table 1. Comparing the total energy of two systems with the same number of atoms, while one system has half surface area covered with single As layer and half covered with As-In-As-In-As layer and another one with the whole surface covered with As-In-As layer, we can find the former one has a total energy of $-(63.40 + 92.36)/2$ eV $= -77.88$ eV, which is lower than the total energy (-77.82 eV) of system with a uniform As-In-As layer. For a system with 1/3 area covered with As-In-As-In-As-In-As and 2/3 with single As, the total energy is $-(106.97/3 + 63.40 \times 2/3)$ eV $= -77.92$ eV, which is even lower. So the system prefers to form InAs islands with As-finished silicon surface rather than uniform InAs layer on silicon surface. This causes a 3D growth mode of InAs on silicon even in the very initial stage. Further more, since the

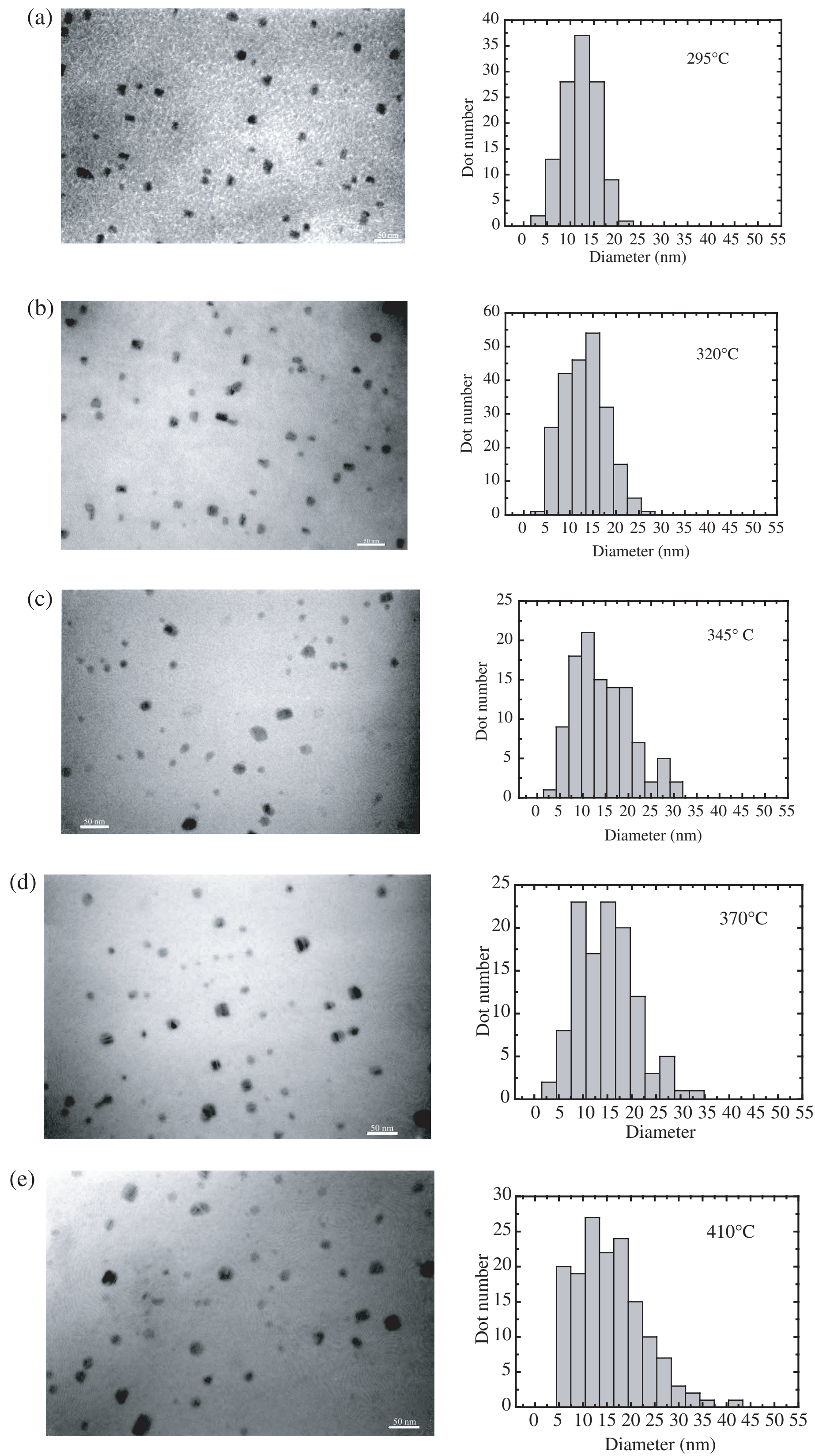

Figure 49. Plane-view TEM of InAs quantum dots grown at (a) 295 °C, (b) 320 °C, (c) 345 °C, (d) 370 °C, (e) 410 °C. and histogram for size distribution.

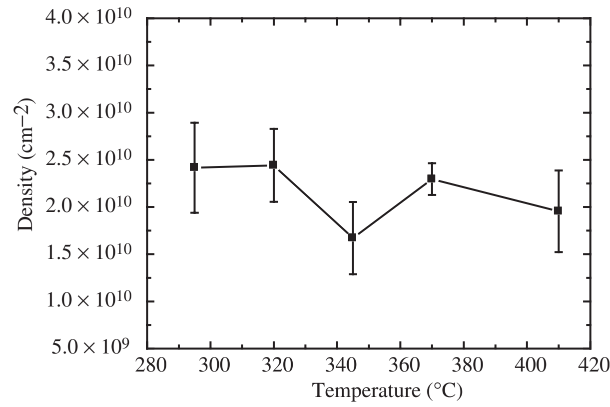

Figure 50. Plot of InAs dot density (y axis) dependence on substrate temperature (x axis).

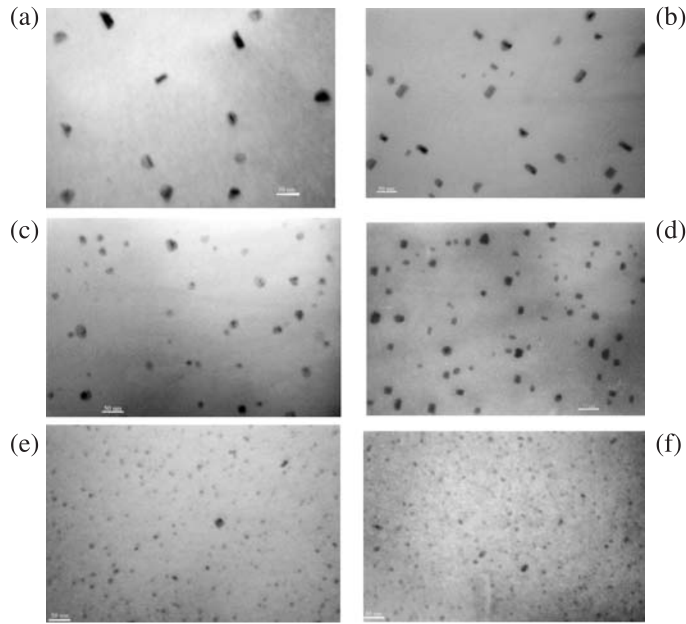

Figure 51. Bright-field plan-view TEM of InAs dots Vs As BEP (a) 9.2×10^{-6} torr, (b) 5.4×10^{-6} Torr, (c) 1.4×10^{-6} Torr, (d) 3.0×10^{-7} Torr. 2.1×10^{-7} Torr, (f) 1.2×10^{-7} Torr.

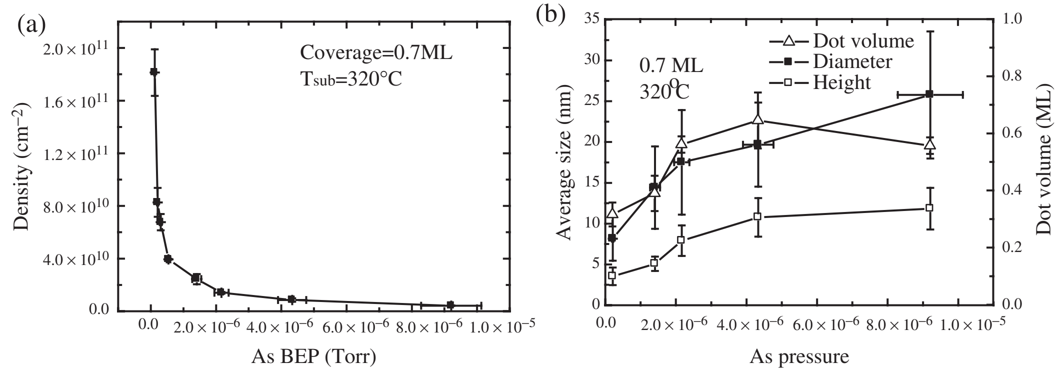

Figure 52. (a) Plot of InAs dot density dependence on arsenic BEP, (b) Plot of InAs dot size and volume dependence on arsenic BEP.

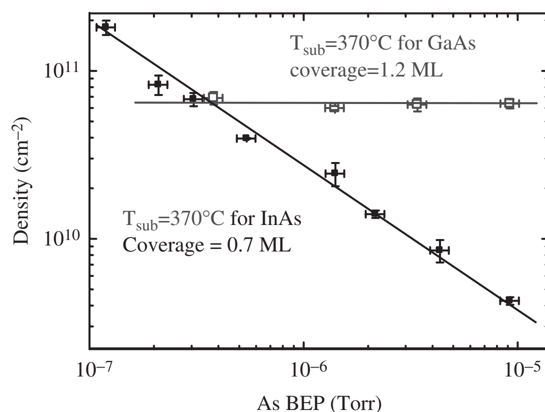

Figure 53. InAs dots and GaAs Dots density dependence on As BEP.

island formation in 3D growth will partially release the strain energy that comes from the lattice mismatch between InAs and Si, the 3D growth will be even more energy favorable.

The optical properties of InAs dots embedded in Si matrix were also reported [244, 245]. But the reason where and how radiative recombination happens is still under discussion. High-resolution transmission electron microscopy shows the formation of an InAs solid solution in the Si cap layer after annealing at 800 °C. The photoluminescence at 1.3 μm region has been attributed to the recombination of excitons localized in the ordered regions which is InAs enriched region with extensions of ~6 nm [246]. From the decay time of PL, the carrier lifetime of 400 ns is obtained [247]. This lifetime is much larger than that of InAs

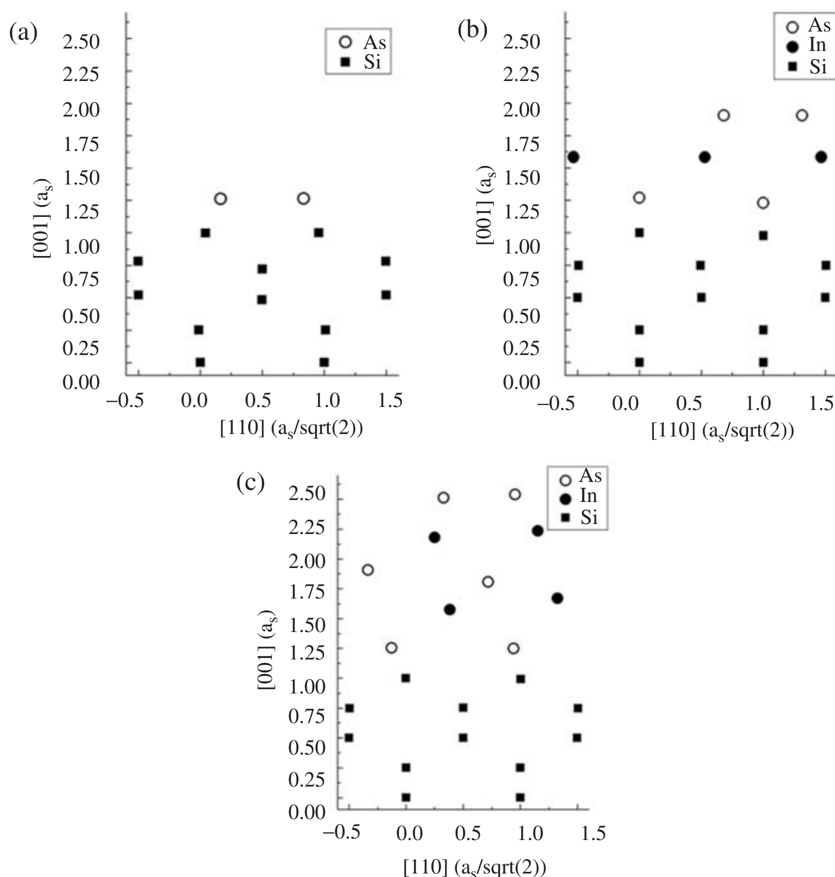

Figure 54. Calculation positions of atoms in (a) Si(001)-As, (b) Si(001)-As-In-As and (c) Si(001)-As-In-As-In-As.

Table 1. Total energies of systems with different InAs overlayers on silicon. The unit area used in the table is the area for one surface dimmer.

Structure	Total energy (eV/unit area)
Si(001)-As	−63.40
Si(001)-As-In-As	−77.82
Si(001)-As-In-As-In-As	−92.36
Si(001)-As-In-As-In-As-In-As	−106.97

quantum dots embedded in GaAs, which is 400–2000 ps depending growth conditions. This suggests the carrier recombination observed in InAs/Si system is fundamentally different from InAs/GaAs. The recombination is mostly like to be indirect transition in type-II band alignment. Later report by Fukatsu et al. shows that PL can be observed from both InAs and GaSb quantum dots embedded in Si. The authors suggest that the PL is from carrier recombination at III–V and Si interface [248]. In addition, the authors demonstrated EL of GaSb quantum dots in Si matrix at room-temperature.

7.3. Summary

Great progress has been made in III–V quantum dots epitaxy on Si, although several questions still need further studying. These questions include atomic arrangement at interface between InAs and Si, unusual InAs dot density dependence on As BEP, band-diagram for InAs dots in Si matrix and defects including dislocations, antiphase domain boundaries and point defects.

8. CONCLUSION

The topic of self-assembly of semiconductor quantum dots via epitaxy has been reviewed in this chapter. The emphasis has been on the various materials science and engineering issues pertinent to the topic.

Recognizing that the interest in fabrication semiconductor quantum dots stems primarily from the anticipated device applications, this chapter begins with a survey of the various quantum dot based devices. The survey shows us that while the requirement on the quantum dot property depends on the specific type of device, there exists an over riding need for controlling dot density and size uniformity. The remaining discussions with regard to the various hetero-structures are all carried out following the common theme.

To lay down the physics background for the discussion, the next section introduces the current understanding of the formation of quantum dots by epitaxy. The driving force comes from the minimization of the Gibbs free energy of the hetero-structure. The key factors influencing the equilibrium morphology include the surface energy, interface energy, and the misfit strain. There are subtleties under this umbrella of qualitative understanding such as the function of the ever-present facet on the overall energy balance, the result of the unavoidable local fluctuation in the adatom density, and other details that remain not well understood. One example is the fact that nearly 100% of the experimental studies are on materials combinations in which the material that forms the dots is under compression. This observation points to the fact that surface energy of the quantum dots depends not only on the magnitude of the misfit strain, but also the sign of the strain. Quantitative prediction of the equilibrium morphology of a surface containing quantum dots remains at this time an extremely challenging task.

The following sections provide reviews on the fabrication of quantum dots from several different materials combinations including Ge on Si, InAs on GaAs, GaN on AlN, PbSe on PbTe and InAs on Si.

Ge on Si represents the simplest hetero-structure. The study of this simple hetero-structure provided a lot of valuable information for the understanding of quantum dot formation mechanism. Substrate temperature and Ge growth rate are the two major factors affecting

the quantum dot growth kinetics. There exists a distinct pyramid-to-dome transition. The critical island size at which the transition takes place monotonically decrease with increasing misfit strain and can be used as an indicator of misfit strain. There also exists dome-to-pyramid transition, which has been shown to be a result of decreasing misfit strain as a result of the intermixing between Ge and Si. Growth of Ge quantum dots over a buried misfit dislocation network has been shown to be a valuable experimental vehicle for studying the adatom kinetics as well as providing insight into the various stages in quantum dot nucleation and growths.

InAs on GaAs is the first compound semiconductor materials families reviewed in this chapter. Comparing to Ge on Si, one more factor that plays an important role in the growth kinetics in addition to the substrate temperature and the film growth rate is the partial pressure of the group V element. For example, InAs quantum dot density depends sensitively on the As pressure at substrate temperature below 480 °C. Such dependence is absent for higher substrate temperatures. A more subtle function of As pressure is a noticeable influence on the photoluminescence property of InAs quantum dots. It appears the photoluminescence efficiency increases and the emission peak narrows with increasing substrate temperature and decreasing As pressure. The likely reason is the point defect density.

GaN on AlN represents another family of compound semiconductors. The unique features include the fact that GaN is polymorphic, i.e., it can exist in zinc-blende or wurtzite structures. Moreover, wurtzite GaN is associated with a large build-in electric field, which leads to the spatial separation of electrons and holes resulting in decreased oscillator strength as well as reduced photon energy in luminescence.

Another family of quantum dots reviewed in this chapter is that of PbSe on PbTe. The reason this family is included in this review despite of the fact only very few publications are in the literature is that it represents the only case in which the quantum dots are under tensile strain. The reason for this behavior is traced to the detailed atomic construction of the prevailing facets. In that case the island surfaces are composed of perfect {100} facets with no surface steps present. As a result, the consideration stemming from the tension associated with surface steps in (001) oriented diamond and zine-blende semiconductors no longer apply.

All three families of hetero-structures, namely, Ge on Si, InAs on GaAs, and GaN on AlN, are composed of chemically similar materials with the associated strong bonding across the hetero-interface, i.e., low interface energy. The few percent lattice mismatch in combination with the low interface energy dictates that the growth mode be Stranski-Krastanow.

The fabrication of InAs quantum dots on Si (001) has with it the added complication of polar on non-polar interface. The same issue exists for GaAs on Si (001). The high interface energy results in Vomer-Weber growth. The reduced interaction between the quantum dots and the substrate manifests through the lack of registration between the quantum dots and a buried dislocation network. As a result, the self-assembly process is dominated more by the surface diffusion length of adatoms than the strain field interaction between adjacent dots. The 11% lattice mismatch between InAs and Si dictates that the critical dot size for dislocation is small. Experimental results show that the critical size is a function of As pressure and could be smaller than 10 nm. Such small critical island size indicates the absence of a process window for the intended optoelectronic device application using InAs quantum dots in Si. This is because that quantum confinement renders the energy band gap of a 10 nm size InAs quantum dot to be significantly larger than that of Si leading to no confinement of excitons.

In conclusion, self-assembly of semiconductor quantum dots via epitaxy is an exciting topic for scientific research as well as novel devices. The challenge remains in controlling the dot density and size uniformity.

ACKNOWLEDGMENT

The authors would like to acknowledge the funding support to our research on this subject with some of the results presented in this article. ARO (Grant No. DAAD19-01-1-0532 and DAAD19-01-1-0690).

REFERENCES

1. S. A. Empedocles, D. J. Norris, and M. G. Bawendi, *Phys. Rev. Lett.* 77, 3873–3876 (1996).
2. J. Shi, K. Zhu, Q. Zheng, L. Zhang, L. Ye, J. Wu, and J. Zuo, *Appl. Phys. Lett.* 70, 2586 (1997).
3. Y. H. Xie, G. H. Gilmer, C. Roland, P. J. Silverman, S. K. Buratto, J. Y. Cheng, E. A. Fitzgerald, A. R. Kortan, S. Schuppler, M. A. Marcus, and P. H. Citrin, *Phys. Rev. Lett.* 73, 3006 (1994).
4. M. Pinczolits, G. Springholz, and G. Bauer, *Appl. Phys. Lett.* 73, 250 (1998).
5. W. A. Harrison, E. A. Kraut, J. R. Waldrop, and R. W. Grant, *Phys. Rev. B* 18, 4402 (1978).
6. M. Asada, A. Kameyama, and Y. Suematsu, *J. Quantum Electron.* 20, 745 (1984).
7. Y. Miyamoto, Y. Miyake, M. Asada, and Y. Suematsu, *IEEE J. Quantum Electron.* 25, 2001 (1989).
8. Y. Arakawa and H. Sakaki, *Appl. Phys. Lett.* 40, 939 (1982).
9. H. Jiang and J. Singh, *Appl. Phys. Lett.* 85,7438 (1999).
10. G. T. Liu, A. Stintz, H. Li, K. J. Malloy, and L. F. Lester, Digest of the LEOS Summer Topical Meetings, IEEE Catalog #99TH8455, p. 19, 1999.
11. G. T. Liu, A. Stintz, H. Li, K. J. Malloy, and L. F. Lester, Digest of the LEOS Summer Topical Meetings, IEEE Catalog #99TH8455, p. 19, 1999.
12. M. Grundmann, *Physica E* 5, 167 (2000).
13. N. Kirstaedter, O. Schmidt, N. N. Ledentsov, D. Bimberg, V. M. Ustinov, A. Yu. Egorov, A. E. Zhukov, M. V. Maximov, P. S. Kop'ev, and Zh. I. Alferov, *Appl. Phys. Lett.* 69, 1226 (1996).
14. N. Kirstaedter, O. Schmidt, N. N. Ledentsov, D. Bimberg, V. M. Ustinov, A. Yu. Egorov, A. E. Zhukov, M. V. Maximov, P. S. Kop'ev, and Zh. I. Alferov, *Appl. Phys. Lett.* 69, 1226 (1996).
15. S. Zaitsev, N. Yu. Gordeev, V. I. Kopchatov, V. M. Ustinov, A. E. Zhukov, A. Yu. Egorov, N. N. Ledentsov, M. V. Maximov, P. S. Kop'ev, A. O. Kosogov, and Zh. I. Alferov, *Jpn. J. Appl. Phys.* 36, 4219 (1997).
16. A. Patane, A. Polimeni, M. Henini, L. Eaves, P. C. Main, and G. Hill, *J. Appl. Phys.* 85, 625 (1999).
17. M. Grundmann and D. Bimberg, *Jpn. J. Appl. Phys.* 36, 4181 (1997).
18. H. Shoji, Y. Nakata, K. Mukai, Y. Sugiyama, M. Sugawara, N. Yokoyama, and H. Ishikawa, *IEEE J. Select. Topics in Quant. Electr.* 3, 188 (1997).
19. M. V. Maximov, N.Yu. Gordeev, S. V. Zaitsev, P. S. Kop'ev, I. V. Kochnev, N. N. Ledentsov, A. V. Lunev, S. S. Ruvimov, A. V. Sakharov, A. F. Tsatsul'nikov, Yu. M. Shernyakov, Zh. I. Alferov, D. Bimberg, *Semiconductors* 31, 124 (1997).
20. Yu. M. Shernyakov, D. A. Bedarev, E. Yu. Kondrat'eva, P. S. Kop'ev, A. R. Kovsh, N. A. Maleev, M. V. Maximov, S. S. Mikhrin, A. F. Tsatsul'nikov, V. M. Ustinov, B. V. Volovik, A. E. Zhukov, Zh.I. Alferov, N. N. Ledentsov, and D. Bimberg, *Electron Lett.* 35, 898 (1999).
21. H. R. Choo, B.-H. O, C. D. Park, H. M. Kim, J. S. Kim, D. K. Oh, H. M. Kim, and K. E. Pyun, *IEEE Photon. Technol. Lett.* 10, 645 (1998).
22. R. Krebs, F. Klopf, S. Rennon, J. P. Reithmaier, and A. Forchel, *Elctronics Lett.* 37, 1223 (2001).
23. V. Ryzhii, I. Khmyrova, V. Mitin, M. Stroscio, and M. Willander, *Appl. Phys. Lett.* 78, 3523 (2001).
24. J. D. Phillips, *J. Appl. Phys.* 91, 4590 (2002).
25. U. Bockelman and G. Bastard, *Phys. Rev. B* 42, 8947 (1990).
26. H. Benisty, C. M. Sotomayer-Torres, and C. Weisbuch, *Phys. Rev. B* 44, 10945 (1991).
27. H. Grabert and M. H. Devoret, Eds., "Single Charge Tunneling." Plenum, New York, 1992.
28. K. K. Likharev and A. N. Korotkov, *Proc. 1995 ISDRS* 355 (1995).
29. K. K. Likharev, *Appl. Phys. Lett.* 73, 2137 (1998).
30. R. C. Ashoori, H. L. Stormer, J. C. Weiner, L. N. Pfeiffer, K. W. Baldwin, S. J. Pearton, and K. W. West, *Phys. Rev. Lett.* 68, 3088 (1992).
31. D. J. Mar, R. M. Westervelt, and P. F. Hopkins, *Appl. Phys. Lett.* 64, 631 (1994).
32. P. L. McEuen, E. B. Foxman, U. Meirav, M. A. Kastner, Y. Meir, N. S. Wingreen, and S. J. Wind, *Phys. Rev. Lett.* 66, 1926–1929 (1991).
33. L. J. Geerligs, V. G. Anderegg, P. A. M. Holweg, J. E. Mooij, H. Pothier, D. Esteve, C. Urbina, and M. H. Devoret, *Phys. Rev. Lett.* 64, 2691–2694 (1990).
34. J. K. Pekola, K. P. Hirvi, J. P. Kauppinen, and M. A. Paalanen, *Phys. Rev. Lett.* 73, 2903 (1994).
35. Y.-W. Mo, D. E. Savage, B. S. Swartzentruber, and M. G. Lagally, *Phys. Rev. Lett.* 65, 1020(1990).
36. F. M. Ross, J. Tersoff, and R. M. Tromp, *Phys. Rev. Lett.* 80, 984 (1998).
37. F. M. Ross, R. M. Tromp, and M. C. Reuter, *Science* 286, 1931 (1999).
38. T. I. Kamins, G. Medeiros-Ribeiro, D. A. A. Ohlberg and R. Stanley Williams, *Appl. Phys. A* 67, 727 (1998).
39. V. Yam, V. Le Thanh, D. Débarre, Y. Zheng, and D. Bouchier, *Appl. Surf. Sci.* 224, 143 (2004).
40. S. A. Chaparro, J. Drucker, Y. Zhang,D. Chandrasekhar, and M. R. McCartney, *Phys. Rev. Lett.* 83, 1199 (1999).
41. K. E. Khor and S. Das Sarma, *J. Vac. Sci. Technol. B* 15, 1051 (1997).
42. X. Z. Liao, J. Zou, D. J. H. Jiang, X. Wang, and R. Leon, *Appl. Phys. Lett.* 77, 1304 (2000).
43. T. B. Massalski, J. L. Murray, L. H. Bennett, and H. Baker, "Binary Alloy Phase Diagrams." ASM, Metals Park, Ohio, 1986.
44. J. Räisänen, J. Hirvonen, and A. Anttila, *Solid State Electron.* 24, 333 (1981).
45. R. S. Williams, G. Medeoros-Ribeiro, T. I. Kamins, and D. A. A. Ohlberg, *Acc. Chem. Res.* 32, 425 (1999).
46. M. Goryll, L. Vescan, and H. Lüth, *Thin Solid Films* 336, 244 (1998).
47. Y.-W. Mo, D. E. Savage, B. S. Swartzentruber, and M. G. Lagally, *Phys. Rev. Lett.* 65, 1020 (1990).
48. T. I. Kamins, G. Medeoros-Ribeiro, D. A. A. Ohlberg, and R. S. Williams, *J. Appl. Phys.* 85, 1159 (1999).

49. K. Nakajima, A. Konishi, and K. Kimura, Phys. *Rev. Lett.* 83, 1802 (1999).
50. F. M. Ross, *IBM J. Res. Dev.* 44, 489 (2000).
51. Y.-W. Mo, J. Kleiner, M. B. Webb, and M. G. Lagally, *Surf. Sci.* 268, 275 (1992).
52. F. M. Ross, J. Tersoff, and R. M. Tromp, *Phys. Rev. Lett.* 80, 984 (1998).
53. H.-J. Gossmann, L. C. Feldman, and W. M. Gibson, *Surf. Sci.* 155, 413 (1985).
54. M. A. Lutz, R. M. Feenstra, F. K. LeGoues, P. M. Mooney, and J. O. Chu, *Appl. Phys. Lett.* 66, 724 (1995).
55. T. I. Kamins and R. S. Williams, *Appl. Phys. Lett.* 71, 1201 (1997).
56. Y.-H. Wu, C.-Y. Wang, A. Elfving, G. V. Hansson, and W.-X. Ni, *Mater. Sci. Eng. B* 89, 151 (2002).
57. D. Srivastava and B. J. Garrison, *Phys. Rev. B* 46, 1472 (1992).
58. C. Roland and G. H. Gilmer, *Phys. Rev. B* 47, 16286 (1993).
59. R. Kariotis and M. G. Lagally, *J. Vac. Sci. Technol. B* 7, 269 (1989).
60. M. Tomellini and M. Fanfoni, *Current Opinon in Solid State and Mat. Sci.* 5, 91 (2001).
61. Y.-W. Mo, J. Kleiner, M. B. Webb, and M. G. Lagally, *Surf. Sci.* 268, 275 (1992).
62. M. Zinke-Allmang, L. C. Feldman, and M. H. Grabow, *Surf. Sci.* 200, L427 (1988).
63. Y.H Xie, S. B. Samavedam, M. Bulsara, T. A. Langdo, and E. A.Fitzgerald, *Appl. Phys. Lett.* 71, 3567 (1997).
64. Y.-W. Mo and M. G. Lagally, *Surf. Sci.* 248, 313 (1991).
65. J. M. C. Thornton, A. A. Williams, J. E. Macdonald, R. G. van Silfhout, J. F. van der Veen, M. Finney and C. Norris, *J. Vac. Sci. Technol. B* 9(4), 2146 (1991).
66. M. Katayama, T. Nakayama, M. Aono, and C. F. McConville, *Phys. Rev. B* 54, 8600 (1996).
67. C. S. Peng, Q. Huang, W. Q. Cheng, J. M. Zhou, Y. H. Zhang, T. T. Sheng, and C. H. Tung, *Appl. Phys. Lett.* 72, 2541 (1998).
68. A. Portavoce, F. Volpi, A. Ronda, P. Gas, and I. Berbezier, *Thin Solid Films* 380, 164 (2000).
69. A. Portavoce, A. Ronda, and I. Berbezier, *Mater. Sci. Eng. B* 89, 205 (2002).
70. H. Jorke, *Surf. Sci.* 193, 569 (1988).
71. K. D. Hobart, D. J. Godbey, M. E. Twigg, M. Fatemi, P. E. Thompson, and D. S. Simons, *Surf. Sci.* 334, 29 (1995).
72. N. Kirstaedter, N. N. Ledentsov, M. Grundmann, D. Bimberg, V. M. Ustinov, S. S. Ruvimov, M. V. Maximov, P. S. Kop'ev, Zh. I. Alferov, U. Richter, P. Werner, U. Gsele, and J. Heydenreich, *Electon. Lett.* 30, 1994 (1416).
73. J. Phillips, P. Bhattacharya, S. W. Kennerly, D. W. Beekman, and M. Dutta, *IEEE J. Quantum Electron.* 35, 1999 (936).
74. M. Grundmann, J. Christen, N. N. Ledentsov, J. Böhrer, D. Bimberg, S. S.Ruvimov, P. Werner, U. Richter, U.Gösele, J. Heydenreich, V. M. Ustinov, A. Yu. Egorov, A. E. Zhukov, P. S. Kop'ev, and Zh. I. Alferov, *Phys. Rev. Lett.* 74(20), 1995 (4043).
75. K. H. Schmidt, G. Medeiros-Ribeiro, J. Garcia, and P. M. Petroff, *Appl. Phys. Lett.* 70(13), 1997 (1727).
76. M. Schroeder and D. E. Wolf, *Phys. Rev. Lett.* 74 1995 (2026).
77. R. M. Tromp and J. B. Hannon, *Surf. Rev. lett.* 9, 1565 (2002).
78. Y. Ebiko, S. Muto, D. Duzuki, S. Itoh, H. Yamakoshi, K. Shiramine, T. Haga, K. Unno, and M. Ikeda, *Phys. Rev. B* 60, 8234 (1999).
79. J. A. Venables, G. D. T. Spiller, and M. Hanbücken, *Rep. Prog. Phys.* 47, 399 (1984).
80. V. Bressler-Hill, S. Varma, A. Lorke, B. Z. Nosho, P. M. Petroff, and W. H. Weinberg, *Phys. Rev. Lett.* 74, 3209 (1995).
81. M. Schroeder and D. E. Wolf, *Phys. Rev. Lett.* 74, 2026 (1995).
82. M. Schroeder and D. E. Wolf, *Phys. Rev. Lett.* 74, 2026 (1995).
83. A. Madhukar, Q. Xie, P. Chen, and A. Konkar, *Appl. Phys. Lett.* 64, 2727 (1994).
84. Ken-ichi Shiramine, T. Itoch, S. Muto, T. Kozaki, and S. Sato, *J. Cryst. Growth* 242, 332 (2002).
85. K. R. Evans, C. E. Stutz, D. K. Lorance, and R. L. Jones, *J. Vac. Sci. Tech. B* 7(2), 259 (1989).
86. P. B. Joyce, T. J. Krzyzewski, G. R. Bell, T. S. Jones, S. Malik, D. Childs, and R. Murray, *Phys. Rev. B* 62, 10891 (2000).
87. Y. Nakata, K. Mukai, M. Sugawara, K. Ohtsubo, H. Ishikawa, and N. Yokoyama, *J. Cryst. Growth* 208, 93 (2000).
88. S. Kiravittaya, Y. Nakamura, and O. G. Schmidt, *Physica E* 13, 224 (2002).
89. A. Madhukar, Q. Xie, P. Chen, and A. Konkar, *Appl. Phys. Lett.* 64, 2727 (1994).
90. A. Madhukar, Q. Xie, P. Chen, and A. Konkar, *Appl. Phys. Lett.* 64, 2727 (1994).
91. K. Yamaguchi, K. Yujobo, and T. Kaizu, *Jpn. J. Appl. Phys.* 39, L1245 (2000).
92. A. Madhukar, Q. Xie, P. Chen, and A. Konkar, *Appl. Phys. Lett.* 64, 2727 (1994).
93. A. Madhukar, Q. Xie, P. Chen, and A. Konkar, *Appl. Phys. Lett.* 64, 2727 (1994).
94. K. Yamaguchi, K. Yujobo, and T. Kaizu, *Jpn. J. Appl. Phys.* 39, L1245 (2000).
95. G. S. Solomon, J. A. Trezza, and J. S. Harris Jr., *Appl. Phys. Lett.* 66, 3161 (1995).
96. T. Hanada, B.-H. Koo, H. Totsuka, and T. Yao, *Phys. Rev. B* 64, 165307 (2001).
97. K. Jacobi, *Prog. Surf. Sci.* 71, 185 (2003).
98. Y. Nabetani, T. Ishikawa, S. Noda, and A. Sasaki, *J. Appl. Phys.* 76, 347 (1994).
99. Y. Hasegawa, H. Kiyama, Q. K. Xue, and T. Sakurai, *Appl. Phys. Lett.* 72, 2256 (1998).
100. G. Costantini, C. Manznao, R. Sonmuang, O. G. Schmidt and K. Kern, *Appl. Phys. Lett.* 82, 3194 (2003).
101. E. Pehlke, N. Moll, A. Kley, and M. Scheffler, *Appl. Phys. A* 65, 525 (1997).
102. R. Heitz, A. Kalburge, Q. Xie, M. Grundmann, P. Chen, A. Hoffmann, A. Madhukar, and D. Bimberg, *Phys. Rev. B* 57, 9050 (1998).

103. I. Mukhametzhanov, Z. Wei, R. Heitz, and A. Madhukar, *Appl. Phys. Lett.* 75, 85 (1998).
104. M. Grundmann, J. Christen, N. N. Ledentsov, J. Böhrer, D. Bimberg, S. S.Ruvimov, P. Werner, U. Richter, U.Gösele, J. Heydenreich, V. M. Ustinov, A. Yu. Egorov, A. E. Zhukov, P. S. Kop'ev, and Zh. I. Alferov, *Phys. Rev. Lett.* 74(20), 4043 (1995).
105. S. Ruvimov, Z. Liliental-Weber, J. Washburn, N. N. Ledentsov, V. M. Ustinov, V. A. Shchukin, P. S. Kop'ev, Zh. I. Alferov, and D. Bimberg, *Physics of the Solid State* 40, 781 (1998).
106. T. Hanada, B.-H. Koo, H. Totsuka, and T. Yao, *Phys. Rev. B* 64, 165307 (2001).
107. K. Jacobi, *Prog. Surf. Sci.* 71, 185 (2003).
108. Y. Nabetani, T. Ishikawa, S. Noda, and A. Sasaki, *J. Appl. Phys.* 76, 347 (1994).
109. Y. Hasegawa, H. Kiyama, Q. K. Xue, and T. Sakurai, *Appl. Phys. Lett.* 72, 2256 (1998).
110. G. Costantini, C. Manznao, R. Sonmuang, O. G. Schmidt and K. Kern, *Appl. Phys. Lett.* 82, 3194 (2003).
111. E. Pehlke, N. Moll, A. Kley, and M. Scheffler, *Appl. Phys. A* 65, 525 (1997).
112. R. Heitz, A. Kalburge, Q. Xie, M. Grundmann, P. Chen, A. Hoffmann, A. Madhukar, and D. Bimberg, *Phys. Rev. B* 57, 9050 (1998).
113. I. Mukhametzhanov, Z. Wei, R. Heitz, and A. Madhukar, *Appl. Phys. Lett.* 75, 85 (1998).
114. M. Grundmann, J. Christen, N. N. Ledentsov, J. Böhrer, D. Bimberg, S. S. Ruvimov, P. Werner, U. Richter, U.Gösele, J. Heydenreich, V. M. Ustinov, A. Yu. Egorov, A. E. Zhukov, P. S. Kop'ev, and Zh. I. Alferov, *Phys. Rev. Lett.* 74(20), 4043 (1995).
115. S. Ruvimov, Z. Liliental-Weber, and J. Washburn, N. N. Ledentsov, V. M. Ustinov, V. A. Shchukin, P. S. Kop'ev, Zh. I. Alferov, and D. Bimberg, *Physics of the Solid State* 40, 781 (1998).
116. S. P. Kowalczyk, W. J. Schaffer, E. A. Kraut, and R. W. Grant *J. Vac. Sci. Tech. B* 20, 705 (1982).
117. M. Grundmann, J. Christen, N. N. Ledentsov, J. Böhrer, D. Bimberg, S. S. Ruvimov, P. Werner, U. Richter, U.Gösele, J. Heydenreich, V. M. Ustinov, A. Yu. Egorov, A. E. Zhukov, P. S. Kop'ev, and Zh. I. Alferov, *Phys. Rev. Lett.* 74(20), 4043 (1995).
118. S. K. Eah, W. Jhe, and Y. Arakawa, *Appl. Phys. Lett.* 80, 2779 (2002).
119. S. P. Kowalczyk, W. J. Schaffer, E. A. Kraut, and R. W. Grant *J. Vac. Sci. Tech. B* 20, 705 (1982).
120. M. Grundmann, J. Christen, N. N. Ledentsov, J. Böhrer, D. Bimberg, S. S.Ruvimov, P. Werner, U. Richter, U.Gösele, J. Heydenreich, V. M. Ustinov, A. Yu.Egorov, A. E. Zhukov, P. S. Kop'ev, and Zh. I. Alferov, *Phys. Rev. Lett.* 74(20), 4043 (1995).
121. S. K. Eah, W. Jhe, and Y. Arakawa, *Appl. Phys. Lett.* 80, 2779 (2002).
122. M. Grundmann, J. Christen, N. N. Ledentsov, J. Böhrer, D. Bimberg, S. S. Ruvimov, P. Werner, U. Richter, U.Gösele, J. Heydenreich, V. M. Ustinov, A. Yu. Egorov, A. E. Zhukov, P. S. Kop'ev, and Zh. I. Alferov, *Phys. Rev. Lett.* 74(20), 4043 (1995).
123. A. D. Yoffe, *Advances in Physics* 42, 172 (1993).
124. G. Pryor, *Phys. Rev. B* 60, 2869 (1999).
125. L. A. Wang, J. Kim, and A. Zunger, *Phys. Rev. B* 59, 5687 (1999).
126. J. M. García, G. MedeirosRibeiro, K. Schmidt, T. Ngo, J. L. Feng, A. Lorke, J. Kotthaus, and P. M. Petroff, *Appl. Phys. Lett.* 71, 2014 (1997).
127. L. Chu, M. Arzberger, G. Böhm, and G. Abstreiter, *J. Appl. Phys.* 85, 2355 (1999).
128. M. G. Alessi, M. Capizzi, A. S. Bhatti, A. Frova, F. Martelli, P. Frigeri, A. Bosacchi, and S. Franchi, *Phys. Rev. B* 59, 7620 (1999).
129. L. Chu, M. Arzberger, G. Böhm, and G. Abstreiter, *J. Appl. Phys.* 85, 2355 (1999).
130. T. Kaizu and K. Yamaguchi, *Jpn. J. Appl. Phys.* 40, 1885 (2001).
131. M. Grundmann, J. Christen, N. N. Ledentsov, J. Böhrer, D. Bimberg, S. S. Ruvimov, P. Werner, U. Richter, U.Gösele, J. Heydenreich, V. M. Ustinov, A. Yu. Egorov, A. E. Zhukov, P. S. Kop'ev, and Zh. I. Alferov, *Phys. Rev. Lett.* 74(20), 4043 (1995).
132. L. Chu, M. Arzberger, G. Böhm, and G. Abstreiter, *J. Appl. Phys.* 85, 2355 (1999).
133. L. Chu, M. Arzberger, G. Böhm, and G. Abstreiter, *J. Appl. Phys.* 85, 2355 (1999).
134. K. Yamaguchi, K. Yujobo, and T. Kaizu, *Jpn. J. Appl. Phys.* 39, L1245 (2000).
135. U. Bockelmann and G. Bastard, *Phys. Rev. B* 42, 8947 (1990).
136. F. Adler, M. Geiger, A. Bauknecht, F. Scholz, H. Schweizer, M. H. Pilkuhn, B. Ohnesorge, and A. Forchel, *J. Appl. Phys.* 80, 4019 (1996).
137. E. C. Le Ru, J. Fack, and R. Murray, *Phys. Rev. B* 67, 245318 (2003).
138. F. Adler, M. Geiger, A. Bauknecht, F. Scholz, H. Schweizer, M. H. Pilkuhn, B. Ohnesorge, and A. Forchel, *J. Appl. Phys.* 80, 4019 (1996).
139. E. C. Le Ru, J. Fack, and R. Murray, *Phys. Rev. B* 67, 245318 (2003).
140. F. Adler, M. Geiger, A. Bauknecht, F. Scholz, H. Schweizer, M. H. Pilkuhn, B. Ohnesorge, and A. Forchel, *J. Appl. Phys.* 80, 4019 (1996).
141. R. Heitz, M. Veit, N. N. Ledentsov, A. Hoffmann, D. Bimberg, V. M. Ustinov, P. S. Kop'ev, and Zh. I. Alferov, *Phys. Rev. B* 56, 10435 (1997).
142. B. Ohnesorge, M. Albrecht, J. Oshinowo, A. Forchel, and Y. Arakawa, *Phys. Rev. B* 54, 11532 (1996).
143. R. Heitz, M. Veit, N. N. Ledentsov, A. Hoffmann, D. Bimberg, V. M. Ustinov, P. S. Kop'ev, and Zh. I. Alferov, *Phys. Rev. B* 56, 10435 (1997).
144. J. Feldmann, S. T. Cundiff, M. Arzberger, G. Böhm, and G. Abstreiter, *J. Appl. Phys.* 89, 1180 (2001).
145. Tae-Won Kang and Jae-Eung Oh, *J. Cryst. Growth* 227–228, 1039 (2001).
146. W. H. Jiang, X. L. Ye, B. Xu, H. Z. Xu, D. Ding, J. B. Liang, and Z. G. Wang, *J. Appl. Phys.* 88, 2529 (2001).
147. E. C. Le Ru, J. Fack, and R. Murray, *Phys. Rev. B* 67, 245318 (2003).

148. U. Bockelmann, G. Bastard, *Phys. Rev. B* 42, 8947 (1990).
149. F. Adler, M. Geiger, A. Bauknecht, F. Scholz, H. Schweizer, M. H. Pilkuhn, B. Ohnesorge and A. Forchel, *J. Appl. Phys.* 80, 1996 (4019).
150. R. Heitz, A. Kalburge, Q. Xie, M. Grundmann, P. Chen, A. Hoffmann, A. Madhukar, D. Bimberg, *Phys. Rev. B*, 57, 1998 (9050).
151. G. G. Tarasov, Yu. I. Mazur, Z. Ya. Zhuchenko, A. Maaßdorf, D. Nickel, J. W. Tomm, H. Kissel, C. Walther, and W. T. Masselink, *J. Appl. Phys.* 88, 7162 (2000).
152. M. Grundmann, J. Christen, N. N. Ledentsov, J. Böhrer, D. Bimberg, S. S. Ruvimov, P. Werner, U. Richter, U.Gösele, J. Heydenreich, V. M. Ustinov, A. Yu. Egorov, A. E. Zhukov, P. S. Kop'ev, and Zh. I. Alferov, *Phys. Rev. Lett.*, 74(20), 4043 (1995).
153. A. D. Yoffe, *Advances in Physics* 42, 172 (1993).
154. G. Pryor, *Phys. Rev. B* 60, 2869 (1999).
155. L. A. Wang, J. Kim, and A. Zunger, *Phys. Rev. B* 59, 5687 (1999).
156. J. M. García, G. MedeirosRibeiro, K. Schmidt, T. Ngo, J. L. Feng, A. Lorke, J. Kotthaus, and P. M. Petroff, *Appl. Phys. Lett.* 71, 2014 (1997).
157. L. Chu, M. Arzberger, G. Böhm, and G. Abstreiter, *J. Appl. Phys.* 85, 2355 (1999).
158. M. G. Alessi, M. Capizzi, A. S. Bhatti, A. Frova, F. Martelli, P. Frigeri, A. Bosacchi, and S. Franchi, *Phys. Rev. B* 59, 7620 (1999).
159. L. Chu, M. Arzberger, G. Böhm, and G. Abstreiter, *J. Appl. Phys.* 85, 2355 (1999).
160. T. Kaizu and K. Yamaguchi, *Jpn. J. Appl. Phys.* 40, 1885 (2001).
161. M. Grundmann, J. Christen, N. N. Ledentsov, J. Böhrer, D. Bimberg, S. S. Ruvimov, P. Werner, U. Richter, U.Gösele, J. Heydenreich, V. M. Ustinov, A. Yu. Egorov, A. E. Zhukov, P. S. Kop'ev, and Zh. I. Alferov, *Phys. Rev. Lett.* 74(20), 4043 (1995).
162. L. Chu, M. Arzberger, G. Böhm, and G. Abstreiter, *J. Appl. Phys.* 85, 2355 (1999).
163. L. Chu, M. Arzberger, G. Böhm, and G. Abstreiter, *J. Appl. Phys.* 85, 2355 (1999).
164. K. Yamaguchi, K. Yujobo, and T. Kaizu, *Jpn. J. Appl. Phys.* 39, L1245 (2000).
165. U. Bockelmann and G. Bastard, *Phys. Rev. B* 42, 8947 (1990).
166. F. Adler, M. Geiger, A. Bauknecht, F. Scholz, H. Schweizer, M. H. Pilkuhn, B. Ohnesorge, and A. Forchel, *J. Appl. Phys.* 80, 4019 (1996).
167. E. C. Le Ru, J. Fack, and R. Murray, *Phys. Rev. B* 67, 245318 (2003).
168. F. Adler, M. Geiger, A. Bauknecht, F. Scholz, H. Schweizer, M. H. Pilkuhn, B. Ohnesorge, and A. Forchel, *J. Appl. Phys.* 80, 4019 (1996).
169. E. C. Le Ru, J. Fack, and R. Murray, *Phys. Rev. B* 67, 245318 (2003).
170. F. Adler, M. Geiger, A. Bauknecht, F. Scholz, H. Schweizer, M. H. Pilkuhn, B. Ohnesorge, and A. Forchel, *J. Appl. Phys.* 80, 4019 (1996).
171. R. Heitz, M. Veit, N. N. Ledentsov, A. Hoffmann, D. Bimberg, V. M. Ustinov, P. S. Kop'ev, and Zh. I. Alferov, *Phys. Rev. B* 56, 10435 (1997).
172. B. Ohnesorge, M. Albrecht, J. Oshinowo, A. Forchel, and Y. Arakawa, *Phys. Rev. B* 54, 11532 (1996).
173. R. Heitz, M. Veit, N. N. Ledentsov, A. Hoffmann, D. Bimberg, V. M. Ustinov, P. S. Kop'ev, and Zh. I. Alferov, *Phys. Rev. B* 56, 10435 (1997).
174. J. Feldmann, S. T. Cundiff, M. Arzberger, G. Böhm and G. Abstreiter, *J. Appl. Phys.* 89, 1180 (2001).
175. Tae-Won Kang and Jae-Eung Oh, *J. Cryst. Growth* 227–228, 1039 (2001).
176. W. H. Jiang, X. L. Ye, B. Xu, H. Z. Xu, D. Ding, J. B. Liang, and Z. G. Wang, *J. Appl. Phys.* 88, 2529 (2001).
177. E. C. Le Ru, J. Fack, and R. Murray, *Phys. Rev. B* 67, 245318 (2003).
178. U. Bockelmann and G. Bastard, *Phys. Rev. B* 42, 8947 (1990).
179. F. Adler, M. Geiger, A. Bauknecht, F. Scholz, H. Schweizer, M. H. Pilkuhn, B. Ohnesorge, and A. Forchel, *J. Appl. Phys.* 80, 4019 (1996).
180. R. Heitz, A. Kalburge, Q. Xie, M. Grundmann, P. Chen, A. Hoffmann, A. Madhukar, and D. Bimberg, *Phys. Rev. B* 57, 9050 (1998).
181. G. G. Tarasov, Yu. I. Mazur, Z. Ya. Zhuchenko, A. Maaßdorf, D. Nickel, J. W. Tomm, H. Kissel, C. Walther, and W. T. Masselink, *J. Appl. Phys.* 88, 7162 (2000).
182. R. Heitz, A. Kalburge, Q. Xie, M. Grundmann, P. Chen, A. Hoffmann, A. Madhukar, and D. Bimberg, *Phys. Rev. B* 57, 9050 (1998).
183. M. Sugawara, *Semiconductors and Semimetals* 60, 132 (1999).
184. H. Shoji, Y. Nakata, K. Mukai, Y. Sugiyama, and M. Sugawara, *Jpn. J. Appl. Phys.* 35, L903 (1996).
185. M. Grundmann and D. Bimberg, *Jpn. J. Appl. Phys.* 36 Part 1, 4181 (1997).
186. B. Shi and Y. H. Xie, *Appl. Phys. Lett.* 82, 4788 (2003).
187. R. Heitz, A. Kalburge, Q. Xie, M. Grundmann, P. Chen, A. Hoffmann, A. Madhukar, and D. Bimberg, *Phys. Rev. B* 57, 9050 (1998).
188. M. Sugawara, *Semiconductors and Semimetals* 60, 132 (1999).
189. H. Shoji, Y. Nakata, K. Mukai, Y. Sugiyama, M. Sugawara, *Jpn. J. Appl. Phys.* 35, L903 (1996).
190. M. Grundmann and D. Bimberg, *Jpn. J. Appl. Phys.* 36 Part 1, 4181 (1997).
191. B. Shi and Y. H. Xie, *Appl. Phys. Lett.* 82, 4788 (2003).
192. R. Murray, D. Childs, S. Malik, P. Siverns, C. Roberts, J. M. Hartmann, and P. Stavrinou, *Jpn. J. Appl. Phys.* 38, 528 (1999).
193. P. B. Joyce, T. J. Krzyzewski, G. R. Bell, T. S. Jones, E. C. Le Ru, and R. Murray, *Phys. Rev. B* 64, 235317 (2001).

194. R. P. Mirin, J. P. Ibbetson, J. E. Bowers, and A. C. Gossard, *J. Cryst. Growth* 175/176, 696 (1997).
195. D. L. Huffaker and D. G. Deppe, *Appl. Phys. Lett.* 73, 520 (1998).
196. K. Mukai, N. Ohtsuka, M. Sugawara, and S. Yamazaki, *Jpn. J. Appl. Phys.* 33 Part 2, L1710 (1994).
197. J. M. Gerard, A. Lemaitre, B. Legrand, A. Ponchet, B. Gayral, and V. Thierry-Mieg, *J. Cryst. Growth* 201/202, 1109 (1999).
198. K. Nishi, H. Saito, S. Sugo, and J. S. Lee, *Appl. Phys. Lett.* 74, 1111 (1999).
199. F. Ferdos, M. Sadeghi, Q. X. Zhao, S. M. Wang, and A. Larsson, *J. Cryst. Growth* 227–228, 1140 (2001).
200. A. F. Tsatsul'nikov, A. R. Kovsh, A. E. Zhukov, Yu. M. Shernyakov, Yu. G. Musikhin, V. M. Ustinov, N. A. Bert, P. S. Kop'ev, and Zh. I. Alferov, A. M. Mintairov, J. L. Merz, N. N. Ledentsov, and D. Bimberg, *Appl. Phys. Lett.* 88, 6272 (2000).
201. Y. Nakata, K. Mukai, M. Sugawara, K. Ohtsubo, H. Ishikawa, and N. Yokoyama, *J. Cryst. Growth* 208, 93 (2000).
202. R. Murray, D. Childs, S. Malik, P. Siverns, C. Roberts,J. M. Hartmann, and P. Stavrinou, *Jpn. J. Appl. Phys.* 38, 528 (1999).
203. P. B. Joyce, T. J. Krzyzewski, G. R. Bell, T. S. Jones, E. C. Le Ru, and R. Murray, *Phys. Rev. B* 64, 235317 (2001).
204. R. P. Mirin, J. P. Ibbetson, J. E. Bowers, and A. C. Gossard, *J. Cryst. Growth* 175/176, 696 (1997).
205. D. L. Huffaker and D. G. Deppe, *Appl. Phys. Lett.* 73, 520 (1998).
206. K. Mukai, N. Ohtsuka, M. Sugawara, and S. Yamazaki, *Jpn. J. Appl. Phys.* 33 Part 2, L1710 (1994).
207. J. M. Gerard, A. Lemaitre, B. Legrand, A. Ponchet, B.Gayral, and V. Thierry-Mieg, *J. Cryst. Growth* 201/202, 1109 (1999).
208. K. Nishi, H. Saito, S. Sugo, and J. S. Lee, *Appl. Phys. Lett.* 74, 1111 (1999).
209. F. Ferdos, M. Sadeghi, Q. X. Zhao, S. M. Wang, and A. Larsson, *J. Cryst. Growth* 227–228, 1140 (2001).
210. A. F. Tsatsul'nikov, A. R. Kovsh, A. E. Zhukov, Yu. M. Shernyakov, Yu. G. Musikhin, V. M. Ustinov, N. A. Bert, P. S. Kop'ev, and Zh. I. Alferov, A. M. Mintairov, J. L. Merz, N. N. Ledentsov, and D. Bimberg, *Appl. Phys. Lett.* 88, 6272 (2000).
211. Y. Nakata, K. Mukai, M. Sugawara, K. Ohtsubo, H. Ishikawa, and N. Yokoyama, *J. Cryst. Growth* 208, 93 (2000).
212. Chris G. Van de Walle, *Phys. Rev. B* 38, 1871 (1989).
213. C. Pryor, J. Kim, L. W. Wang, A. J. Williamson, and A. Zunger, *J. Appl. Phys.* 83, 2548 (1998).
214. Y. Kikuchi, H. Sugii, and K. Shintani, *J. Appl. Phys.* 89, 1191 (2001).
215. H. T. Johnson and L. B. Freund, *J. Appl. Phys.* 81, 6081 (1997).
216. J. R. Downes, D. A. Faux, and E. P. O'Reilly, *J. Appl. Phys.* 81, 6700 (1997).
217. G. S. Pearson and D. A. Faux, *J. Appl. Phys.* 88, 730 (2000).
218. G. Pryor, *Phys. Rev. B* 60, 2869 (1999).
219. L. A. Wang, J. Kim, and A. Zunger, *Phys. Rev. B* 59, 5687 (1999).
220. H. T. Johnson and L. B. Freund, *J. Appl. Phys.* 81, 6081 (1997).
221. H. T. Johnson and L. B. Freund, *J. Appl. Phys.* 81, 6081 (1997).
222. A. Madhukar , Q. Xie, P. Chen, and A. Konkar, *Appl. Phys. Lett.* 64, 2727 (1994).
223. C. Priester and M. Lannoo, *Phys. Rev. Lett.* 75, 93 (1995).
224. Feng Liu, Adam H. Li, and M. G. Lagally, *Phys. Rev. Lett.* 87, 126103 (2001).
225. B. Daudin, F. Widmann, G. Feuillet, Y. Samson, M. Arlery, and J. L. Rouvière, *Phys. Rev. B* 56, R7069 (1997).
226. F. Widmann, B. Daudin, G. Feuillet, Y. Samson, J. L. Rouvière, and N. Pelekanos, *J. Appl. Phys.* 83, 7618 (1998).
227. I. Kegal, T. H. Metzger, J. Peisl, J. Stangl, G. Bauer, and D. Smilgies, *Phys. Rev. B* 60, 2516 (1999).
228. P. Schittenhelm, C. Engel, F. Findeis, G. Abstreiter, A. A. Darhuber, G. Bauer, A. O. Kosogov, and P. Werner, *J. Vac. Sci. Technol. B* 16, 1575 (1998).
229. E. Martinez-Guerrero, C. Adelmann, F. Chabuel, J. Simon, N. T. Pelekanos, Guido Mula, B. Daudin, G. Feuillet, and H. Mariette, *Appl. Phys. Lett.* 77, 809 (2000).
230. F. Widmann, B. Daudin, G. Feuillet, Y. Samson, J. L. Rouvière, and N. Pelekanos, *J. Appl. Phys.* 83, 7618 (1998).
231. M. Pinczolits, G. Springholz, and G. Bauer, *Appl. Phys. Lett.* 73, 250 (1998).
232. K. Alchalabi, D. Zimin, G. Kostorz, and H. Zogg, *Phys. Rev. Lett.* 90, 026104-1 (2003).
233. H. Kroemer, *Mat. Res. Soc. Symp. Proc.* 67, 3 (1986).
234. G. E. Cirlin, N. K. Polyakov, V. N. Petrov, V. A. Egorov, B. V. Denisov, B. V. Volovik, V. M. Ustinov, Zh.I. Alferov, N. N. Ledentsov, R. Heitz, D. Bimberg, N. D. Zakharov, P. Werner, and U. Gösele, *Mater. Phys. Mech.* 1, 15 (2000).
235. L. Hansen, F. Bensing, and A. Waag, *Thin Solid Films* 367, 85 (2000).
236. T. Mano, H. Fujioka, K. Ono, Y. Watanabe, and M. Oshima, *Appl. Sur. Sci.* 130–132, 760 (1998).
237. W. A. Harrison, E. A. Kraut, J. R. Waldrop, and R. W. Grant, *Phys. Rev. B* 18(8), 4402 (1978).
238. A. Zdyb, J. M. Olchowik, D. Szymczuk, J. Mucha, K. Zabielski, M. Mucha, and W. Sadowski, *Cryst. Res. Technol.* 37, 875 (2002).
239. R. D. Bringans, *Crit. Rev. in Sol. State Mat. Sci.* 17, 353 (1992).
240. J. E. Northrup, *Phys. Rev. Lett.* 62, 2487 (1989).
241. D. K. Biegelsen, F. A. Ponce, A. J. Smith, and J. C. Tramontana, *J. Appl. Phys.* 61(5), 1856 (1987).
242. Doeke J. Oostra, Russell V. Smilgys, and Stephen R. Leone, *Appl. Phys. Lett.* 55, 1333 (1989).
243. J. E. Northrup, *Phys. Rev. Lett.* 62, 2487 (1989).

244. G. E. Cyrlin, V. N. Petrov, V. G. Dubrovskii, Yu. B. Samsonenko, N. K. Polyakov, A. O. Golubok, S. A. Masalov, and N. I. Komyak, V. M. Ustinov, A. Yu. Egorov, A. R. Kovsh, M. V. Maximov, A. F. Tsatsul'nikov, B. V. Volovik, A. E. Zhukov, P. S. Kop'ev, N. N. Ledentsov, and Zh. I. Alferov, and D. Bimberg, *Semiconductors* 33, 972 (1999).
245. M. Jo, K. Ishida1, K. Kawamoto, and S. Fukatsu, *Phys. Stat. Sol. (c)* 1117 (2003).
246. N. D. Zakharov, P. Werner, and U. Go¨sele, R. Heitz and D. Bimberg, N. N. Ledentsov, V. M. Ustinov, B. V. Volovik, Zh. I. Alferov, N. K. Polyakov, V. N. Petrov, V. A. Egorov, and G. E. Cirlin, *Appl. Phys. Lett.* 76, 2677 (2000).
247. R. Heitz, N. N. Ledentsov, D. Bimberg, A.Yu. Egorov, M. V. Maximov, V. M. Ustinov, A. E. Zhukov, Zh.I. Alferov, G. E. Cirlin, I. P. Soshnikov, N. D. Zakharov, P. Wernerd, and U. G osele. *Appl. Phys. Lett.* 74, 1701 (1999).
248. S. Fukatsu, M. Jo, K. Ishida, N. Yasuhara, and K. Kawamoto, *Materials Science and Engineering C* 23, 683 (2003).